To the Graduate Council:

I am submitting herewith a thesis written by Farhad Nazeradl entitled "The Influence of Shielding Gas Type and Mass Flow on the Melt Zone in the Surface Treatment of 1010 Steel Using Continuous-Wave High-Power CO_2 and Nd:YAG Lasers." I have examined the final copy of this thesis for form and content and recommend that it be accepted in partial fulfillment of the requirements for the degree of Master of Science, with a major in Metallurgical Engineering.

Dr. Mary Helen McCay, Major Professor

We have read this thesis
and recommend its acceptance:

Accepted for the Council:

Associate Vice Chancellor and
Dean of The Graduate School

THE INFLUENCE OF SHIELDING GAS TYPE AND MASS FLOW ON THE MELT ZONE IN THE SURFACE TREATMENT OF 1010 STEEL USING CONTINUOUS-WAVE HIGH-POWER CO_2 AND Nd:YAG LASERS

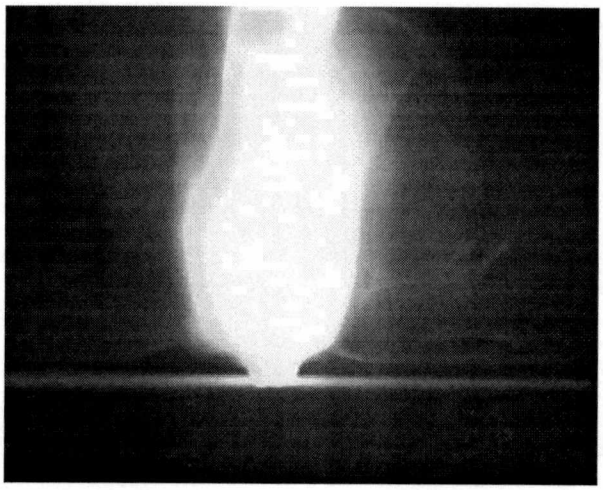

A Thesis

Presented for the

Master of Science

Degree

The University of Tennessee, Knoxville

Farhad Nazeradl

May 1998

This thesis is dedicated to my parents.

ACKNOWLEDGMENTS

I would like to thank my thesis advisor, Dr. Mary Helen McCay, for her guidance through the development of this research and careful revision of my thesis. I would also like to thank Dr. Narendra Dahotre for his great support and participation in my thesis committee. Special thanks goes for my other thesis committee member, Dr. Anthony Pedreaza, for his cooperation and advice on my thesis.

I am also grateful to Dr. Dwayne McCay and Dr. John Hopkins for participating in my defense and giving useful directions.

There are a number of people whose assistance should be recognized including Mike Sharp and Fred Schwartz and other members and staff of Center for Laser Application in the University of Tennessee Space Institute. I am very much thankful to Mary Lo for her around-the-clock assistance in searching references related to my study.

ABSTRACT

In studying the surface laser processing techniques several important factors have been the focus of this investigation. The effects of laser scanning speed, mass flow and type of shielding gas on the melt depth of ¼" thick 1010 steel have been studied in this project. In agreement with previous works, increasing scanning speed showed a decrease in the depth of the melt zone in the process. The next factor, the shielding gas mass flow effect, is the least investigated factor in the recent literature. Using a depth prediction method employed by Steen-Eherhad, we have established a corresponding mathematical formula for a 2000W laser power at a constant 1500mm/min scanning speed. Speed effect has a very good agreement with theoretical result derived by Steen-Ehrhard. In analyzing the melt depth data a first order linear regression was applied and in most cases this regression shows a good correlation between melt depth and mass flow of shielding gases. Our data acquired by measuring plasma size also indicates that the plasma size does not have a correlation with the melt zone depth.

PREFACE

Surface treatment of materials has become an increasingly important technique in modern manufacturing. Corrosion, friction and wear of material sometimes could easily be prevented by applying layer of more resistive materials (thermal, mechanical or chemical resistance) on the bulk substrate. Reinforcing the construction material locally at the surface region helps to save the use of more expensive material as bulk.

The high costs of laser machinery and the demand for more proficient crew to operate and maintain such equipment may have hindered wide spread use of laser surface processing (LSP) in every day industrial applications. Today, with advances in design of user friendly and cost effective laser sources, LSP technology promises extensive applications by the industry in the near future.

The LSP at UTSI (University of Tennessee Space Institute) started as a need at AEDC (Arnold Engineering and Development Center) for replacement of existing large scale structures, such as the AEDC wind tunnel, with non-corrosive material. For the existing wind tunnel facilities at AEDC, replacement of structure with that of a non-corrosive substitute is extremely costly.

Using 1010 steel as substrate (same material as some part of the AEDC wind tunnel structure) it was demonstrated that by laser melting a chromium powder mix, a thin layer (~1mm) of stainless-steel equivalent (more than 12% chromium) could be

created on the surface. A mixture of chromium powder and binder was applied on the surface of a flat 1010 steel plate. Later, a high power CO_2 laser[1] beam on the surface was applied to create a thick enough layer of Fe-Cr-C alloy on the surface to stand the requirement of AEDC for corrosion resistance.

Although initial lab processes on the surface of 1010 steel plate seemed satisfactory, from practical point of view it was not possible to move the CO_2 laser to the site to apply the surface alloying methods. To overcome the inflexibility of the traditional high-power CO_2 laser a Nd:YAG laser with flexible fiberoptic replaced the laser source for this process. One of the major differences between the CO_2 and the Nd:YAG laser is the shorter wavelength[2] of the laser light emitted by Nd:YAG. Not only this gives a better coupling efficiency into the material, it also enables the Nd:YAG laser light to be transmitted through fiber optics. When the fiber optical systems are used for beam transportation instead of the traditional reflective optical system, the beam can be transmitted over several hundred meters, and the laser beam maybe manipulated in a very flexible manner, even by robotic systems. The operational versatility is one of the most important aims of the LSP program at UTSI, which means LSP techniques could eventually be applied on complex and/or hard to reach structures.

---

[1]- Although maximum power of this CO_2 laser is around 3000 watts, it is never necessary to apply full power of the beam for this application.

[2]- Nd:YAG wavelength is ~1.06μm compare to ~10.6 μm of CO_2 laser.

TABLE OF CONTENT

PAGE

LIST OF TABLES

TABLE PAGE

LIST OF FIGURES

FIGURE PAGE

NOMENCLATURE

A	absorption
A_{CO2}	absorptivity of metals for CO_2 laser [%]
A_{YAG}	absorptivity of metals for Nd:YAG laser [%]
α	emissivity
a	d.c resistivity component
b	d.c resistivity component
C	specific heat [J/ kg-K]
d_0	diameter of beam at the waist [m]
D_f	defocus distance [m]
d_{MZ}	depth of melt zone [m]
d_{HAZ}	depth of heat affected zone [m]
E	radiative energy [W]
E_{rcl}	energy release at the surface for each electron-ion pair being absorbed [J]
E_{ion}	ionization energy of single atom [J]
σ	Stefan-Boltzmann constant [5.67051×10^{-8} W/m^2-K^4]
σ_t	total cross section of for ion neutral collision [m^2]
I	incident laser power density [W/m^2]
I_0	incident laser power density at the center of the beam [W/m^2]
K	thermal conductivity [W/m-C]

k	thermal diffusivity [m^2/s]
k	refraction index (constant in imaginary part)
k_B	Boltzmann's constant [1.380658×10^{-23} J/K]
L	thickness of the sheet [m]
m	refraction index
n	refraction index (constant in real part)
n_i	ion density [m^{-3}]
P	total laser beam power [W]
P_{HC}	heat conduction power [W]
R_0	reflectivity at normal incidence [%]
r_0	beam radius at focus [m]
r	radial distance [m]
r_*	regression coefficient
T	temperature [K]
T_α	phase transformation temperature [K]
T_b	boiling temperature [K]
T_m	melting temperature [K]
T_v	vaporizing temperature [K]
T_h	heat affected temperature [K]
T_s	surface temperature [K]

T_n	plasma temperature [K]
T_n	temperature of neutrals[K]
T_e	temperature of electrons[K]
T_i	temperature of ions [K]
t	time [s]
γ	coefficient of resistivity change with temperature
λ	wavelength [m or μm]
ρ_0	resistively at 20^0 C
ρ_m	d.c. resistivity [Ω/m]
ω	angular frequency [rad/s]
v	scan velocity [m/s]
Z	depth of melt pool [m]

Abbreviations:

Ar	Argon
CCD	couple charged device
CO_2	carbon dioxide
CW	continuos wave
d.c.	direct current
HAZ	heat affected zone
He	helium

LSP	laser surface processing
MZ	melt zone
ND	neutral density
Nd:YAG	yttrium aluminum garnet doped with active neodymium
N_2	nitrogen
O_2	oxygen
ppm	part per million
RD-	*rust and dust* project sample for CO_2 laser
RF	radio frequency
SGI	silicon graphics indigo
TEM	transverse electromagnetic wave
YRD-	*rust and dust* project sample for Nd:YAG laser

Units:

C	degree centigrade
eV	electron volt
K	degree Kelvin
kHz	kilo-Hertz
m	meter
mrad	milli-radian
MHz	mega-Hertz
mm	millimeter

μm	micrometer
μs	micro second
SU	scale unit of mass flow from instrument column
W	watts
Ω	ohm

CHAPTER 1

BASIC ELEMENTS

1.1 Laser Surface Processing Parameters

When processing with a laser, the alloy has to be shielded against oxidation as in the traditional welding and melting. This is usually accomplished with an inert shielding gas such as argon or helium. In addition to melting, the high-power laser beam vaporizes a small amount of material and also ionizes the shielding gas on top of the beam's foot print, which creates a plasma cloud over the molten surface (Figure 1.1). This hot vapor could play an important role in beam-solid coupling, particularly for CO_2 and Nd:YAG infrared wavelengths.

The range of the beam power density where evaporation is achieved extends from 10^3 W/cm^2 to 10^{15} W/cm^2. Assuming 300μm for the diameter of the laser beam and an applied power of 2000W it can be seen that the intensity of the laser beam on the surface lies well inside this range (around 3×10^{10} W/cm^2). In addition, around 10^7 to 10^{10} W/cm^2 beam intensities the vapor becomes partially ionized and absorbs an important portion of the laser energy[5]. Base on these criteria, in our discussion the hot vapor on top of the sample will be called "*plasma*".

When shielding gas is blown toward the melt surface, it will probably influence the shape and stability of the melt zone by physical contact and in some cases by

changing the surface tension of molten pool. The experimental procedure is aimed at studying the size and shape of the melt zone (MZ) related to the shielding gas mass transfer within the interaction zone, the type of shielding gas, the advance speed of the laser beam on the surface and the size of the plasma (Figure 1.2).

In order to ascertain only the effect of shielding gas and plasma on the MZ we eliminated the application of chromium power mix on the surface, and studied only the beam interaction on plain 1010 steel surface. In the future, data acquired from different shielding gas effects is expected to improve penetration and mechanical characteristic of alloying process.

1.2 Shielding Gas[11]

Seven widely used shielding gases are employed for this project: argon, argon + SO_2 (701ppm SO_2), helium, CO_2, nitrogen, oxygen, and air. The most widely used shielding gases for laser processing of steels are helium and argon, with helium being said to produce significantly more penetration than argon. Additions of small amounts of sulfur dioxide to argon gas also enhances the melt depth. Carbon dioxide is a very good alternative to both helium and argon. According to some reports[10], and it provides nearly the same penetration as helium but it costs less than helium and argon. The major drawback of using CO_2 as the shielding gas for steels is that it can cause porosity in the MZ[10,11].

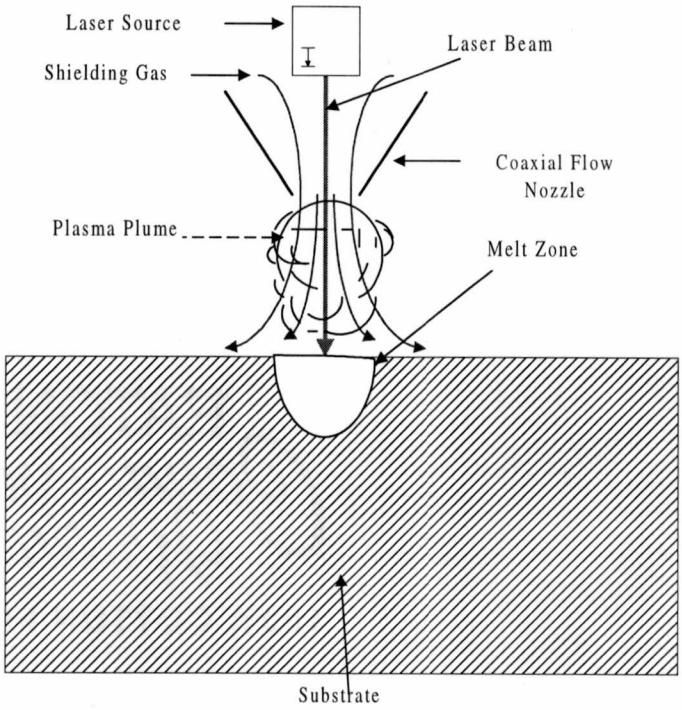

Figure 1.1 Laser induced plasma cloud in a typical LSP using coaxial shielding gas flow

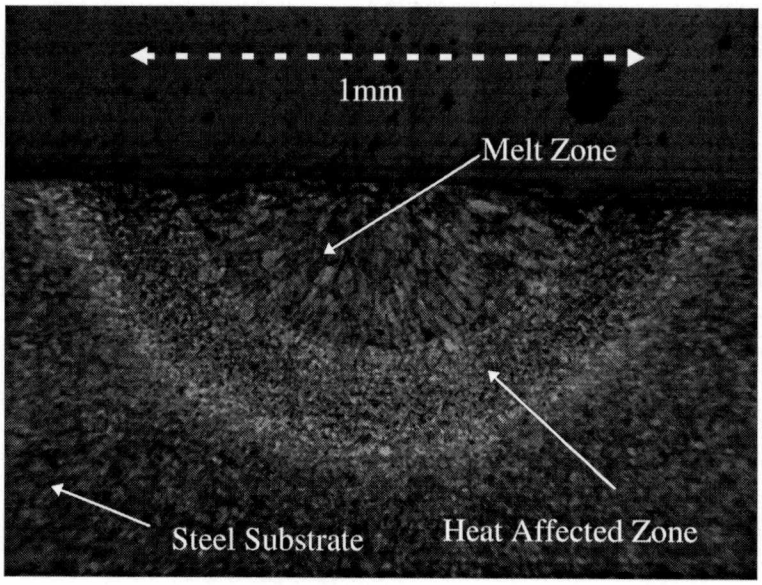

Figure 1.2 Cross section of steel slab after surface melting by high-power laser

At the same time, nitrogen offers better MZ performance than argon while being less expensive. Oxygen and air both offer some degree of enhanced penetrations but the amount of oxidation when using these gases is probably too high for industrial use.

The emphasis of the initial step in this study is to determine the effect of increasing the mass flow of the shielding gas on the size of the MZ. The shielding gas is controlled through an indicator/control valve, with the mass flow unit presented as *scale unit* (Figure 1.3a). Therefore, readings on the mass flow would actually be based on liter per minute (L/min) of each gas on the melt track. Using data in Appendix A, and assuming an ideal gas, the mass flow based on L/min can be converted to gram per second mass flow. The latter is closer to the mass flow concept and later can be used to determine the thermophysical characteristics of gases on the melt zone and plasma plume (Figure 1.3b).

1.3 Laser Induced Plasma [23]

In many laser processes an intense luminous plume which often contains a plasma is formed above the hot surface of the irradiated metal (Figure1.4). The incident power is absorbed partly in the plasma and partly by the surface of the workpiece, depending on the wavelength of the lasers. Since plasma are capable of absorbing a significant part of the incident laser energy, they strongly influence the transfer of laser energy into the workpiece.

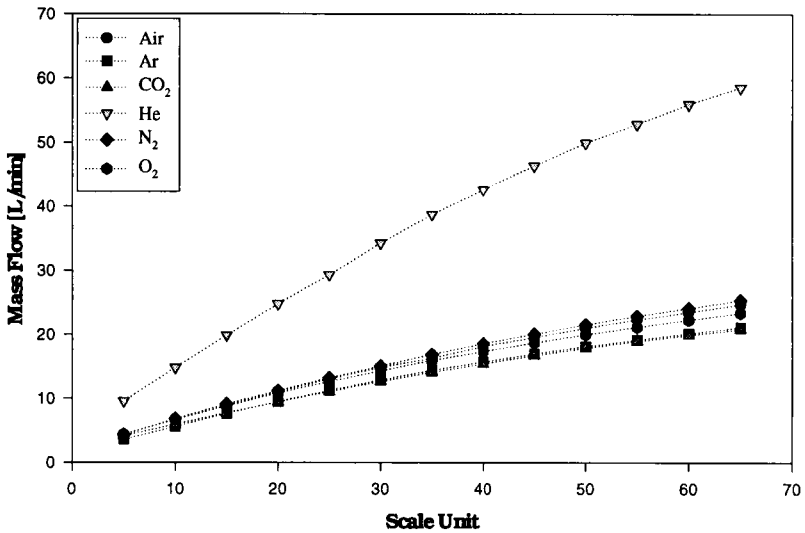

(a)

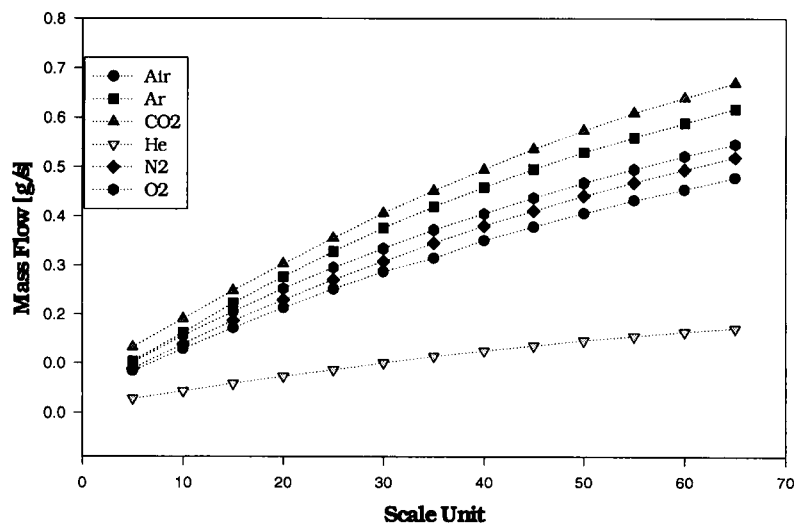

(b)

Figure 1.3 Mass Calibration, (a) scale unit conversion to Liter/min, (b) scale unit conversion to gram/s

The plasma may contain ionized cover gases or vaporized substrate material from the workpiece. The plasma has different physical and optical characteristics depending on the type of material, ionization level of the material, temperature of formation and density of the hot vapor formed in the plasma. See Appendix A (Table A.1) for the ionization potentials of the shielding gases and Appendix B (Table B.1) for the ionization potential of vapor phase iron. These characteristics may cause different absorption levels for different laser wavelengths such as CO2 and Nd:YAG lasers.

In addition to the temperature and density of the plasma, the energy transfer also depends on the physical properties of the material and the processing parameters. Some of these processing parameters are mass flow of the shielding gas, laser power, and the laser beam diameter. Some of the physical properties of iron are listed in Appendix B (Table B.1).

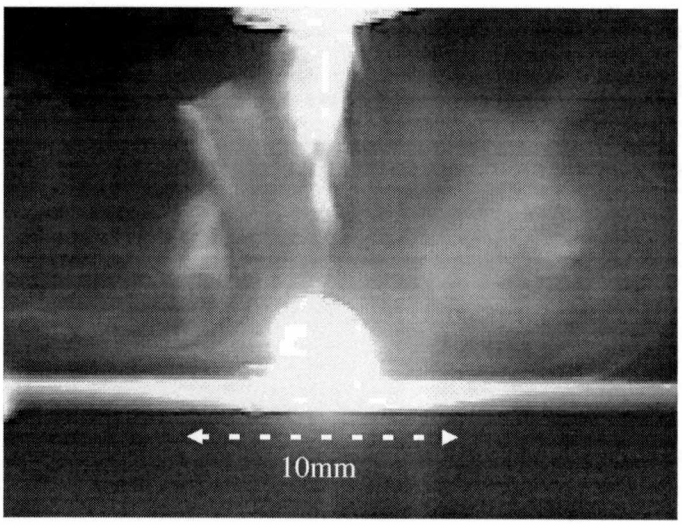

Figure 1.4 Plasma formation above melt surface during LSP of 1010 steel using 2000W CO_2 laser with argon shielding gas.

CHAPTER 2

EXPERIMENTAL SET-UP

Two sets of different laser sources will be used in this experiment and results from the two lasers will be compared.

2.1 CO_2 Laser

The ROFIN-SINAR RS-3000 (Figure 2.1) is a carbon dioxide industrial laser mainly used for deep welding and cutting of material, but in surface treatment could also be as versatile. The active medium in CO_2 laser is a mixture of high grade CO_2, N_2 and He gases, where CO_2 are active molecules that emit the part of the energy absorbed in the form of infrared 10.6μm radiation from a transition between two rotational lines in the 9.4μm and 10.4μm bands. Excitation of the active medium is accomplished by direct electrical discharges in the gases[1,4].

These characteristics (Table 2.1) are achieved by using high-speed axial flow and RF excitation of laser gases. The gas in the high-speed axial gas circulation of RS-3000 laser moves in the resonator parallel to the direction of propagation of the laser light at a speed close to the speed of sound. This means that a high power density is achieved in the excitation volume[6].

Table 2.1 Some characteristics of RS-3000 laser.

Wavelength:	10.6μm		Beam diameter:	30 mm
Excitation:	RF 27.12 MHz		Beam divergence:	1.5 mrad
Output range:	300-3000 W		Pulse width:	20 μs-CW

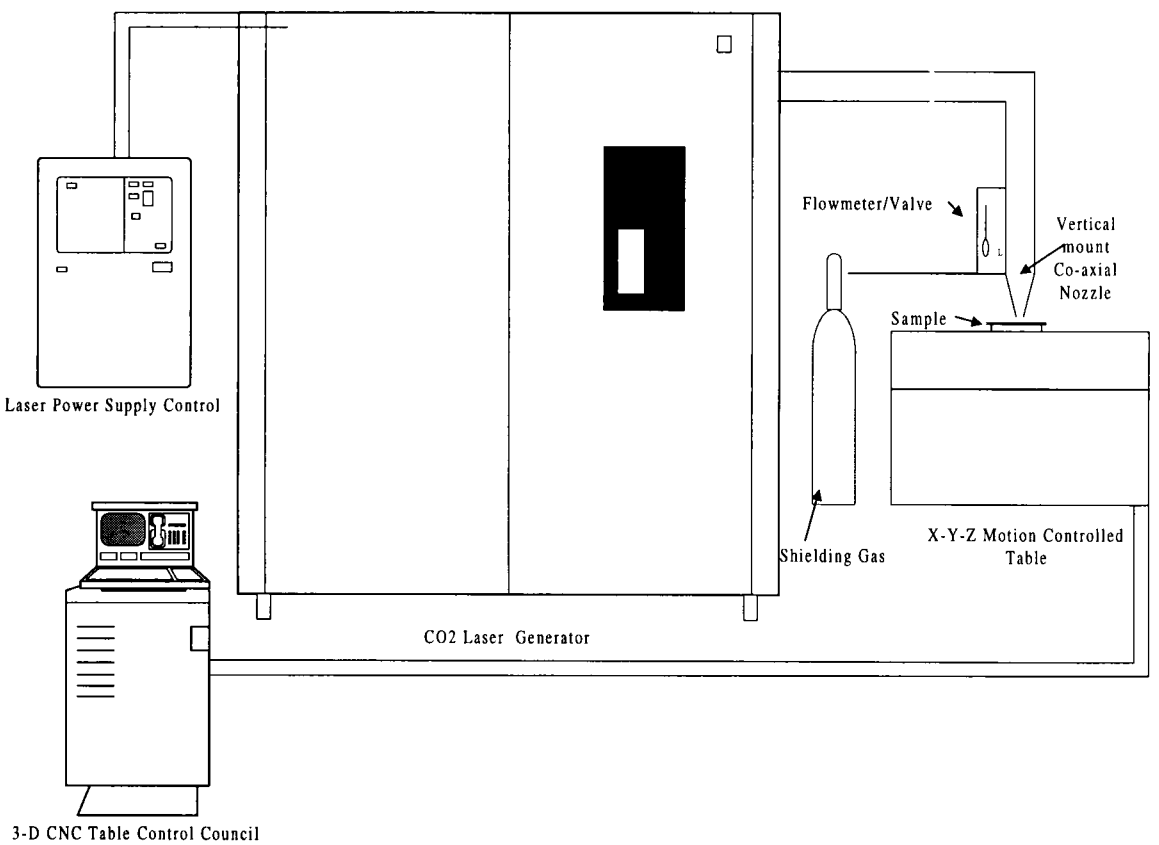

Figure 2.1 Layout of RS-3000 CO_2 laser and its control panels.

In our experiment we will use the TEM_{10} mode (Figure 2.2) of the RS-3000 laser. Although the cross section is non-uniform in shape, the fast beam advance on the surface would compensate for lack of intensity in the middle ring of the beam. With proper optics installed we can reduce the spot size from the 30mm diameter laser output to almost 300μm. Yet, to control the melt track width we can change the stand-off distance of the beam focus from the sample surface. In this case, a 10mm stand-off would provide an ~1mm width melt zone track in 2000W power setting on the surface of the sample. This melt track width is large enough to study the cross-section of the melt zone.

2.2 Continuous Wave Nd:YAG Laser

The active medium in the Nd:YAG laser is a synthetic single-crystal of yttrium aluminum garnet that has been doped with a low percentage of rare earth neodymium. The 1.06μm radiation is generated by transition of an excited electron between two energy levels of the neodymium ion. The excitation of this active medium is accomplished by broadband optical radiation from an intense arc lamp, which is coupled into the crystal. This process is called "optical pumping" and it is a very common way to pump solid sate material[1].

The crystal or rod, is grown to a maximum of 150mm in length. This growth size limitation and the problem rising from cooling larger rods dictate the design of lasers with multiple rods in series. Therefore, each rod is excited and cooled separately. The HLP-

3000 Nd:YAG laser (Figure 2.3) uses three of these rods to achieve its 3000W maximum output.

The shorter wavelength of Nd:YAG laser, and its Gaussian beam profile (TEM_{00}, Figure 2.4), packs more energy and better coupling on the surface of steel at room temperature and above than CO_2 laser. The reported power needed to melt and iron-based material with the Nd:YAG wavelength is around one order of magnitude smaller than the power using the CO_2 laser[4]. More aspect of energy absorption in different temperature of CO_2 and Nd:YAG lasers will be discussed in the Chapter 3.

The fiberoptic beam delivery system consists of a lens set which focuses the laser beam into fiber, a fiberoptic cable assembly (150mm long), and an end-effector (output lens set) which focuses the light transmitted through the fiber onto the workpiece. The normal fiber size used with the HLP-3000 laser is 600μm in diameter, therefore the minimum spot size would be ~300μm in diameter.

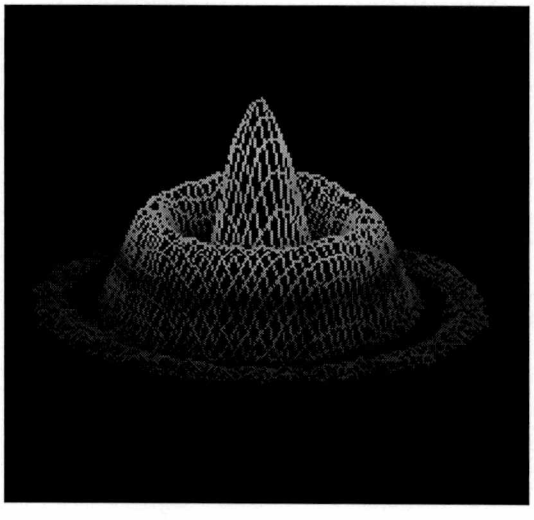

Figure 2.2 3-D cross section of TEM_{10} mode laser beam. Bright colors indicate higher intensity [8].

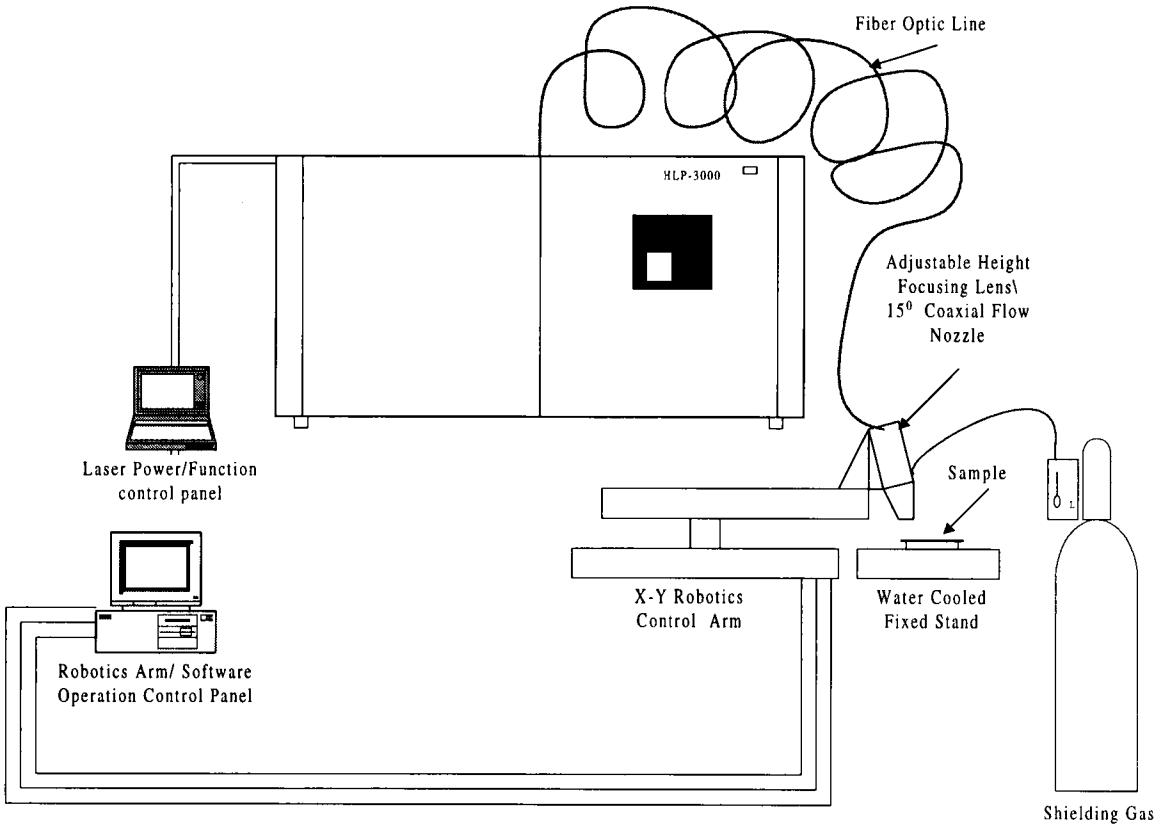

Figure 2.3 Lay-out of Hobart HLP-3000 laser and robotic arm assembly.

Beam quality changes during transport in the fiberoptic media and as a result the original Gaussian profile could be distorted to a "top-hat" distribution (Figure 2.5). If the top-hat is not distorted too much and still keeps a good amount of spherical symmetry the combined traverse speed and the beam intensity profile would offer a homogeneous melting surface. Later in the Chapter 3 we will discuss further some of the beam profile approximations and assumptions.

2.3 Video Image Processing

To investigate the interaction of the plasma with the surface of the steel samples a video camera was installed on of the set-ups (Figure 2.6). The system consists of a CCD video camera, zoom and proper ND (neutral density) filters on a special adjustable arm close to the samples. The video was recorded on a VHS video tape and later it would be analyzed by video capture system utilizing a Silicon Graphics Indigo (SGI0 IMAPCT workstation. The SGI workstation could capture almost all of the 30 frame per second images recorded on the VHS tape using Indigo Video board.

The Elmo model TSN401 CCD color camera was used to record the plasma plume above the samples. The shutter speed could go down to 1/10000 of a second using shutter switch panel. The ND filter is installed to decrease the plasma glare effect on camera's CCD detectors to enhance the image sharpness.

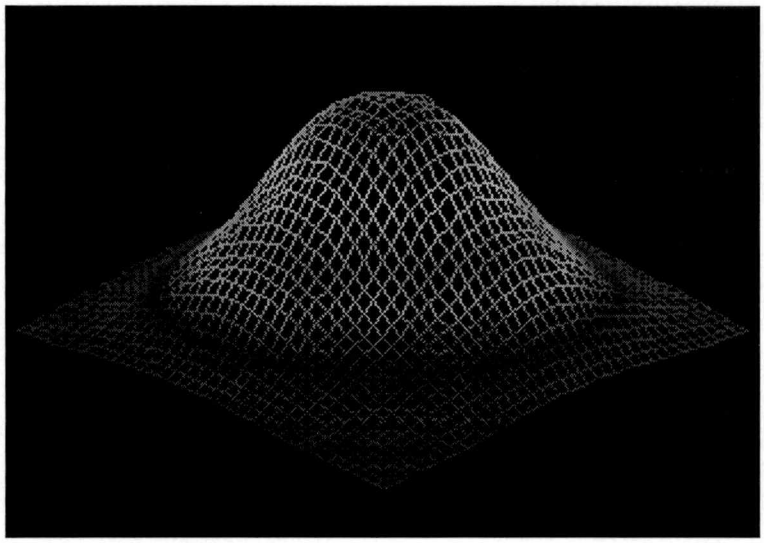

Figure 2.4 Gaussian TEM_{00} laser beam profile, brighter colors indicate higher intensity.

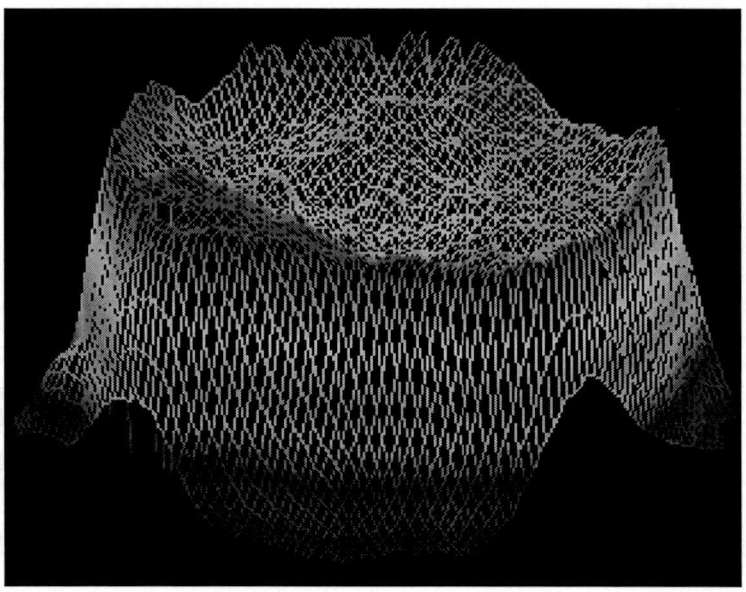

Figure 2.5 Top-hat distribution of Nd:YAG laser beam coming out of the fiber optic[8].

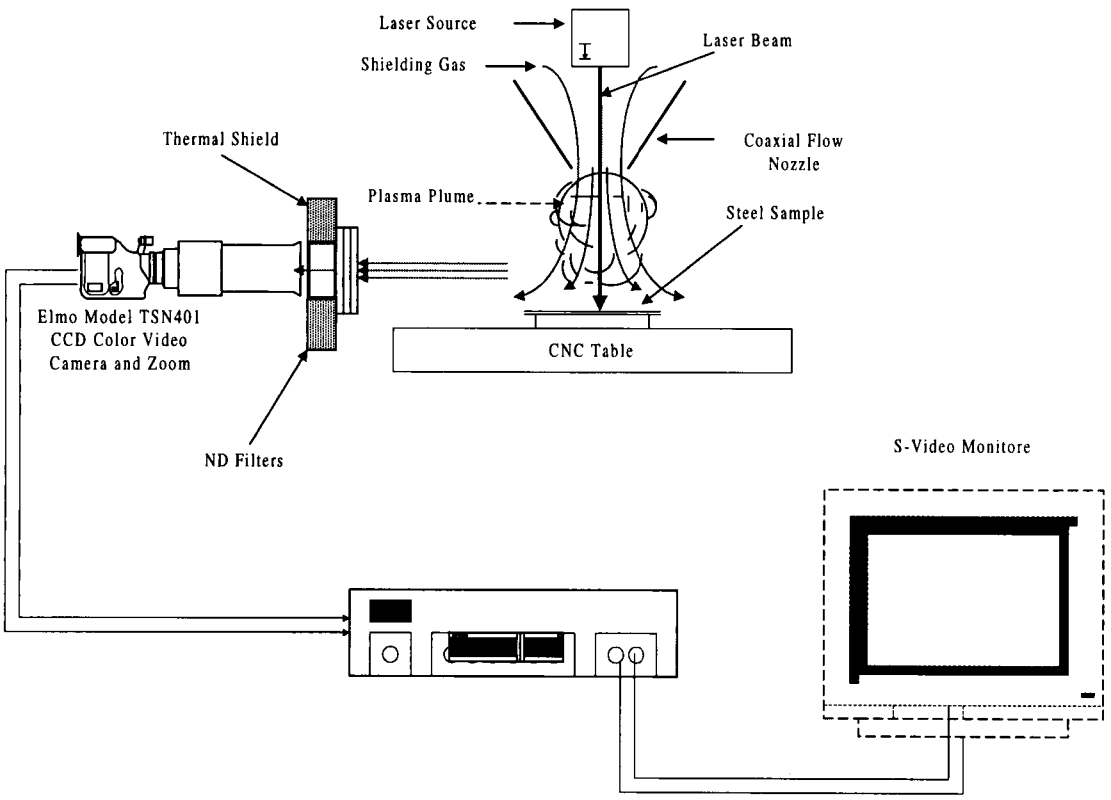

Figure 2.6 Lay-out of plasma recording.

2.4 Sample Set-up

- Samples were cut from ¼" 1010 steel sheet to 2"×6" slabs, then sand-blasted to remove any coating or oxidation on the surface (figure 2.7a). After setting the laser marker (a red He-Ne laser marker) on the edge of the sample, we set the power to 2000W. This power setting was constant through all of our experiments. For the CO_2 laser the coaxial nozzle perpendicular to the sample's surface, while for the Nd:YAG laser the coaxial and therefore the beam has a 15^0 angle with the normal to the surface.

- In the YRD-66 and RD-66 and 65 samples, the scan speed remains constant at 1500mm/min. RD-64 data are taken with several scan speeds of 1500mm/min, 2000mm/min, 2500mm/min and 3000mm/min total of four different scan speeds (see Appendix C for all the speed settings). Only argon gas was used for RD-64 samples to emphasize the effect of scanning speed on the melt zone depth while, in RD-66 and YRD-66 the main concern was to find the effect of different shielding gases.

- Shielding gas was stepped at 5 scale units starting at 5 and ending with 60 scale units (5,10, 15, 20, 25, 30, 35, 40, 45, 60) with a total of 12 speeds per each shielding gas. The shielding gas is turned on a few seconds before the laser hits the surface with maximum 2000W power. This in some extent insures the abundance of shielding gas over the sample.

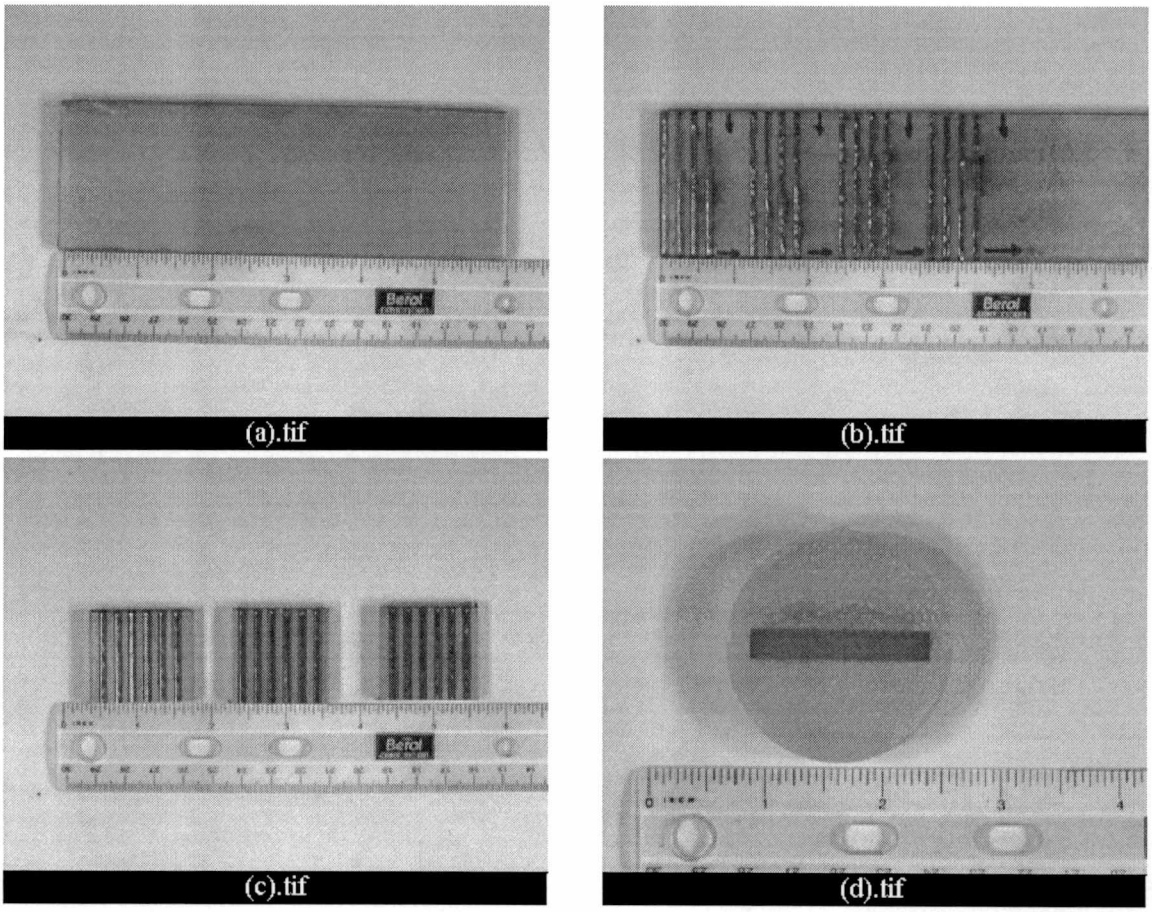

Figure 2.7 Processing of steel samples: 6x2 slab(a) multiple track run on the sample(b) track groups cut for mount (c) sample mounted (d).

•Samples were set on the processing table without clamping. The time interval and the distance between each track (5mm for each tracks and 10mm for each group of 6 or 4 tracks) help to cool down the sample so there is no risk of bending the steel slab during processing because of uneven heating by the laser. Therefore, the samples are not cooled.

2.5 Post Processing

After processing of the sample by laser beam (Figure 2.7b), each group of tracks were then cut and mounted (Figure 2.7c). After mounting the samples on a resin base holder (Figure 2.7d) the cross sections were polished by 100, 200, 300, 400 and 600 sand papers. Then, the samples were polished one more time by 1 and 0.1 micron emulsified liquid. To extract the melt zone and heat affected zone from the substrate, the polished cross sections were treated with an etching solution, 10gram$(NH_3)_2S_2O_8$ ammonium per sulfate + 100 ml H_2O, using cotton swabs and then washed and air dried. At this stage the samples were ready to be measured under microscope.

2.6 Video Image Measurement

To measure the HAZ and the MZ of the cross-section of the tracks, a Nikon microscope with a CCD camera was used. The CCD has an interface with a QuickCapture video board. The QuickCapture frame grabber board plugs directly to an extension slot inside the Macintosh II computer. Using NIH*Image* software, the cross

section area of processed tracks could be measured. Spatial calibration provides real world area and length measurements.

A total of six measurements was performed for each track under microscope. These include HAZ depth and width, MZ depth and width (Figure 2.8), HAZ area and MZ area. Therefore, one measurement was taken per each data point. See Appendix A for data entry of measurements.

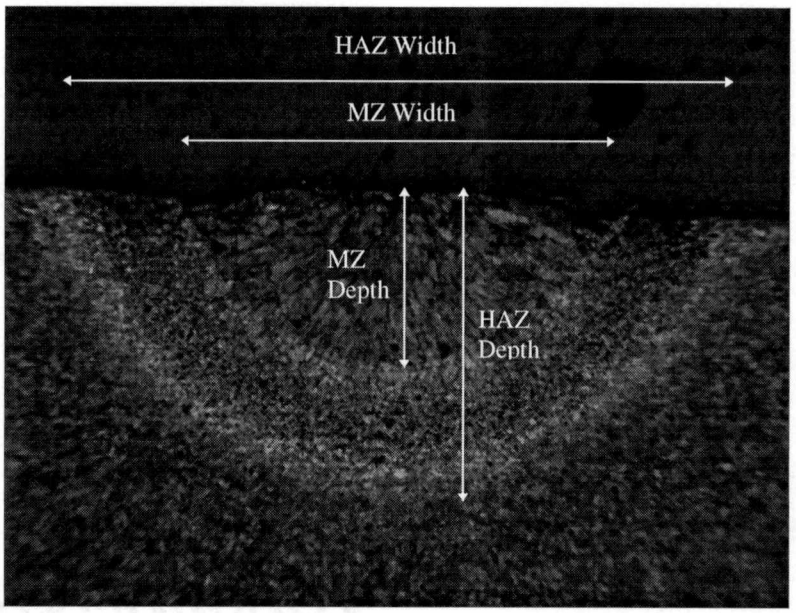

Figure 2.8 Measurements of track cross-section.

CHAPTER 3

LASER BEAM CHARACTERISTICS AND ASSUMPTIONS

3.1 Absorptivity of Metal

The absorptivity of a material is an essential factor effecting LSP especially since absorptivity increases with increasing temperature[13]. The absorptivity also changes with the phase and the surface condition of the sample[12]. However, the surface condition becomes less effective on the energy absorption in the case of surface melting processes since the surface of metallic samples melts very quickly when high power laser radiation is applied. For an opaque solid, the fraction of incident radiation absorbed is[4]:

(3.1) $A = 1 - R_0$

Where A is the absorption and R_0 is the reflectivity at normal incidence. For a gray-body radiation the Stefan-Boltzmann equation including emissivity as a constant factor is:

(3.2) $E = \alpha\sigma T^4$

where E is radiative energy and σ is Stefan-Boltzmann constant and α is the emissivity (for black-body radiation α is 1). In our discussion emissivity is considered to be the same as absorption.

Reflectivity at normal incidence for a complex refractive index $m = n - ik$ is:

(3.3) $$R_0 = \frac{(n-1)^2 + k^2}{(n+1)^2 + k^2}$$

The absorption is then:

$$(3.4) \quad A = \frac{4n}{(n+1)^2 + k^2}$$

Absorption is a function of temperature T and wavelength λ and in general, n and k (refraction index components) for metallic materials are also functions of T and λ. At longer wavelengths, n and k both increase rapidly with λ and A decreases to a small fraction of its value at shorter wavelengths. This means that absorption is generally higher at lower wavelengths[4]. In the following sections we will discuss two methods for estimating the absorption by metals of various wavelengths.

3.2 Absorption of Metals, The Hagen-Ruben Method[12]

Experimental data on absorptivity are lacking due to difficulties in measuring this property at high temperature. Therefore, a theoretical approximation will be used in measuring absorption at the melting temperatures of low carbon steel and iron. The Hagen-Ruben relationship will be used to determine the absorptivity of metals at high temperatures. This relationship can be expressed as:

$$(3.5) \quad A = \left(8A\omega\rho_m\right)^{1/2} \text{ or } A = 365.15\left(\frac{\rho_m}{\lambda}\right)^{1/2}$$

where $\omega = 2\pi c/\lambda$ where λ is the wavelength of the laser radiation in μm and ρ_m is the d.c. resistivity of metal in units Ω-m.

Arata and Miyamato[28] calculated the absorptivity of metals for Fresnel absorption of a CO_2 laser and Nd:YAG laser to be:

(3.6) $A_{CO_2} = 112.2(\rho_m)^{1/2}$

(3.7) $A_{YAG} = 354.67(\rho_m)^{1/2}$

where A_{CO2} is the absorptivity of a metal for the CO_2 laser wavelength radiation, A_{YAG} is the absorptivity of a metal for Nd:YAG lasers and ρ_m is:

(3.8) $\rho_m = 10^{-8}(a+bT)$

For iron the values of a and b for different temperature are listed in the Table 3.1:

Table 3.1 Variation of resistivity of iron with temperature.

Temperature Range[K]	a	b
273-1060	-80	0.175
1060-1808	69.5	0.035
1808-1973	80	0.033

Using the data in Table 3.1 and Equations 3.6 and 3.7, we can calculate the absorptivity of radiation by iron during laser processing with CO_2 and Nd:YAG lasers (Figure 3.1). Above the melting temperature, T_m = 1810 K, the absorption of radiation by iron for the Nd:YAG and the CO_2 are significantly different. The ratio A_{YAG}/A_{CO2} is 3.16. This indicates a higher efficiency for Nd:YAG operation. Later in Chapter 5 on data analysis we will compare these theoretical values with experimental data.

3.3 Absorption of Metals, the Duley Method

The temperature dependence of absorption, A, is calculated from this expression[14]:

(3.9) $A\ (10.6\ \mu m) = 11.2[\rho_0(1+\gamma T)]^{1/2} - 62.9[\rho_0(1+\gamma T)] + 174[\rho_0(1+\gamma T)]^{3/2}$

where ρ_0 is the resistivity at 20^0 C and γ is the coefficient of resistivity change with temperature T^0 C.

Equation 3.9 only represents the absorption for the CO_2 laser wavelength, but Duley has calculated the emissivity (absorption) of both iron and mild steel[4] and from Figure 3.2 it can be seen that the absorption values for iron and mild steel are very similar. Later this will help us to replace absorption values of mild steel with those of iron which simplifies future calculations since iron thermophysical data for different temperatures are more readily available than low carbon steel. Equation 3.9, unlike the Hagen-Ruben relationship (Equation 3.5), has real values for absorption at temperatures lower than 500 K yet, it has no comparison between CO_2 and Nd:YAG absorption. Moreover we are more interested in the absorption at higher temperatures.

3.4 Beam Quality

Beam quality denotes the degree of perfection of an actual beam relative to an ideal Gaussian beam. This ideal beam has a symmetrical Gaussian intensity profile (Figure 2.4b) and a flat phase front at its waist. The size of a Gaussian profile is arbitrarily defined as the diameter at which intensity has decreased to $1/e^2$ of its central

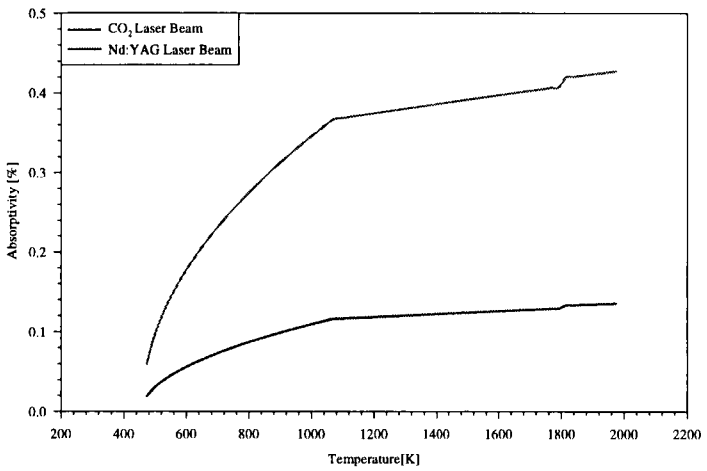

Figure 3.1 Absorptivity of the CO_2 and Nd:YAG lasers radiation by iron using the Hagen-Ruben relationship[1]

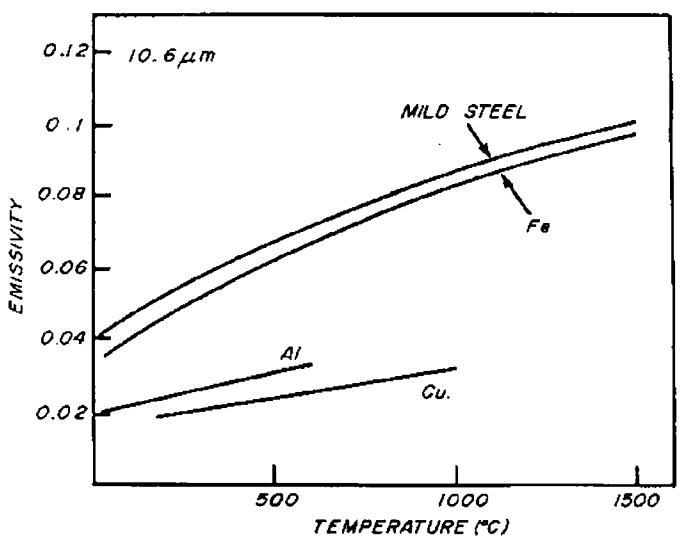

Figure 3.2 Absorption (emissivity)of several material including mild steel and iron in different temperatures[4]

value. A Gaussian beam constitutes the longest possible Rayleigh range (Equation 3.10) and smallest possible far-field divergence (Equation 3.11)[15].

(3.10) Rayleigh range = $\frac{\pi \cdot d_0^{\,2}}{4\lambda}$

Where d_0 is the diameter of beam at the waist. At this range, the diameter of the beam has increased by only 41%, and the central intensity decreased by a factor of 2. Beyond this range, the beam will eventually expand at a constant far-field divergence.

(3.11) Far-field, full-angle divergence = $\frac{4\lambda}{\pi \cdot d_0}$

More over this beam maintains its Gaussian profile at all distances from the waist. Such a beam is called a "diffraction-limited" beam.

All practical beams will have shorter Rayleigh ranges and larger far-field divergence. This could be from distorted profiles at the waist, or the existence of higher order TEM modes, or both. The ratio of actual beam divergence to the diffraction-limited divergence is called "beam quality".

Thermal and energy distribution of a beam on metallic surfaces are a well-studied subject and energy distribution of the laser beam is often considered to have a Gaussian profile. The assumption of a Gaussian thermal and energy distribution of the laser beam on the sample is a reasonable approximation despite the different beam profile of the laser source (Figure 2.2&2.5). At the focus, the beam still keeps the signature beam profile of

[1]-For values smaller then 473 K of surface temperature T, with a and b values from table.3, the A values are imaginary and therefore not shown.

the source (distorted top-hat or TEM_{10}). Using the far-field approximation criteria[27] in Equation 3.12, assuming a flat phase beam front, a safe defocus distance from the focal point of the lens can be established.

$$\frac{r_0^{\,2}}{2\lambda \cdot D_f} \langle\langle 2\pi \tag{3.12}$$

where r_0 is the beam radius at focus, λ is the wavelength of the laser beam and D_f is the approximate defocus distance.

Based on a top-hat beam profile and flat phase front, for a 10mm defocus the criteria is met even for a focal point as big as 300μm beam radius(Figure 3.3), which lead to the assumption of diffraction on a circular aperture.

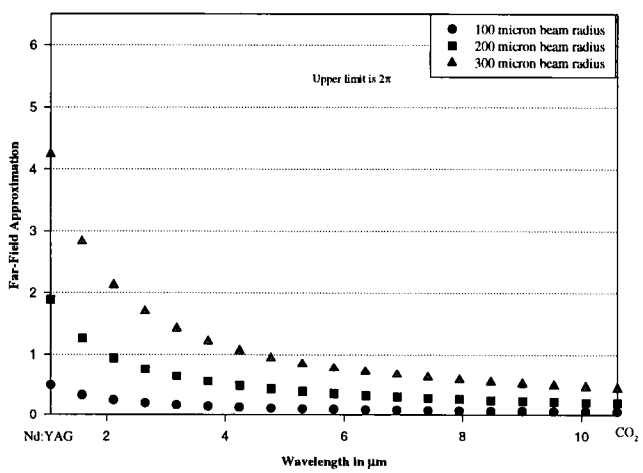

Figure 3.3 Beam radius effect on far-field approximation for a 10mm defocus.

Assuming a Fraunhofer diffraction approximation for a circular aperture, in the far-field zone the image on the defocus plane is an Airy disk, which is a good approximation of a Gaussian distribution. Therefore, if the original beam is roughly symmetrical, for most of the laser TEM modes and profiles the Fourier transform in the far-field zone converts the beam profile to a Gaussian approximation.

3.5 Energy Absorption for Gaussian Beam.

The power density I is given by[15]:

$$(3.13)\quad I = I_0 \exp(\frac{2r^2}{r_0})$$

$$(3.14)\quad I_0 = \frac{2P_{Temp}}{\pi \cdot r_0^2}$$

Where P_{Temp} is the power needed at different surface temperatures in watts, I_0 is the power density at the center of the Gaussian beam, r is the radial distance from the center of the beam, and r_0 is the beam radius. The radius r_0 is the distance at which the power density has dropped to $1/e^2$ or 13.5% of the value at the center of the beam which means 86.5% of total power is contained in spot of r_0 size.

Heat transfer calculations show the limiting temperature at the center of a Gaussian focal spot on a bulk target is[4]:

$$(3.15)\quad T = \frac{A \cdot I_0 \cdot r_0 \pi^{1/2}}{K}$$

Where K is thermal conductivity[16] and A is the absorption[2].

Using Equation 3.14 and 3.15 (replacing I_0) we can therefore obtain P_{temp} (Equation 3.16) for the CO_2 and Nd:YAG wavelengths as a function of temperature at the center of a Gaussian focal spot in Figure 3.4. Therefore, to achieve a given temperature, the CO_2 laser has to deliver more power to the sample than the shorter wavelength Nd:YAG which indicates the higher efficiency of shorter infrared lasers.

$$(3.16) \quad P_{Temp} = \frac{\pi \cdot r_0 K}{2A \cdot T}$$

The Equation 3.15 is for steady state (t = ∞) at the surface of the sample and the power absorbed model is based on a drilling (non-moving) point source on the surface of the metal. In our experiment we use a moving source or a moving sample. Despite the simplicity of the drilling model for a point source at the center of the beam, we can estimate for a given temperature how much power is actually absorbed by the metal. Later in the chapter on heat transfer (Chapter 4) we will introduce a model with a moving laser source.

[2]- Absorption values for different temperatures are calculated from equation 3.5 and 3.6, see Figure 3.1.

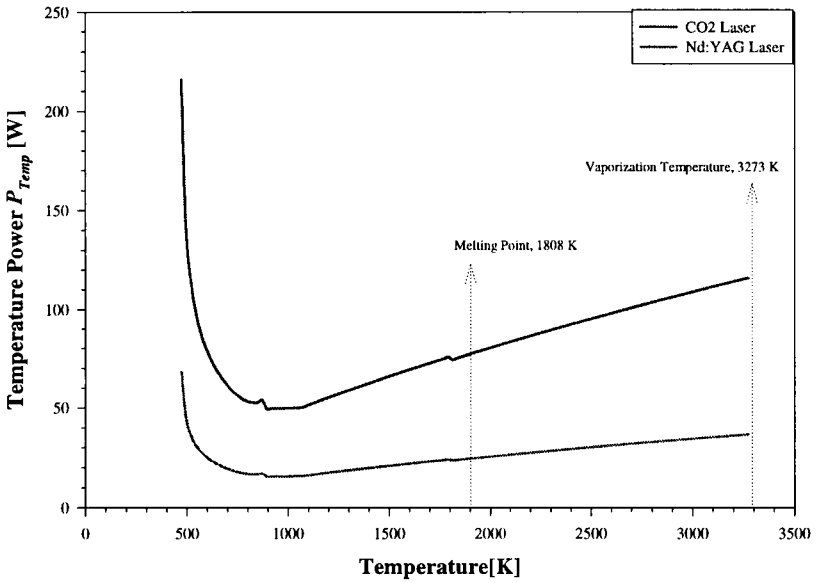

Figure 3.4 Absorbed power CO_2 and Nd:YAG laser for iron at the center of a 300 μm Gaussian beam.

CHAPTER 4

HEAT TRANSFER

4.1 Introduction[20]

There have been many studies of the depth of the MZ with varying emphases on experiments, modeling, and simulations. In one extreme, the experimental studies statistically analyze large numbers of measurements in order to develop a master correlation for the purpose of prediction. For these, the laws of physics play little or no role in the analysis as the correlations are largely empirical. A disadvantage is that, without insight into which groups of variables should be plotted and versus which other groups. The resulting correlation tends to be complicated and often conceals the dominant physical effects.

At the other extreme, the equations of mass and energy are solved computationally for temperature and scan velocities, etc., as a function of position and time. For these, even if all information of the thermophysics has been accounted for and exact predictions are possible, the time consuming and complicated nature of simulation limits their application. For example, Cline and Anthony[26] have used numerical method to solve for the isotherms and melt depths. There are other examples of numerical approaches using 2D or 3D, single track or multiple tracks of which none will be discussed here since this approach requires extensive amounts of computer

programming. Therefore, using some analytical solution maybe considered in some cases.

Explicit exact solutions can be obtained by classical heat transfer methods. Heat transfer in a solid metal substrate is governed by the energy the equation, which for uniform scan velocities and constant material properties is linear in temperature with constant coefficient. Carslaw and Jeager[21] have a well-known catalog of such solutions. In another well-known article, Rosenthal[19] applies these methods to metal treatments with a moving heat source, and illustrates how to interpret various exact solutions in analyzing measurements in welding applications. For general boundary conditions computation using a boundary-element formulation has proved effective. Nonetheless, the challenge remains to choose the appropriate solution and interpret it properly. Therefore, several different models will be introduced in this chapter each of which would provide a simple solution to the effects of laser power and scan speed in our experiments.

4.2 Convection Effect[20]

When a melt pool exists, the heat transfer generally couples with fluid motion across a solidification front of an unknown shape which itself may be influenced by the behavior of a melt-gas interface of an unknown position. Nevertheless, even when there is a melt pool with convection, its depth may be dominated by heat transfer within the solid substrate. As long as the melt pool depth is relatively shallow and longer than the

laser beam width with a very good approximation we can neglect the convection effect[20,5]. Indeed, for the range of parameters typical for laser surface treatment, with or without existence of the melt pool, the penetration depth is principally determined by conduction of absorbed energy throughout the substrate. Consequently, we ignore the effect of melt pool convection in our discussion and present three models for depth of melt zone.

4.3 Depth of MZ Carslaw and Jeager Model[21]

4.3.1 Infinite Sheet

The analysis of thermal effects involves the solution of the three-dimensional heat transfer equation when heat input is limited to a surface source. Heat transfer from this source initiates a melting wave that propagates into the bulk material. Stable propagation of this wave will occur while the surface temperature is less than the boiling temperature. Therefore, the melt depth can be calculated from the speed of the melting wave and the time interval between T_m (melt temperature) and T_v (vaporization temperature) at the front surface.

Assumptions made for this calculation are as follow

(a) The physical characteristic of the metal, i.e., k, A and K are independent of the temperature.

(b) The scanning speed v and the total laser power P, are constant.

(c) The laser source is considered as a point source.

Considering an infinite half space, as shown in Figure 4.1, a laser source emitting P power is uniformly scanning surface of an infinite half space slab with scan speed v. For a moving surface heat source, the simplest solution is obtained when a point source is assumed. In this case the temperature distribution is:

$$(4.1) \quad T(r) = \frac{AP}{4\pi \cdot K \cdot r} \exp\left[-\frac{v(r-x)}{2k}\right]$$

with

$$(4.2) \quad r = \sqrt{x^2 + y^2 + z^2}$$

and v is the speed in x direction (direction of movement).

Using Equation 4.1, also known as the Rosenthal model, for a 2000W laser power and 1500mm/min scan speed we can predict the temperature profile for a heat source using a CO_2 laser ($A=A_{CO2}$) or Nd:YAG laser ($A=A_{YAG}$).

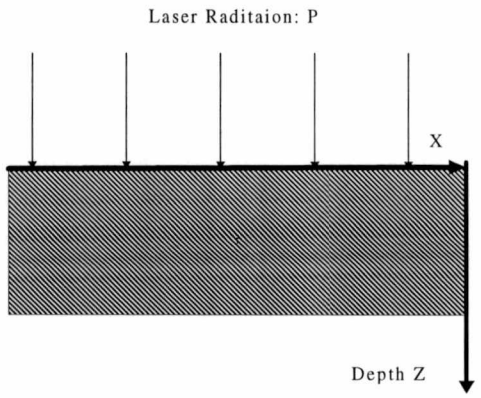

Figure 4.1 Infinite half space, with an edge on the right and infinite length at the left and the bottom of the plate.

To make the calculation possible for a two-dimensional contour we assume $x = 0$. In this case, a temperature diagram of the heated area cross section perpendicular to direction of beam movement could be studied. Using Equation 3.6, A for CO_2 the absorption is averaged around 0.13 for a temperature range of around 1000K to 2000K (Figure 4.2).

The absorption for the same temperature range, using Equation 3.7, is 0.41 for Nd:YAG laser. Therefore, there is a substantial change in the position of the 1500K - 2000K isotherm lines for the two wavelengths. This suggests, as expected, that the stronger absorption at the shorter wavelength Nd:YAG creates a much bigger MZ (Figure 4.3).

More importantly, the isotherm pattern, especially in the Nd:YAG case, suggests a temperature profile close to T_v. If the energy assumption in this calculation is correct, then the material loss due to excess heat is inevitable.

The melting temperature of iron, T_m, is 1808K and the vaporization temperature, T_v, is 3273K. Looking at Figure 4.2, the area reaching temperatures above T_v is very small. Therefore, a very small loss of material will occur due to vaporization. For Nd:YAG on the other hand (Figure 4.3), the region of $T > T_v$ is much greater than that created by the CO_2 laser. This could lead to a large amount of material vaporization in the center of the tracks.

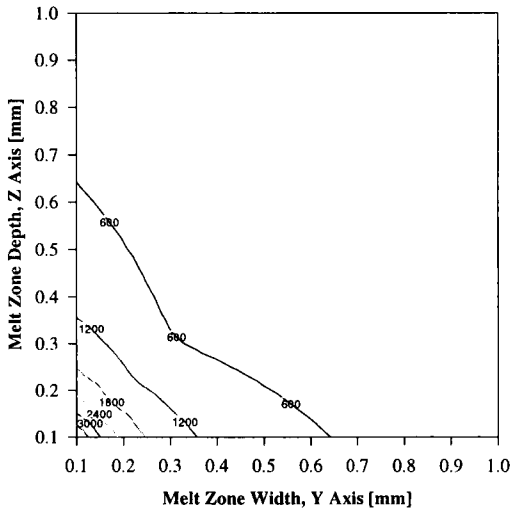

Figure 4.2 Temperature isotherms of a processed frontal cross-section using a 2000W CO_2 laser beam and 1500mm/min scanning speed with Carslaw-Jeager model.

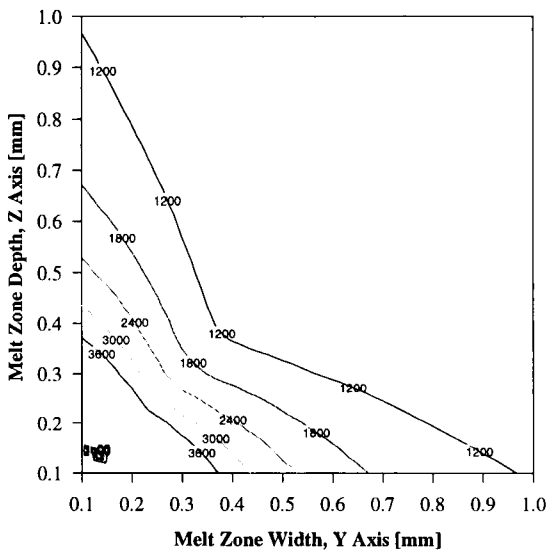

Figure 4.3 Temperature isotherms of processed frontal cross-section using a 2000W Nd:YAG laser beam and 1500mm/min scanning speed using Carslaw-Jeager.

The mathematical model in Equation 4.1, neglects the contribution of several physical phenomena including shielding gas cooling effect, plasma shielding, radiation heat loss from the surface and latent heat. These parameters could effectively reduce the absorbed power by the melt zone thus creating a smaller MZ with a lower maximum temperature very close to the center of the point source. We will discuss some of these phenomena later in chapter 5 on data analysis.

4.3.2 Correction for Finite Thickness

Suppose that the slab is $0 < z < L$ and that it moves with velocity v parallel to the x axis, with a power source P and no heat loss from surface of the slab. This is the same problem as the first case, except for finite thickness of the slab (Figure 4.4).

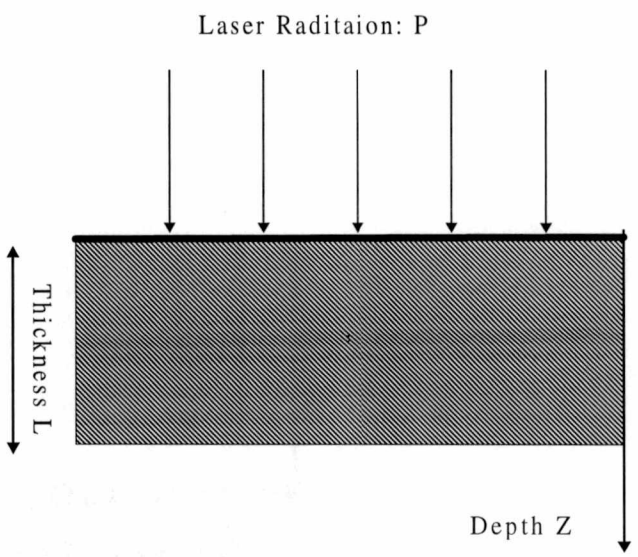

Figure 4.4 Finite thickness slab

For this problem the expression for the steady state temperature due to the point source is:

$$(4.3)\quad T(r)=\frac{AP}{2\pi\cdot K\cdot L}\cdot\left\{K_0\left(\frac{vr}{2k}\right)+2\sum_{n=1}^{\infty}K_0\left[\frac{vr}{2k}\left(1+\frac{4k^2n^2\pi^2}{v^2L^2}\right]\cos\left(\frac{n\cdot\pi\cdot z}{L}\right)\right\}\exp\left(\frac{vx}{2k}\right)\right.$$

Where L is the thickness of the sheet, and K_0 is the zero order Bessel function. Although Equation 4.3 has a correction element for finite thickness, for a 1/4" thick steel slab this model offers very little change in the isotherms locations or shape compared to the Equation 4.1 (see Figure 4.5)

4.4 Depth of MZ for Rosenthal Method

Assuming $X = 0$ and $Y = 0$, we can solve Equation 4.1 for Z, and for a $T_m = 1808$ we can solve the equation for different scanning speeds as indicated graphically on Figure 4.6. As expected from the absorption factor in Equation 4.1, Nd:YAG offers enhanced melt penetration in comparison to CO_2 laser.

4.5 Depth of MZ and HAZ, Steen, Ehrhard and Schussler Model[21]

4.5.1 Assumptions

Assume the laser scans the substrate at a constant velocity v, and there is steady state behavior in a moving reference frame. The essential physics can be understood by

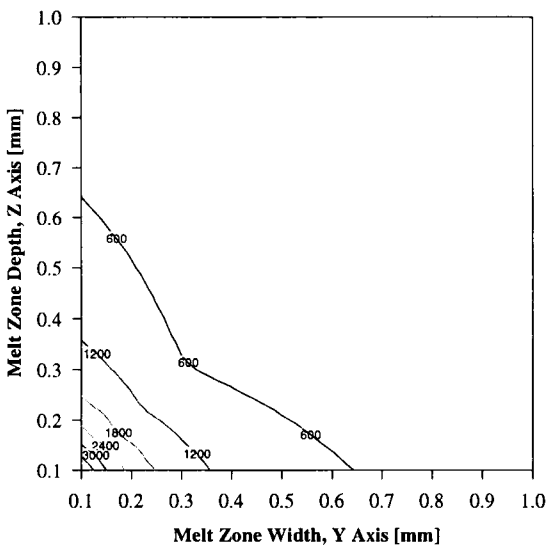

(a)

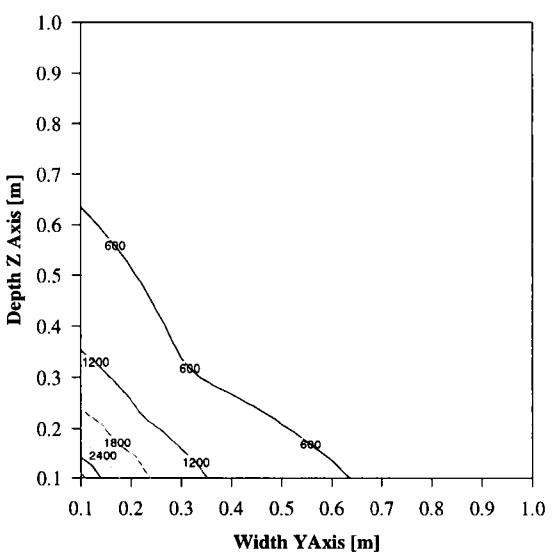

(b)

Figure 4.5 Isotherm modeled (a) with infinite thickness and (b) corrected isotherm for 1/4" thick steel slab for a 2000W CO_2 laser with 1500mm/min scan speed using Carslaw -Jeager model.

considering two-dimensional heat flow in the substrate, as might occur with a rectangular beam source aligned with its small dimension in the scan direction.

For simplicity, the absorbed power density, I, is assumed uniform across the beam. The applied laser power is modeled as a constant heat flux, consistent with the regime of experimental interest. Outside the beam profile, the surface is taken to be adiabatic, neglecting any radiative heat transfer and in keeping with the relatively poor thermal conductivity of an overlaying gas. Solid state transformations and any melting/freezing are assumed to take place in local equilibrium. Hence, they coincide with special isotherms. Variations of material properties with temperature in the solid substrate will be ignored. An important feature of the analysis is that the material properties in the transformation zone or in a MZ are not needed.

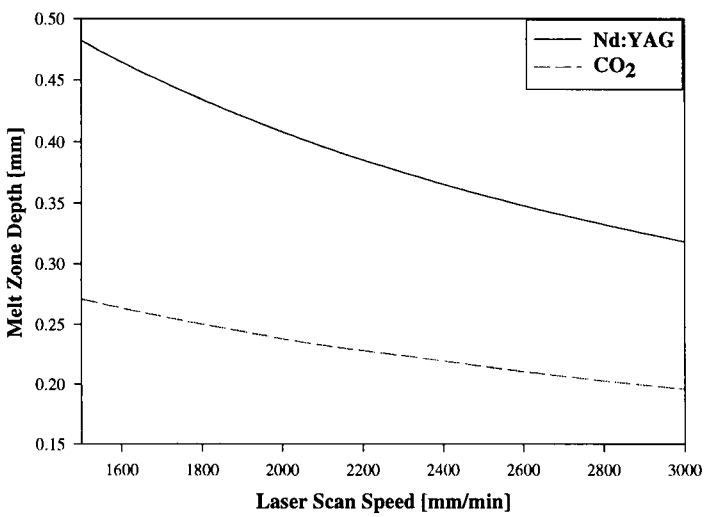

Figure 4.6 Melt penetration comparison of Nd:YAG and CO_2 lasers using Rosenthal method

Various scales of thermal penetration are shown in the Figure 4.7. Where d_{MZ} is depth of the melt zone, d_{HAZ} is depth of the heat affected zone, L is the sample thickness, T_m is melt zone temperature, and T_h is heat affected temperature, T_∞ is the far-filed temperature (temperature at the bottom of the slab), T_α is the transformation temperature and r_0 is beam radius.

Each of the depth dimensions is to be the maximum penetration depth of a particular isotherm. Although shown in nearly circular arcs, the isotherms in calculation and the experiments are distorted. Generally due to influences depending on the particular experiment (including convective effect of the solid substrate motion, heat-transfer condition at the top surface and laser beam profile) these distortion could vary.

The penetration zones of special interest are the MZ and HAZ. In metallurgical literature, the term "heat-affected zone" often refers to a transformation zone; a zone made visible through etching (Figure 1.4b).

4.5.2 MZ Depth

In this section, we assume the MZ penetration depth is an isotherm appropriate for equilibrium melting/freezing at the solidification interface (i.e., no undercooling) with no influence of interface curvature. Hence the melt depth, d_m, is just a penetration depth.

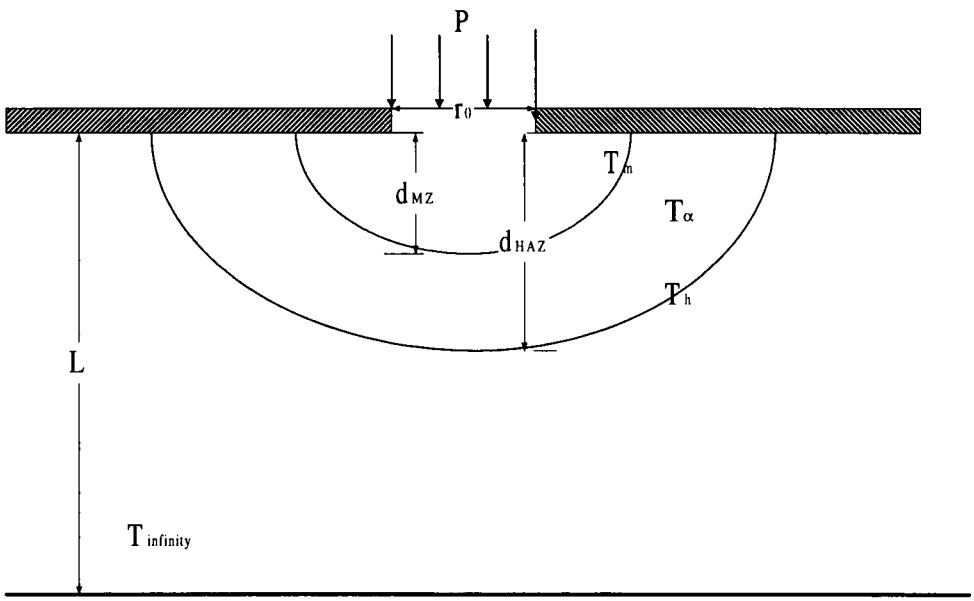

Figure 4.7 Sketch of penetration depths in an axial cross section of a laser treated workpiece. The beam is moving with speed v perpendicular to the page.

Furthermore, latent heat produced (melting) or absorbed (freezing) is negligible relative to total heat flux in the solid everywhere along the solidification front. This assumption is always true on the average over the total length of the solidification front since the total freezing must just equal total melting. Under these conditions, the heat flux into the solid is in local balance with the heat flux from the liquid at the solidification front[21].

A further assumption is that whenever a molten zone exists, the horizontal extent of the MZ (x and y axis) at the surface exceeds the beam dimension (MZ's maximum width > r_0). This insures there is no heat addition across the surface beyond the melt isotherm. For a relatively shallow MZ therefore the depth is:

$$(4.4) \quad d_{MZ} = \left[\sqrt{\frac{4}{\pi \cdot \frac{2vr_0}{k}}} - \left(\frac{T_m}{T\infty} - 1\right) \cdot \frac{1}{\frac{I \cdot A \cdot 2r_o}{KT_\infty}} \right] \cdot 2r_0$$

Which T_m = *1808 K*, T_∞ = *300 K* and power density I is $\frac{P}{\pi \cdot r_0^2}$. Using Equation 4.4, we can predict the MZ maximum depth for both CO_2 and Nd:YAG lasers (Figure 4.8)

4.6 Comparison of Two Methods

Equation 4.3 (Carslaw & Jeager) and 4.4 (Steen-Ehrhard) both offer d_{MZ} for different scanning speeds and laser surface absorption. What they cannot offer is the effect of shielding gas on the power factor, P, leaving absorption, A, the only power factor available (see section 1.3 & 1.4).

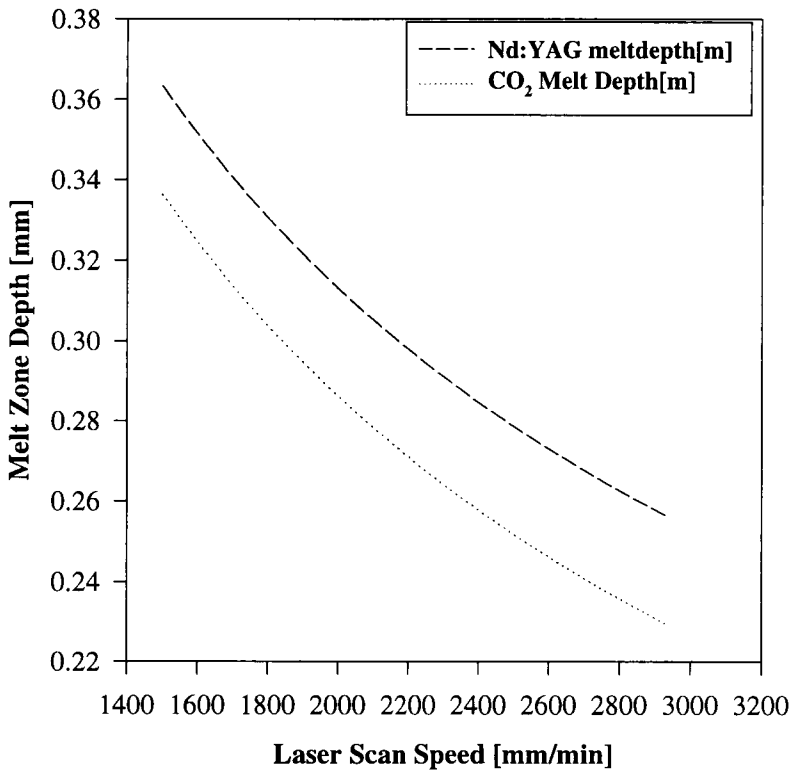

Figure 4.8 Melt zone depth using Steen-Ehrhard model, 2000W radiation for Co_2 and Nd:YAG lasers at different scanning speed.

Although both methods suggest that the d_{MZ} of the Nd:YAG is greater than of CO_2, there is a considerable disagreement in presenting this difference in the melt zone penetration. For example, for the Nd:YAG using both methods, Rosenthal predicts much greater penetration depth compared to the Steen-Ehrhard method (Figure 4.9a)

Changing from the Nd:YAG frequency to the CO_2 wavelength, the two methods reverse the melt penetration characteristic and, as seen in Figure 4.9b, the melt depth of Steen-Ehrhard is greater than that that of Rosenthal's. In Equation 4.1, Rosenthal, the Power factor ($A \times P$), is more dominant than that of Steen-Ehrhard, therefore, the change of absorption rate does not follow the same pattern as of Equation 4.4, Steen-Ehrhard. Since the Steen-Ehrhard model has some good agreement with new experimental results[20], we will use the Steen-Ehrhard melt depth for future analysis.

4.7 Energy Transfer by Plasma

There are at least two main physical effects responsible for energy transport to the workpiece. These are plasma collision and plasma emission.

4.7.1 Plasma Collision[23]

The workpiece gains energy by absorption and inelastic reflection of plasma particles. For simplicity it is assumed that all electrons, ions and neutral atoms from the plasma colliding with the surface are absorbed. In turn, the surface at the appropriate

evaporation temperature releases as many neutral atoms as necessary to match the absorbed particles in order to keep the net mass ablation at the surface zero.

The energy gain of the workpiece per exchanged neutral particle, known as heat conduction, is:

(4.1) Heat Conduction: $\frac{3}{2}k_B(T_n - T_s)$

Where T_n is plasma temperature, T_s is surface temperature and k_B is Boltzmann's constant.

4.7.2 Plasma Emission

The second important energy transfer effect is the radiation absorption at the surface of the melt by the photons emitted by the plasma. This is especially favored by the fact that the radiation emitted by the plasma has a much smaller wavelength than both the Nd:YAG and CO_2 lasers' wavelengths and therefore the Fresnel absorption coefficient of the metal is significantly higher for this kind of radiation[23]. The energy flux density of the radiation, however, is strongly linked to the energy flux density emitted by a black body at a temperature which can be describe Stefan-Boltzmann law (energy = σT^4). This is applicable only in the case of plasma in equilibrium described by a single temperature.

4.8 Effect of Shielding Gas on Plasma

One of the purposes of the high-speed shielding gas jet employed in laser processing is to blow away the plasma that forms above the melt surface. The use of this inert gas does not, however, succeed in removing all of the plasma with the result that the plasma scatters a part of the incident laser beam. This has the effect of reducing the efficiency of coupling of the laser power to the workpiece. Another source of energy loss arises from the flux of plasma that escapes from the melt surface. The residual laser power then has to be supplied to the workpiece by energy transfer from the plasma as well as by direct absorption of laser light at the surface of melt.

4.9 Plasma -Enhanced Coupling[5]

It is well established that the fraction of beam flux absorbed in metals increases above a certain threshold irradiance (Figure 5.1b). The increase tends to be particularly large for lower wavelength infrared lasers.

A typical sequence of events might be as follows. First, the material is heated to the point of evaporation by normal absorption. The plasma close to the surface is partially ionized and begins itself to absorb significantly. Then, a stationary plasma layer close to the evaporation surface forms. The temperature of the near-surface plasma is typically around 1 to 3 eV. Energy from the plasma can now be transferred to the dense phase by any of the three mechanisms:

1. Normal electron heat conduction

2. Short-wavelength thermal plasma radiation which is efficiently absorbed by the metal.

3. Condensation of vapor forced back to the surface by the plasma pressure.

These mechanisms provide an additional heat flux to the dense material, which may or may not exceed the loss of absorbed power due to plasma.

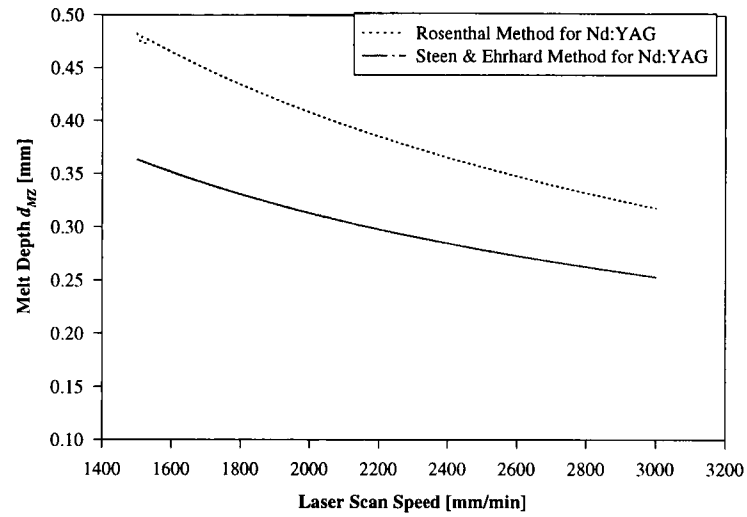

(a)

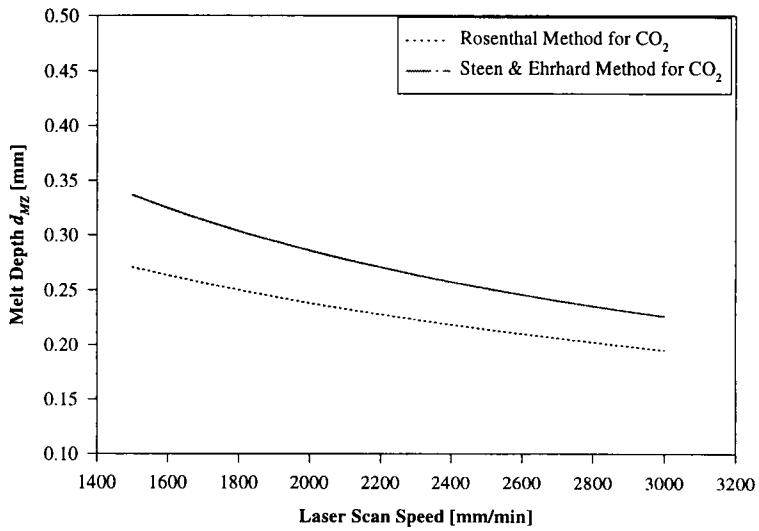

(b)

Figure 4.9 Melt depth of Rosenthal vs. Steen-Ehrhard method, (a) for Nd:YAG laser, (b) for CO_2 laser using 2000W laser beam.

CHAPTER 5

DATA ANALYSIS

5.1 Effect of Shielding Gas Mass Flow

When processing with a laser, the solidifying material has to be shielded against oxidation as in traditional welding. With helium and argon being the most widely used shielding gases since they are inert and do not react with the liquid weld metal[10].

While discussing the parameters affecting MZ size in LSP, the effect of shielding gas in the mathematical models was ignored. The lack of literature in the formulation of shielding gas effects makes it difficult to introduce a mathematical solution. However, the type and mass flow of shielding gas are important factors in enhancing or reducing the theoretical value obtained by different heat transfer models (Figure5.1). Generally as our data indicates, as the mass tranfer of shielding gas on the sample increases so does the size of the MZ.

5.2 Effect of Scanning Speed

As mentioned in the section 4.4.II, the scanning speed has a substantial effect on the melt depth (in Figure 4.7, this effect is shown from 1500mm/min to 3000 mm/min).

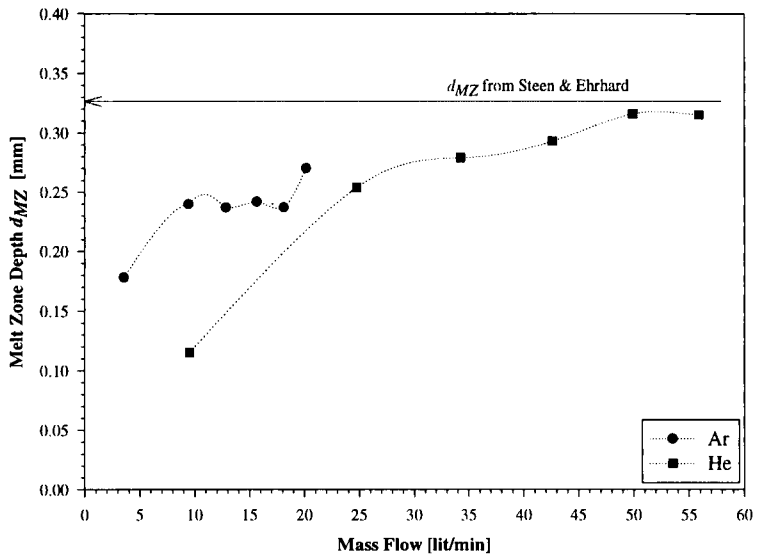

(a)

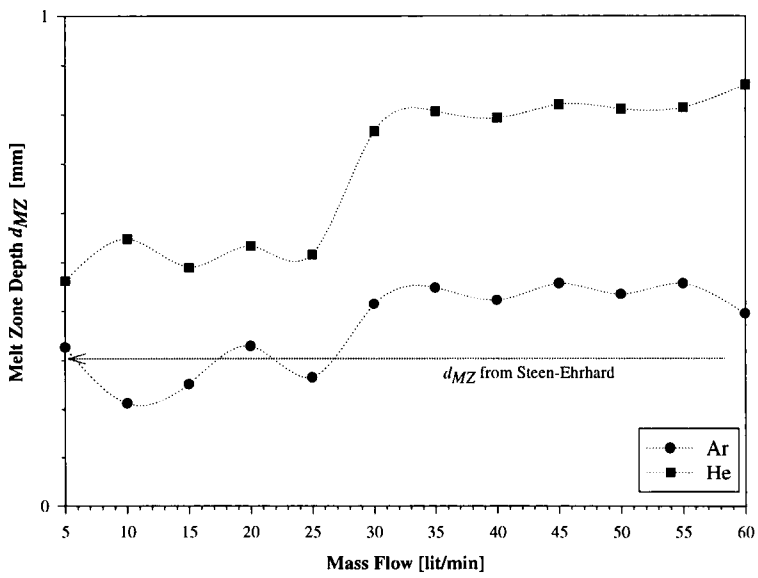

(b)

Figure 5.1 Effect of shielding gas mass flow (a) sample RD-65, 2000W CO_2,1500mm/min laser (b) sample YRD-66, 2000W Nd:YAG 1500mm/min

Using our data obtained by from the CO_2 laser for 2000W power, the effect of speed is shown for different mass flows (Figure 5.2). From Equation 4.4 and sample RD-64, for the CO_2 laser at 2000W power with argon shielding gas (see Appendix C), the MZ depth for 1500 mm/min is about 1.6 time greater than the MZ depth for 3000mm/min scanning speed. In practice, as shown in Figure 5.2, the average for the MZ depth of 1500 mm/min is 0.42 mm and for 3000 mm/min is 0.27 mm resulting in a 1.55 ratio, which is comparable with theoretical results. To further examine the speed effect, the results from RD-63[1] argon gas shielding experiment is compared with theoretical values shown in Figure 5.3 and it has a very good agreement with Equation 4.4 up to and around 2500 mm/min scan speed (see Appendix C for RD-63 data).

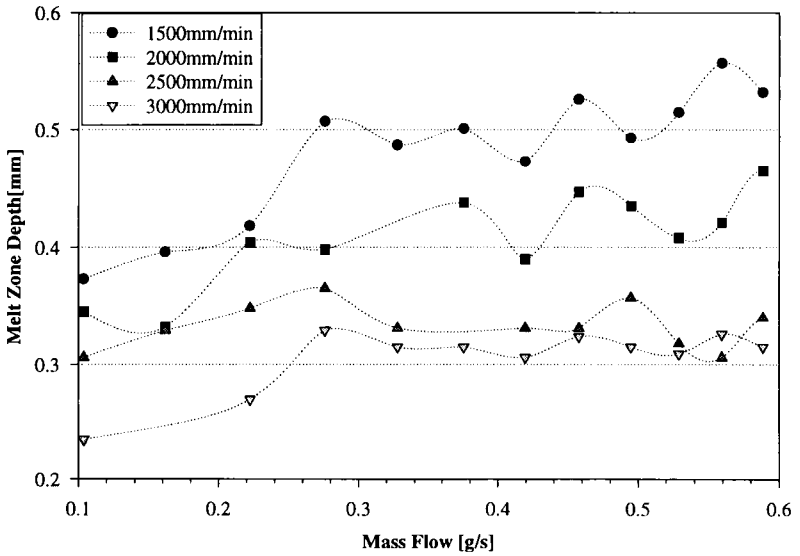

Figure 5.2 Speed effect, sample RD-64 argon shielding gas, 2000W CO_2 laser.

[1]- RD-63 and 64 experiments were specifically tailored to evaluate the speed effect.

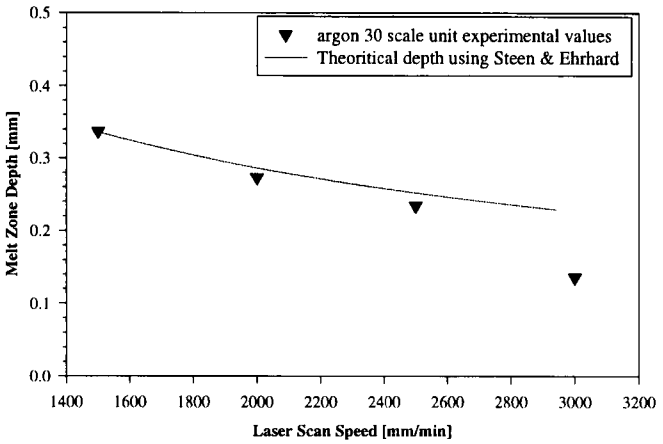

Figure 5.3 Scan speed effect on a constant mass flow, sample RD-63 argon shielding gas, 2000W CO_2 laser.

5.3 Effect of Inert Shielding Gases (He, N_2 and Ar)

In order to create a scale on which all of the mass flows can easily be compared, the melt depth data was subjected to linear regression of 1st order. These regression lines then were stretched to intersect the axis in order to predict the behavior of the mass flow at higher and lower values (see Appendix D the data regression results).

Using the regression method, the interpretation of data of all the shielding gases over the entire range of mass flow is much easier. Considering Ar, N_2 and He as inert gases and O_2, air and CO_2 as reactive gases the melt zone depth for the range of mass flows can be predicted (assuming the regression of our data hold for the entire range of mass flow). These results are shown in Figure 5.4 for the CO_2 laser.

According to previous research[24], the weld pool shape resulting from the use of different inert gases varied with ease of ionization of the gas. Helium, with the highest ionization energy (24.587 eV)[25], should have a small weld pool while argon, with 15.759eV ionization energy should have a wider and deeper melt pool than that of helium. This contradicts other research by Abbot-Albright[10], which says that helium produces significantly more penetration than argon in penetration welding.

In our experimental data (Figure 5.4) helium has a smaller melt pool than Ar and N_2 at lower mass flow. The slightly lower ionization of N_2 (15.580eV) over Ar should not yield much difference in melt pool size and this is the case for our data. For helium, at low mass flow, the ionization assumption seems to be true since helium has a smaller MZ size compared to that of Ar and N_2. At higher mass flows however (mass flow > 0.1 gr/sec), helium surpasses the MZ size of nitrogen and the extrapolation indicates it will also surpass that of argon.

On the other hand, helium used with the 2000W Nd:YAG laser and 1500mm/min scanning speed has a significantly greater MZ area than both argon and nitrogen at all the mass flows rates (Figure 5.5). Thus, it seems that the effectiveness of He shielding gas is most pronounced when using the Nd:YAG laser. For argon and nitrogen, however, the MZ is almost the same as the ionization effect would have predicted.

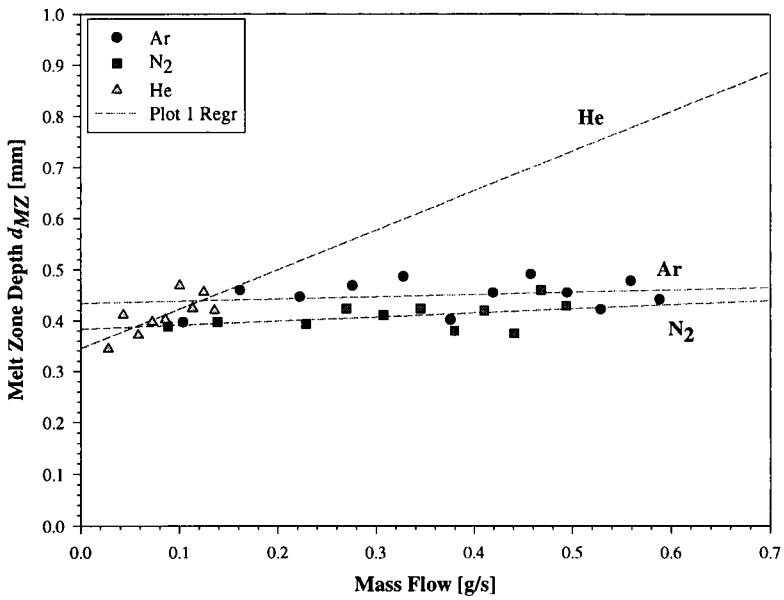

Figure 5.4 Melt zone depth for inert gases, sample RD-66, 2000W CO_2 laser, 1500mm/min.

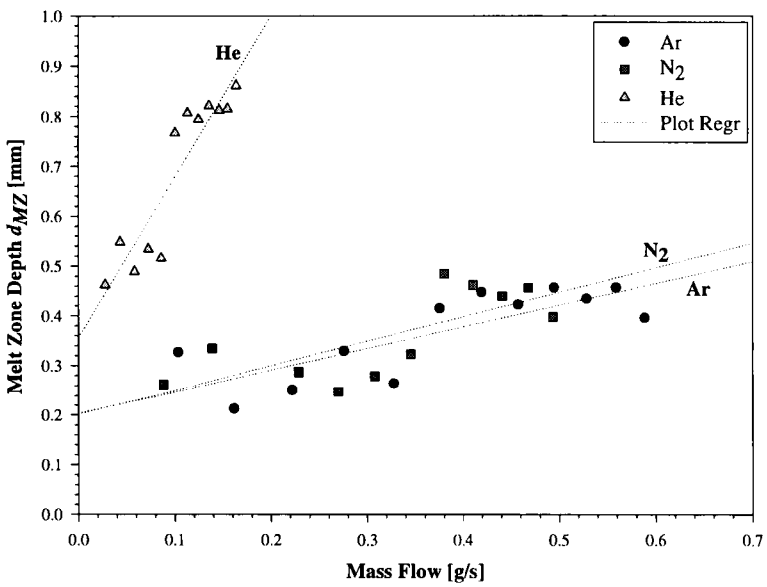

Figure 5.5 Melt zone depth for inert gases, sample YRD-66, 2000W Nd:YAG laser, 1500mm/min.

5.4 Effect of Sulfur in the Argon Shielding Gas

As seen on Figure 5.6, using an Ar + 701ppm of SO_2 during CO_2 processing does not alter the melt area. If sulfur is added to the melt it could reduce the surface tension of the melt and therefore by increasing the convection effect it could increase the melt area[22]. But since convection is not very effective at shallow melt depths, the SO_2 additive cannot increase the melt depth effectively.

On the positive side, the sulfur (in MnS form) could improve the machinability of the melt surface, therefore, helping the ease of post processing of the workpiece. The draw back of sulfur additive on the other hand, is that if the high sulfur content is in the composition melt, is that the sulfur could impair the ductility of steel[22].

In our experiment using the Nd:YAG laser the effectiveness of sulfur additive in the argon gas to increase the melt pool was only observed at lower mass flows (Figure 5.7). At higher mass flow (greater than 0.3 g/s) the melt pool size for Ar grows almost parallel with sulfur addition.

5.5 Effect of Reactive Gases (Oxygen, Air and CO_2)

Unlike the inert gases, gas types such as Air, O_2 and CO_2 react vigorously with the substrate. It is not easy to determine the chemical reaction which these gases have with the melt pool since the quantitative and qualitative analysis of oxygen and carbon in the

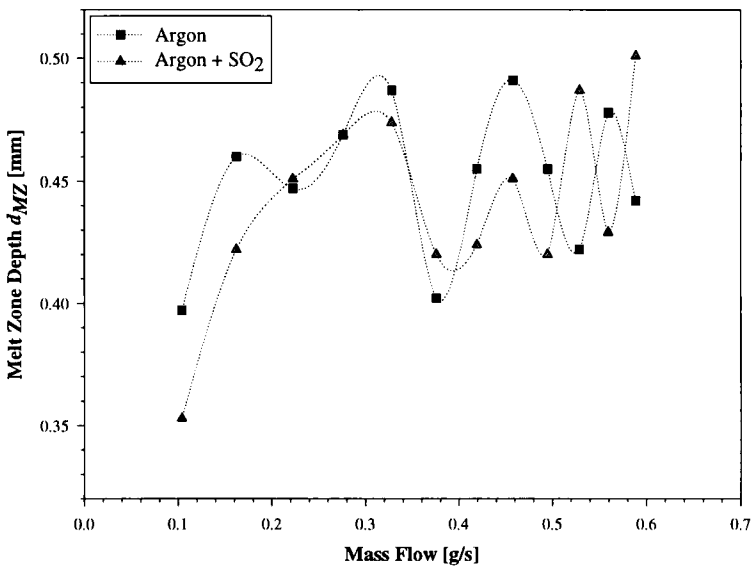

Figure 5.6 Effect of sulfur on the depth of MZ, RD-66 2000W CO_2 laser at 1500mm/min scan speed.

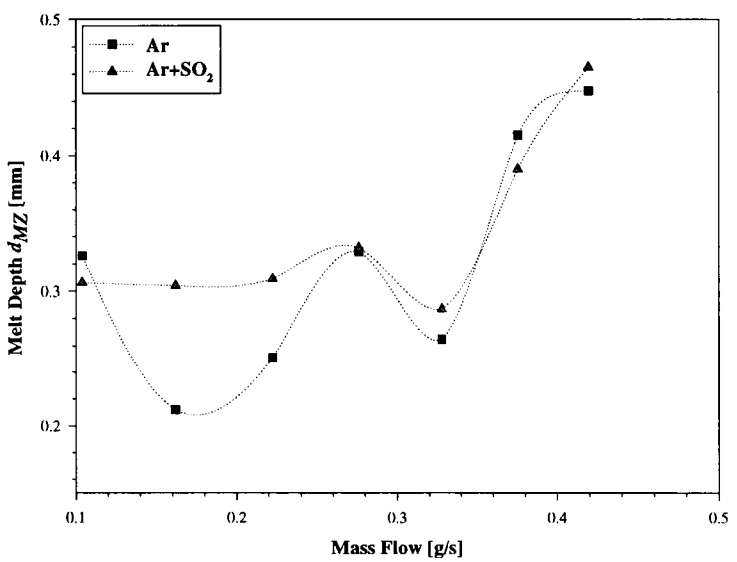

Figure 5.7 Effect of sulfur on the depth of MZ, YRD-66 2000W Nd:YAG laser at 1500mm/min scan speed.

melt zone needs special instrumentation. The oxidation of the MZ is an important factor in some industrial applications and therefore the oxidation content of the modified surface must be kept at reasonable levels. But as far as creating a bigger and deeper melt pool these gases are quite successful[11].

The benefits of using CO_2 as a shielding gas for mild steel is that it provides almost the same amount of MZ size but for a better price value (see Figure 5.8 for CO_2 and Figure 5.5 for He). The major draw back of carbon dioxide, and other reactive gases introduced, is that it may cause porosity in the melt zone (Figure 5.9). The high energy laser causes dissociation of $CO_2 \rightarrow CO + O$, with CO being virtually insoluble in the melt while oxygen has a high solubility. For future considerations, the addition of ferrosilicon power to the weld pool has been shown to effectively control the formation of trapped bubbles (CO) in the MZ and result in a porosity free melt pool[10].

Comparing to He, as seen in Figure 5.8, all reactive gases yield much lower melt zone depth. But to reach the same level of melt depth achieved by other reactive gases, He has to be supplied at higher mass flow than is possible with our current gas supply pressure. If the porosity problem is removed, as discussed before, then CO_2 is better alternative to get high melt depth with our current gas flow pressure.

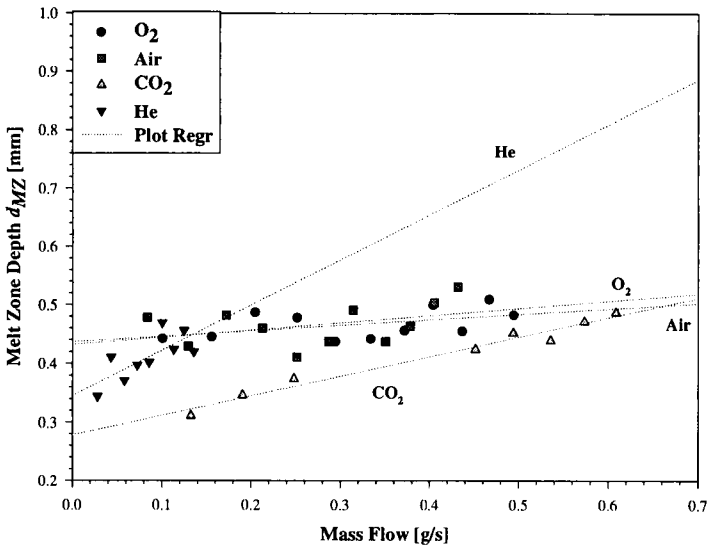

(a)

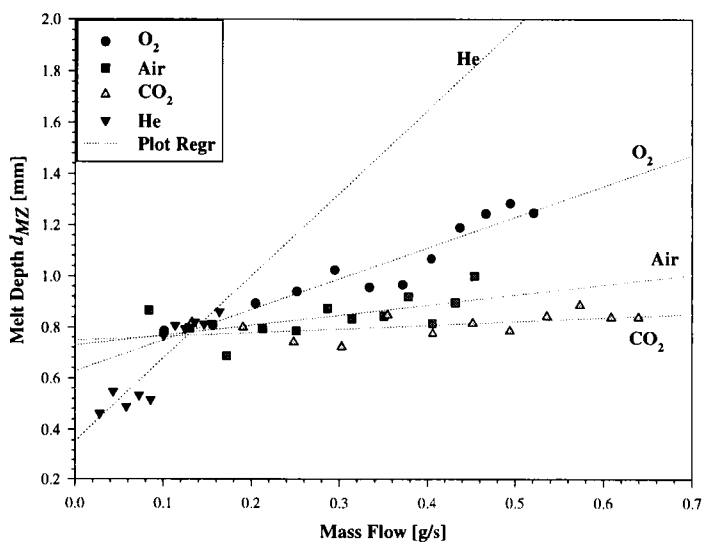

(b)

Figure 5.8 Effect of reactive gases on the melt pool (a) RD-66, 2000W CO_2 laser, (b) YRD-66, 2000W Nd:YAG, 1500mm/min.

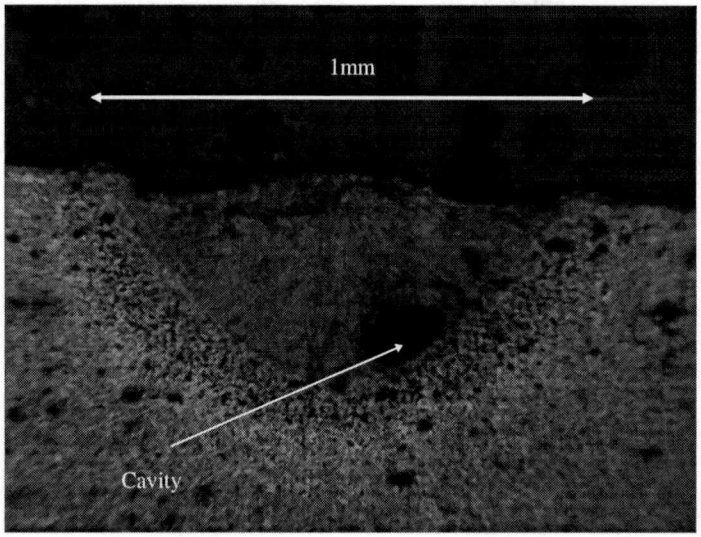

Figure 5.9 Porosity caused by CO_2 shielding gas.

Porosity is also frequently observed in the air an oxygen treated samples. But despite the high oxidation level and porosity introduced in the MZ and the melt pool size is considerably larger than the inert gas treated samples. If the oxidation levels are not required to be low, air and oxygen are good candidates for deep penetrating or cutting applications.

5.6 Modified Steen-Ehrhard model

Using the regression value for the shielding gas effect, we can modify Equation 4.4 to take the effect of variable mass flow of shielding gases into account. It must be noted that the analyzed sample for this first order linear regression calculations, YRD-66

and RD-66, are taken at constant power and speed. Changing these parameters may alter the out come of this modification.

$$(5.1) \quad d_{MZ} = \left(\beta_0 + \beta_1 \cdot \dot{M}\right)\left[\sqrt{\frac{4}{\pi \cdot \frac{2vr_0}{k}}} - \left(\frac{T_m}{T\infty} - 1\right) \cdot \frac{1}{\frac{I \cdot A \cdot 2r_o}{KT_\infty}}\right] \cdot 2r_0$$

where $\dot{M}$ is the mass flow in Kg/sec and β_0 modified regression parameters in m, and β_1 is the modified gas constant for each shielding gas in s/Kg.

The empirical β values, modified from $\beta(0)$ and $\beta(1)$ are shown in Table D.2 in the Appendix D. The $\beta(0)$ and $\beta(1)$ are directly calculated from the regression data as seen in the regression plot in Appendix D. After dividing the $\beta(0)$ and $\beta(1)$ values by the MZ depth we can find β_0 and β_1.

5.7 Plasma Analysis

As discussed in Chapter 1, the effect of mass flow on plasma formation has not been yet established. Furthermore, some contradictions as to the effect of ionization potential, have been reported. To observe the effect of plasma size on changes in the melt pool size we used the technique outlined in Chapter 2.

For each track 6 different measurements from a total of more than 30 frames/track were recorded. Since the plasma was unstable it was difficult to measure accurately. From our gathered data on average of plasma size on the sample no conclusive analysis could be drawn (Figure 5.11). These measurements are not indicative of temperature, electron or ion density of plasma. But generally the reactive gases such as, oxygen, air and carbon dioxide generate larger and more explosive plasma (Figure 5.11).

Although from Figure 5.12, the plasma size and melt zone depth size do not change simultaneously, they do each grow as the mass flow increases. This suggests that the plasma size and melt depth may have some correlation. Actually comparing the measured plasma cross section area vs. the melt zone depth as seen in Figure 5.13 gives a correlation pattern for $r_*^2 = 0.45$. For $r_*^2 = 1$ we have a perfect 1^{st} order linear regression and for $r_*^2 = 0$ the data is completely scattered with no correlation (see Appendix E) for all the RD-66 samples).

This correlation suggests that some of the heat re-radiated back to the melt zone by a larger plasma may correspond to a larger heat source or a higher temperature plasma. But for the rest of our plasma data the correlation values are very small, suggesting that this correlation may only be an accident (see Appendix E).

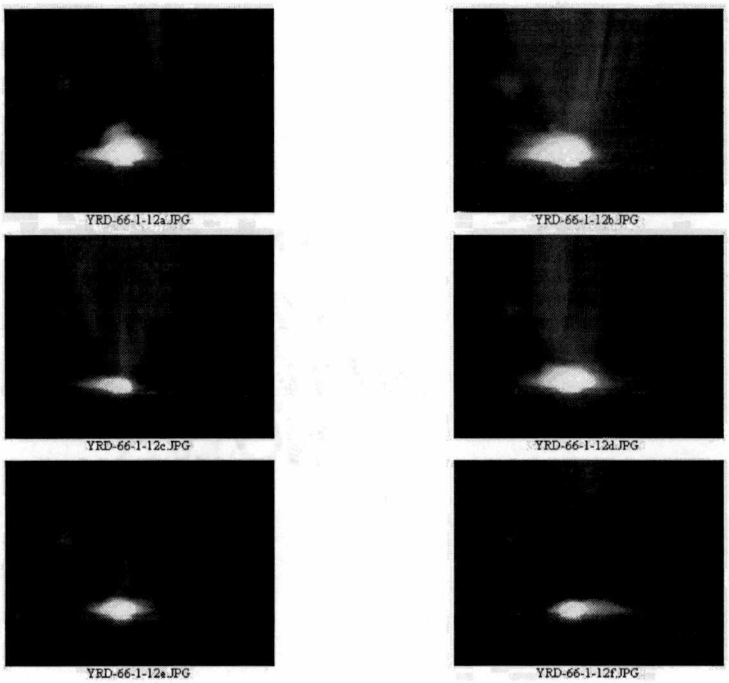

Figure 5.10 Typical plasma fluctuations on the melt pool.

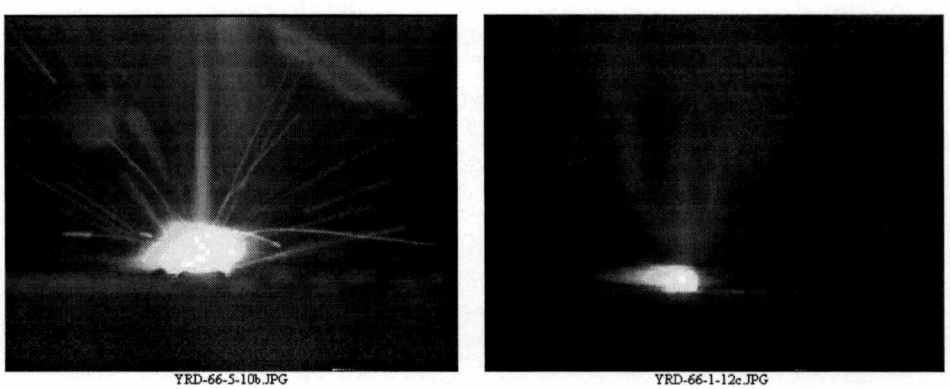

Figure 5.11 The plasma form depends on the type of shielding gas, at left the oxygen generates brighter glow and sparks than argon shielding gas.

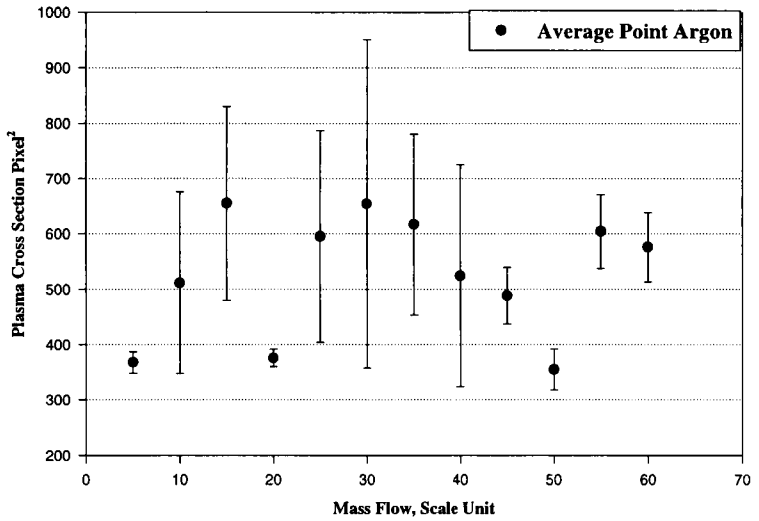

(a)

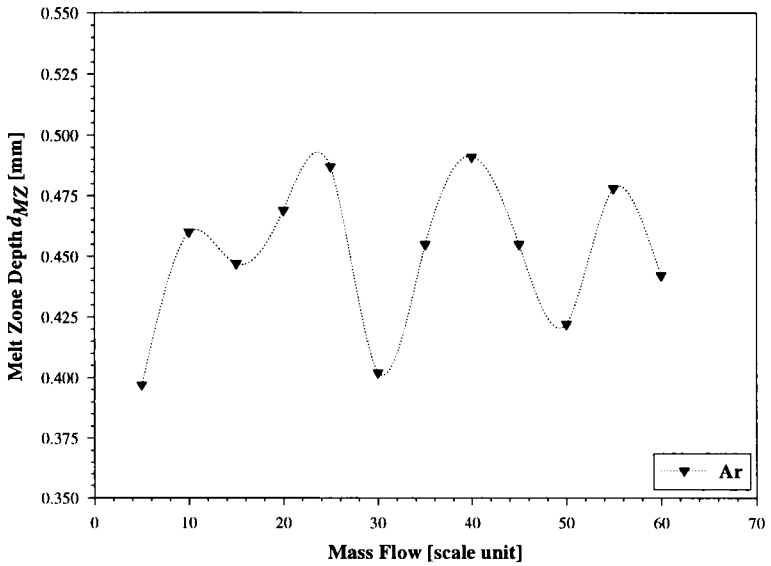

(b)

Figure 5.12 Amplitude change of plasma size vs. Melt zone depth, RD-66-1 argon gas. The plasma size fluctuation (a) seems to have no correspondence to the size fluctuation of MZ depth (b).

Summary

- Melt zone depth increases with the gas flow.
- Increase in the speed reduces the melt zone depth.
- Plasma enhanced coupling is frequently observed.
- For helium shielding gas, plasma enhanced coupling has some correlation with the size of the plasma formed, but for the rest of the shielding gas the correlation values are very low.
- Plasma dominates the heat transfer mechanism to the melt zone, since the laser radiation by itself could not create such melt depths.
- Shielding gas type is an important factor in shape and size of plasma.
- Size of plasma may have some correlation with melt depth size in each gas.
- Helium with its highest ionization energy, creates the highest value for melt depth.
- CO_2 gas does not deliver performance close to He as stated in previous experiments.
- CO_2 shielding gas creates porosity in the melt zone.
- Oxygen and air despite the good penetration depth are not good candidates for material processing, due to the high oxidation and porosity level observed in the application.
- Sulfur addition may have to be increased to see a substantial increase in the melt zone depth in all mass flows.

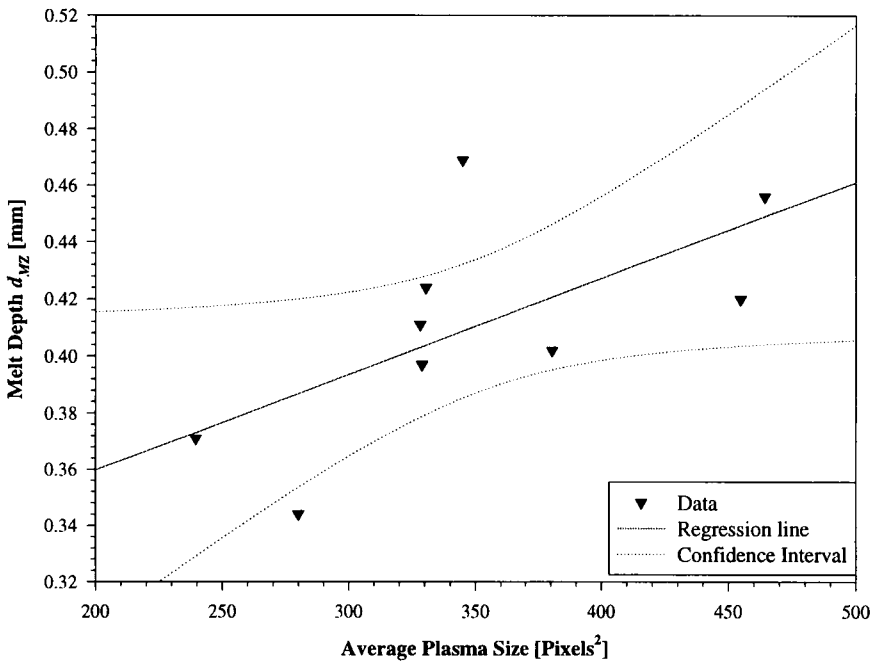

Figure 5.13 Correlation of melt depth with plasma size.

BIBLIOGRAPHY

1. *Guide to laser material processing* by Sidney S. Charschan, Laser Institute of America.
2. *Handbook of Chemistry and Physics*. David R. Lide 77th edition
3. *CRS handbook of thermophysical and thermomechanical dat,* David Lide and H. V. Kehiaian.
4. *Laser Processing and Analysis of Materials*, by W.W. Duley, Plenum.
5. *Laser-Beam Interactions with Materials*, M. V. Allmen & A. Blatter, Springer Pub.
6. ROFIN-SINAR RS-3000 CO_2 laser operational manual.
7. Hobart HLP-3000 Nd:YAG laser operational manual.
8. *CLEO LEAP Conference*, C. B. Roundy and K. Kirkham, June 6-1996, Spiricon Inc. Home Page.
9. *Recent Progress in the Laser Surface Treatment*, W.Bloehs, B. Grunenwald, F. Dausinger and H. Hugel, Laser Institute of America 8-1996.
10. *CO_2 Shielding Gas Effects in Laser Welding Mild Steel*, D.H. Abbott, C.E. Albright, Journal of Laser Applications 6-1994.
11. *The Influence of Shielding Gas Type in High-Power Nd:YAG Laser Welding*, C. Bagger, G. Borden, E. Beske and F. Olsen, JOM-6, Helsinngor, Denmark, 5-7 April,1993

12. *Temperature-Dependent Absorptivity and Cutting Capability of CO2, Nd:YAG and Chemical Oxygen-iodine Lasers*, J. Xie, A. Kar, J.A. Rothenflue and W.P. Latham, Journal of Laser Applications (1997)

13. *The Theory and Application of Laser Chemical Vapor Deposition*, Mazumder, J. and Kar, Plenum Press

14. W.W. Duley, D.J. Semple, J.-P. Mrencyan M. Garvel, Opt. Laser Technol. 11, 281 (1979)

15. *Guide to laser Material Processing*, edited by Sidney S. Charschan, Laser Institute of America.

16. *CRC Handbook of Thermophysical and Thermochemical Data*, D. R. Lide, H.V. Kehiaian.

17. *Metals Handbook* 9th edition, vol. 1, American Society of Metals.

18. *Conduction of Heat in Solids*, H.S. Carslaw and J.C. Jeager, Oxford Press,1959

19. *The theory of Moving Source of Heat and Its Application to Metal Treatments*, D. Rosenthal, ASME Trans., 1946 p.849

20. *Depth of Melt-Pool and Heat-Affected Zone in Laser Surface Treatment*, P.H. Steen, P. Ehrhared, and A. Schussler, Met. And Mat. Trans A, Vol. 25A, Feb 1994, p427

21. *Conduction of Heat in Solids*, H.S. Carslaw and J.C. Jeager, 2nd ed., Oxford press

22. *Steels: Metallurgy and Applications*, D.T. Llewellyn, B & H pub. Ltd.

23. *A fundamental Plasma Based Model for Energy Transfer in Laser Material Processing*, B.R. Finke, P.D. Kapadia, J.M. Dowden, J. Phys. D:Appl. Phys., 23, 1990, p.643

24. *The Laser Welding of Thin Metal Sheets*, R. Ducharme, K. Williams, P Kapadia, J. Dowens, B. Steen and M. Glwaki, J. Phys. D: Appl. Phys. 27(1994) 1619-1627

25. *Handbook of Physical Properties of Liquids and Gases,* Begell House Pub.

26. *Heat Treating and Melting with Scanning Laser or electron beam*, H.E. Cline and T.R Anthony, Journal Appl. Phys. , vol 48, No 9, Sept 1977

27. *Modern Optics*, Robert Guenther, J Wiley Pub.

28. Arata, Y. and Miyamoto, I. Trans. Japn. Weld Soc. 3, 152-162,1972

29. *Handbook of Chemistry and Physics*. David R. Lide 77th edition

APPENDICES

APPENDIX A

Table A.1 Physical characteristics of shielding gases at room temperature[29].

	Air	Ar	Co2	He	N2	O2
Density g/L:	1.161	1.753	1.931	0.176	1.229	1.404
Ionization Potential eV:		15.759	13.773	24.587	15.5808	12.071
Heat Capacity J/gK	1.007	0.520	0.845	5.193	1.040	0.918
ıermal conductivity W/mK		17.9	16.8	156.7	26.0	26.3

Table A.2 Scale unit to liter per minute mass flow conversion

	Air	Ar	Co2	He	N2	O2
Scale	**Flow**	**Flow**	**Flow**	**Flow**	**Flow**	**Flow**
Reading	**L/min**	**L/min**	**L/min**	**L/min**	**L/min**	**L/min**
5	4.323	3.556	4.125	9.523	4.31	4.321
10	6.681	5.543	5.925	14.745	6.772	6.681
15	8.882	7.617	7.712	19.861	9.118	8.759
20	10.995	9.453	9.407	24.75	11.175	10.779
25	12.987	11.225	11.024	29.276	13.178	12.602
30	14.821	12.854	12.618	34.229	15.026	14.276
35	16.252	14.357	14.039	38.7	16.847	15.899
40	18.109	15.673	15.349	42.59	18.553	17.294
45	19.541	16.939	16.656	46.267	20.046	18.683
50	20.963	18.106	17.824	49.889	21.525	19.964
55	22.317	19.15	18.912	52.813	22.856	21.137
60	23.452	20.147	19.876	55.876	24.105	22.271
65	24.68	21.116	20.798	58.472	25.311	23.322

Table A.3 Scale unit to gram per second mass flow conversion.

	Air	Ar	Co2	He	N2	O2
Scale	Mass	Mass	Mass	Mass	Mass	Mass
Reading	g/s	g/s	g/s	g/s	g/s	g/s
5	0.08365	0.10389	0.13276	0.02793	0.08828	0.10111
10	0.12928	0.16195	0.19069	0.04325	0.13871	0.15634
15	0.17187	0.22254	0.2482	0.05826	0.18677	0.20496
20	0.21275	0.27619	0.30275	0.0726	0.2289	0.25223
25	0.2513	0.32796	0.35479	0.08588	0.26993	0.29489
30	0.28679	0.37555	0.40609	0.10041	0.30778	0.33406
35	0.31448	0.41946	0.45182	0.11352	0.34508	0.37204
40	0.35041	0.45791	0.49398	0.12493	0.38003	0.40468
45	0.37812	0.4949	0.53605	0.13572	0.41061	0.43718
50	0.40563	0.529	0.57364	0.14634	0.4409	0.46716
55	0.43183	0.5595	0.60865	0.15492	0.46817	0.49461
60	0.4538	0.58863	0.63968	0.1639	0.49375	0.52114
65	0.47756	0.61694	0.66935	0.17152	0.51845	0.54573

APPENDIX B

PHYSICAL PROPERTIES OF IRON

The following gives us the thermal conductivity as the function of temperature of iron, Fe, in the different phases of material, K is the thermal conductivity in W/mK, T is the temperature from 273 to 873 Kelvin[16].

$$K = A1 + A2(T) + A3(T)^2 + A4(T)^3 + A5(T)^4$$

Where:

A1 := 197.749
A2 := - 0.822405
A3 := 2.0816·10^-3
A4 := - 2.5220·10^-6
A5 := 1.1295·10^-9

Table B.1 Physical characteristics of iron[29].

Density:	7870	Kg/m^3
Specific Heat:	660	J/KgK
Average thermal conductivity:	24	W/mC
Diffusivity:	0.000004621	m^2/sec
Ionization potential in gas phase:	7.9024	eV
Melting Temperature:	1808	K
Vaporization Temperature:	3273	K

APPENDIX C

Table C.1 YRD-66 Data Series

Table C.1a

Date: 10-8-96	Stand off:	10 mm	Speed:	1500 mm/min	Power:	2000 watts	
sample/track	Ar	Melted Zone	width	Depth	HAZ	width	Depth
YRD-66-1A	scale unit	area mm^2	mm	mm	area mm^2	mm	mm
1	5	0.242	1.136	0.326	0.633	1.615	0.565
2	10	0.211	1.231	0.212	0.583	1.749	0.490
3	15	0.219	1.201	0.251	0.626	1.788	0.501
4	20	0.277	1.226	0.329	0.638	1.672	0.521
5	25	0.247	1.206	0.265	0.680	1.693	0.529
6	30	0.299	0.964	0.415	0.641	1.496	0.621
7	35	0.302	0.950	0.448	0.601	1.432	0.618
8	40	0.302	0.980	0.423	0.686	1.493	0.657
9	45	0.322	0.900	0.457	0.649	1.485	0.657
10	50	0.328	0.953	0.435	0.636	1.490	0.635
11	55	0.326	0.953	0.457	0.660	1.482	0.621
12	60	0.282	0.966	0.396	0.684	1.479	0.616
YRD-66-2A	Ar+SO2						
1	5	0.294	1.201	0.306	0.520	1.498	0.479
2	10	0.300	1.242	0.304	0.507	1.504	0.521
3	15	0.301	1.295	0.309	0.602	1.533	0.515
4	20	0.312	1.318	0.332	0.590	1.516	0.524
5	25	0.249	1.145	0.287	0.566	1.485	0.485
6	30	0.335	1.134	0.390	0.646	1.513	0.590
7	35	0.300	0.972	0.465	0.640	1.488	0.646
8	40	0.290	0.855	0.454	0.679	1.386	0.638
9	45	0.320	0.953	0.457	0.643	1.483	0.624
10	50	0.329	0.969	0.460	0.635	1.474	0.613
11	55	0.315	0.914	0.432	0.581	1.451	0.582
12	60	0.321	1.117	0.405	0.621	1.485	0.663

Table C.1b

Date: 10-8-96	Stand off:	10 mm	Speed:	1500 mm/min	Power:	2000 watts	
sample/track	Nitrogen	Melted Zone	width	Depth	HAZ	width	Depth
YRD-66-3A	scale unit	area mm^2	mm	mm	area mm^2	mm	mm
1	5	0.211	1.159	0.262	0.495	1.515	0.476
2	10	0.252	1.156	0.334	0.545	1.482	0.501
3	15	0.264	1.220	0.287	0.545	1.529	0.493
4	20	0.257	1.167	0.248	0.521	1.521	0.474
5	25	0.250	1.226	0.279	0.603	1.669	0.485
6	30	0.231	1.067	0.323	0.576	1.496	0.565
7	35	0.321	1.045	0.485	0.660	1.492	0.674
8	40	0.269	1.022	0.462	0.618	1.485	0.638
9	45	0.332	0.841	0.440	0.639	1.479	0.646
10	50	0.284	0.928	0.457	0.604	1.493	0.630
11	55	0.276	1.014	0.398	0.557	1.432	0.613
12	60	0.273	0.936	0.465	0.601	1.176	0.624
YRD-66-4A	Helium						
1	5	0.695		0.462			
2	10	0.652		0.548			
3	15	0.625		0.489			
4	20	0.762		0.534			
5	25	0.644		0.516			
6	30	0.766		0.767			
7	35	0.872		0.807			
8	40	0.887		0.794			
9	45	0.918		0.821			
10	50	0.869		0.812			
11	55	0.969		0.815			
12	60	0.972		0.861			

Table C.1c

Date: 10-8-96	Stand off:	10 mm	Speed:	1500 mm/min	Power:	2000 watts	
sample/track	Oxygen	Melted Zone	width	Depth	HAZ	width	Depth
YRD-66-5A	scale unit	area mm^2	mm	mm	area mm^2	mm	mm
1	5	1.022		0.785			
2	10	1.105		0.807			
3	15	1.339		0.892			
4	20	1.370		0.939			
5	25	1.385		1.023			
6	30	1.462		0.955			
7	35	1.469		0.966			
8	40	1.433		1.067			
9	45	1.743		1.189			
10	50	1.744		1.244			
11	55	1.625		1.284			
12	60	1.983		1.247			
YRD-66-6A	Air						
1	5	0.924		0.866			
2	10	0.919		0.796			
3	15	0.821		0.686			
4	20	0.937		0.794			
5	25	0.966		0.785			
6	30	1.008		0.874			
7	35	0.966		0.834			
8	40	1.011		0.844			
9	45	1.090		0.919			
10	50	1.160		0.816			
11	55	1.246		0.897			
12	60	1.194		1.000			

Table C.1d

Date: 10-8-96	Stand off:	10 mm	Speed:	1500 mm/min	Power:	2000 watts	
sample/track	CO2	Melted Zone	width	Depth	HAZ	width	Depth
YRD-66-7A	scale unit	area mm^2	mm	mm	area mm^2	mm	mm
1	5	0.950		0.818			
2	10	0.899		0.799			
3	15	0.940		0.740			
4	20	0.827		0.722			
5	25	0.985		0.848			
6	30	1.036		0.776			
7	35	1.044		0.816			
8	40	1.012		0.785			
9	45	1.129		0.843			
10	50	1.026		0.887			
11	55	1.162		0.839			
12	60	1.105		0.839			

Table C.2 RD-66 Data Series

Table C.2a

Date: 10-8-96	Stand off:		10 mm	Speed:	0.025	Power:	2000 watts	
sample/track	Ar	Flow	Melted Zone	width	Depth	HAZ	width	Depth
RD-66-1A	scale unit	Lit/min	area mm^2	mm	mm	area mm^2	mm	mm
1	5	3.556	0.295	1.059	0.397	1.013	2.094	0.679
2	10	5.543	0.386	1.077	0.460	0.965	2.028	0.697
3	15	7.617	0.288	0.871	0.447	0.919	2.033	0.714
4	20	9.453	0.307	1.037	0.469	1.006	2.006	0.741
5	25	11.225	0.362	0.956	0.487	0.867	1.960	0.687
6	30	12.854	0.312	0.908	0.402	0.859	1.885	0.625
7	35	14.357	0.303	0.956	0.455	0.815	1.825	0.657
8	40	15.673	0.364	0.962	0.491	0.855	1.854	0.674
9	45	16.939	0.328	1.032	0.455	0.863	1.898	0.634
10	50	18.106	0.324	0.929	0.422	0.787	1.827	0.643
11	55	19.150	0.429	1.170	0.478	0.817	1.920	0.674
12	60	20.147	0.369	1.022	0.442	0.899	1.920	0.656
RD-66-2A	Ar+SO2							
1	5	3.556	0.204	0.835	0.353	0.679	1.782	0.571
2	10	5.543	0.286	0.867	0.422	0.758	1.809	0.616
3	15	7.617	0.307	0.929	0.451	0.731	1.790	0.629
4	20	9.453	0.308	0.974	0.469	0.791	1.871	0.585
5	25	11.225	0.333	1.000	0.474	0.797	1.898	0.67
6	30	12.854	0.320	1.027	0.420	0.982	1.943	0.683
7	35	14.357	0.336	0.902	0.424	0.817	1.755	0.629
8	40	15.673	0.367	1.023	0.451	1.060	2.005	0.741
9	45	16.939	0.303	0.987	0.420	0.913	1.934	0.71
10	50	18.106	0.362	1.053	0.487	0.928	1.929	0.723
11	55	19.150	0.346	0.955	0.429	0.961	2.028	0.696
12	60	20.147	0.353	1.055	0.501	0.997	2.01	0.719

Table C.2b

Date: 10-8-96	Stand off:		10 mm	Speed:	0.025	Power:	2000 watts	
sample/track	Nitrogen	Flow	Melted Zone	width	Depth	HAZ	width	Depth
RD-66-3A	scale unit	Lit/min	area mm^2	mm	mm	area mm^2	mm	mm
1	5	4.310	0.273	0.696	0.388	0.818	1.759	0.607
2	10	6.772	0.284	1.076	0.397	0.794	1.973	0.616
3	15	9.118						
4	20	11.175	0.290	1.013	0.393	0.851	1.915	0.625
5	25	13.178	0.303	1.062	0.424	0.938	1.991	0.692
6	30	15.026	0.281	1.058	0.411	0.800	1.879	0.652
7	35	16.847	0.314	0.978	0.424	0.801	1.997	0.652
8	40	18.553	0.292	0.978	0.380	0.897	1.915	0.625
9	45	20.046	0.302	0.982	0.420	0.918	2.018	0.634
10	50	21.525	0.294	1.067	0.375	0.923	2.049	0.67
11	55	22.856	0.328	1.027	0.460	1.063	2.085	0.692
12	60	24.105	0.319	1.067	0.429	0.969	2.093	0.714
RD-66-4A	Helium							
1	5	9.523	0.253	1.019	0.344	0.690	1.997	0.58
2	10	14.745	0.263	1.063	0.411	0.736	1.998	0.629
3	15	19.861	0.274	1.090	0.371	0.790	1.997	0.594
4	20	24.750	0.300	1.081	0.397	0.778	1.997	0.62
5	25	29.276	0.264	0.951	0.402	0.833	1.930	0.656
6	30	34.229	0.329	0.929	0.469	0.796	1.996	0.67
7	35	38.700	0.334	1.081	0.424	0.769	1.925	0.638
8	40	42.590	0.300	1.059	0.456	0.829	1.911	0.611
9	45	46.267	0.354	1.206	0.420	0.755	1.992	0.607
10	50	49.889						
11	55	52.813						
12	60	55.876						

Table C.2c

Date: 10-8-96	Stand off:		10 mm	Speed:	0.025	Power:	2000 watts	
sample/track	Oxygen	Flow	Melted Zone	width	Depth	HAZ	width	Depth
RD-66-5A	scale unit	Lit/min	area mm^2	mm	mm	area mm^2	mm	mm
1	5	4.321	0.319	1.112	0.442	1.013	1.995	0.728
2	10	6.681	0.335	1.013	0.445	1.023	1.982	0.647
3	15	8.759	0.330	0.902	0.487	1.192	2.005	0.768
4	20	10.779	0.340	0.978	0.478	1.075	2.129	0.777
5	25	12.602	0.328	1.018	0.437	1.123	2.160	0.746
6	30	14.276	0.322	1.022	0.442	1.043	2.080	0.701
7	35	15.899	0.410	1.175	0.456	1.063	2.087	0.701
8	40	17.294	0.401	1.139	0.500	1.069	2.105	0.709
9	45	18.683	0.384	1.100	0.455	1.058	2.127	0.742
10	50	19.964	0.390	1.140	0.509	1.149	2.230	0.768
11	55	21.137	0.384	1.090	0.482	1.174	2.408	0.764
12	60	22.271						
RD-66-6A	Air							
1	5	4.323	0.306	1.076	0.478	1.031	2.116	0.7
2	10	6.681	0.344	1.112	0.429	0.885	2.071	0.652
3	15	8.882	0.379	1.223	0.482	0.998	2.178	0.713
4	20	10.995	0.361	1.094	0.460	1.098	2.063	0.719
5	25	12.987	0.286	1.089	0.411	0.866	2.045	0.647
6	30	14.821	0.336	0.991	0.437	0.940	2.036	0.737
7	35	16.252	0.338	1.040	0.491	0.873	1.987	0.661
8	40	18.109	0.342	1.125	0.437	0.919	2.037	0.706
9	45	19.541	0.345	0.974	0.464	0.918	1.978	0.67
10	50	20.963	0.365	1.036	0.504	0.909	1.965	0.687
11	55	22.317	0.410	1.116	0.531	0.997	1.960	0.706
12	60	23.452						

Table C.2d

Date: 10-8-96	Stand off:		10 mm	Speed:	0.025	Power:	2000 watts	
sample/track	CO2	Flow	Melted Zone	width	Depth	HAZ	width	Depth
RD-66-7A	scale unit	Lit/min	area mm^2	mm	mm	area mm^2	mm	mm
1	5	4.125	0.299	1.100	0.311	0.753	1.867	0.62
2	10	5.925	0.319	1.210	0.346	0.829	1.849	0.634
3	15	7.712	0.340	1.108	0.374	0.837	1.921	0.634
4	20	9.407						
5	25	11.024						
6	30	12.618						
7	35	14.039	0.348	1.005	0.424	0.847	1.801	0.603
8	40	15.349	0.316	1.054	0.452	0.893	2.005	0.648
9	45	16.656	0.283	1.027	0.439	0.797	1.924	0.569
10	50	17.824	0.312	1.099	0.471	0.806	2.032	0.625
11	55	18.912	0.483	0.951	0.487	0.733	1.902	0.59
12	60	19.876						

Table C.3 RD-65 Data Series

Table C.3a

Date: 7-9-96	Power:	2000		Single Image						
sample/track	speed	Mass Flow	Ar	stand off	Melted Zone	width	Depth	HEZ	width	Depth
RD-65-1 A	mm/min	scale unit	l/min	mm	mm^2	mm	mm	mm^2	mm	mm
1	1500	5	3.556	10	0.076	0.618	0.178	0.325	1.488	0.354
2	1500	20	9.453	10	0.104	0.735	0.24	0.419	1.521	0.401
3	1500	30	12.854	10	0.127	0.866	0.237	0.408	1.532	0.418
4	1500	40	15.673	10	0.131	0.78	0.242	0.451	1.666	0.429
5	1500	50	18.106	10	0.128	0.68	0.237	0.48	1.532	0.44
6	1500	60	20.147	10	0.13	0.733	0.27	0.504	1.535	0.471
RD-65-1B										
1	2000	5	3.556	10	0.084	0.607	0.212	0.322	1.354	0.362
2	2000	20	9.453	10	0.084	0.594	0.187	0.362	1.419	0.362
3	2000	30	12.854	10	0.116	0.727	0.243	0.364	1.478	0.385
4	2000	40	15.673	10	0.1	0.753	0.189	0.414	1.683	0.382
5	2000	50	18.106	10	0.126	0.751	0.248	0.388	1.505	0.39
6	2000	60	20.147	10	0.139	0.856	0.214	0.437	1.536	0.426
RD-65-1C										
1	3000	5	3.556	10	0.034	0.484	0.092	0.221	1.275	0.238
2	3000	20	9.453	10	0.076	0.926	0.106	0.294	1.411	0.281
3	3000	30	12.854	10	0.085	0.767	0.128	0.294	1.458	0.293
4	3000	40	15.673	10	0.071	0.789	0.153	0.282	1.389	0.306
5	3000	50	18.106	10	0.067	0.792	0.142	0.295	1.424	0.287
6	3000	60	20.147	10	0.069	0.803	0.125	0.312	1.469	0.287

Table C.3b

Date: 7-9-96	Power:	2000								
sample/track	speed	Mass Flow	Ar+So2	stand off	Melted Zone	width	Depth	HEZ	width	Depth
RD-65-2 A	mm/min	scale unit	l/min	mm	mm^2	mm	mm	mm^2	mm	mm
1	1500	5	3.556	10	0.056	0.536	0.181	0.366	1.294	0.396
2	1500	20	9.453	10	0.147	0.73	0.279	0.49	1.454	0.487
3	1500	30	12.854	10	0.159	0.872	0.279	0.551	1.477	0.507
4	1500	40	15.673	10	0.197	0.951	0.365	0.577	1.507	0.544
5	1500	50	18.106	10	0.201	1.065	0.351	0.602	1.6	0.535
6	1500	60	20.147	10	0.222	1.007	0.401	0.591	1.528	0.568
RD-65-2B										
1	2000	5	3.556	10	0.127	0.618	0.256	0.449	1.409	0.46
2	2000	20	9.453	10	0.133	0.691	0.279	0.468	1.49	0.473
3	2000	30	12.854	10	0.16	0.819	0.295	0.514	1.476	0.49
4	2000	40	15.673	10	0.137	0.838	0.259	0.442	1.51	0.432
5	2000	50	18.106	10	0.137	0.791	0.292	0.448	1.6	0.451
6	2000	60	20.147	10	0.183	0.983	0.318	0.663	1.536	0.518
RD-65-2C										
1	3000	5	3.556	10	0.07	0.17	0.17	0.241	1.117	0.312
2	3000	20	9.453	10	0.054	0.151	0.151	0.298	1.324	0.298
3	3000	30	12.854	10	0.048	0.128	0.128	0.285	1.427	0.323
4	3000	40	15.673	10	0.076	0.167	0.167	0.324	1.363	0.357
5	3000	50	18.106	10	0.09	0.187	0.187	0.392	1.46	0.359
6	3000	60	20.147	10	0.081	0.203	0.203	0.411	1.502	0.365

Table C.3c

Date: 7-9-96	Power:	2000								
sample/track	speed	Mass Flow	N2	stand off	Melt Zone	width	Depth	HEZ	width	Depth
RD-65-3 A	mm/min	scale unit	l/min	mm	mm^2	mm	mm	mm^2	mm	mm
1	1500	5	4.31	10	0.088	0.639	0.212	0.346	1.42	0.382
2	1500	20	11.175	10	0.203	0.985	0.315	0.457	1.49	0.449
3	1500	30	15.026	10	0.141	0.819	0.281	0.466	1.517	0.457
4	1500	40	18.553	10	0.167	0.879	0.323	0.507	1.524	0.493
5	1500	50	21.525	10	0.203	0.888	0.323	0.526	1.535	0.482
6	1500	60	24.105	10	0.189	0.93	0.36	0.551	1.545	0.504
RD-65-3B										
1	2000	5	4.31	10	0.106	0.696	0.262	0.304	1.436	0.446
2	2000	20	11.175	10	0.114	0.733	0.265	0.389	1.433	0.424
3	2000	30	15.026	10	0.129	0.762	0.254	0.44	1.473	0.429
4	2000	40	18.553	10	0.14	0.713	0.273	0.485	1.54	0.423
5	2000	50	21.525	10	0.173	0.925	0.323	0.427	1.509	0.465
6	2000	60	24.105	10	0.136	0.708	0.232	0.39	1.451	0.382
RD-65-3C										
1	3000	5	4.31	10	0.0019	0.284	0.081	0.186	1.134	0.237
2	3000	20	11.175	10	0.076	0.58	0.178	0.253	1.271	0.293
3	3000	30	15.026	10	0.078	0.574	0.192	0.285	1.346	0.296
4	3000	40	18.553	10	0.078	0.672	0.192	0.308	1.371	0.323
5	3000	50	21.525	10	0.089	0.697	0.192	0.3	1.41	0.337
6	3000	60	24.105	10	0.101	0.674	0.217	0.324	1.458	0.362

Table C.3d

Date: 7-9-96	Power:	2000								
sample/track	speed	Mass Flow	He	stand off	Melted Zone	width	Depth	HEZ	width	Depth
RD-65-4 A	mm/min	scale unit	l/min	mm	mm^2	mm	mm	mm^2	mm	mm
1	1500	5	9.523	10	0.056	0.552	0.115	0.326	1.413	0.357
2	1500	20	24.75	10	0.111	0.633	0.254	0.498	1.64	0.471
3	1500	30	34.229	10	0.143	0.682	0.279	0.496	1.535	0.468
4	1500	40	42.59	10	0.15	0.955	0.293	0.514	1.689	0.462
5	1500	50	49.889	10	0.183	1.006	0.316	0.527	1.71	0.466
6	1500	60	55.876	10	0.169	0.965	0.315	0.517	1.795	0.466
RD-65-4B										
1	2000	5	9.523	10	0	0	0	0.251	1.253	0.269
2	2000	20	24.75	10	0.081	0.621	0.195	0.335	1.495	0.362
3	2000	30	34.229	10	0.086	0.669	0.187	0.366	1.515	0.379
4	2000	40	42.59	10	0.14	0.803	0.251	0.386	1.527	0.39
5	2000	50	49.889	10	0.118	0.825	0.245	0.42	1.543	0.418
6	2000	60	55.876	10	0.159	0.878	0.301	0.448	1.69	0.423
RD-65-4C										
1	3000	5	9.523	10	0.045	0.524	0.109	0.236	1.36	0.265
2	3000	20	24.75	10	0.074	0.552	0.209	0.287	1.444	0.312
3	3000	30	34.229	10	0.072	0.671	0.175	0.297	1.469	0.326
4	3000	40	42.59	10	0.068	0.624	0.164	0.322	1.494	0.318
5	3000	50	49.889	10	0.081	0.588	0.192	0.288	1.505	0.331
6	3000	60	55.876	10						

Table C.3e

Date: 7-9-96	Power:	2000								
sample/track	speed	Mass Flow	O2	stand off	Melted Zone	width	Depth	HEZ	width	Depth
RD-65-5A	mm/min	scale unit	l/min	mm	mm^2	mm	mm	mm^2	mm	mm
1	1500	5	4.321	10	0.266	1.359	0.364	0.661	1.714	0.516
2	1500	20	10.779	10	0.289	1.471	0.382	0.766	1.818	0.546
3	1500	30	14.276	10	0.353	1.512	0.432	0.832	1.967	0.619
4	1500	40	17.294	10	0.381	1.523	0.433	0.87	1.97	0.627
5	1500	50	19.964	10	0.408	1.538	0.429	0.958	2.004	0.66
6	1500	60	22.271	10	0.456	1.548	0.41	1.001	2.001	0.666
RD-65-5B										
1	2000	5	4.321	10	0.188	1.133	0.323	0.6	1.764	0.485
2	2000	20	10.779	10	0.235	1.377	0.301	0.608	1.884	0.46
3	2000	30	14.276	10	0.279	1.352	0.359	0.762	1.978	0.554
4	2000	40	17.294	10	0.324	1.51	0.373	0.771	1.866	0.585
5	2000	50	19.964	10	0.336	1.449	0.387	0.814	1.92	0.552
6	2000	60	22.271	10	0.321	1.529	0.376	0.814	1.858	0.585
RD-65-5C										
1	3000	5	4.321	10	0.095	1.025	0.195	0.385	1.532	0.3226
2	3000	20	10.779	10	0.145	1.192	0.204	0.448	1.599	0.376
3	3000	30	14.276	10	0.209	1.242	0.256	0.528	1.561	0.435
4	3000	40	17.294	10	0.243	1.415	0.271	0.7	1.836	0.46
5	3000	50	19.964	10	0.229	1.39	0.281	0.566	1.655	0.468
6	3000	60	22.271	10	0.343	1.296	0.301	0.576	1.667	0.493

Table C.3f

Date: 7-9-96	Power:	2000								
sample/track	speed	Mass Flow	Air	stand off	Melted Zone	width	Depth	HEZ	width	Depth
RD-65-7A	mm/min	scale unit	l/min	mm	mm^2	mm	mm	mm^2	mm	mm
1	1500	5	4.323	10	0.045	0.315	0.195	0.169	0.694	0.318
2	1500	20	10.995	10	0.074	0.465	0.212	0.215	0.864	0.326
3	1500	30	14.821	10	0.104	0.476	0.292	0.226	0.874	0.37
4	1500	40	18.109	10	0.126	0.516	0.304	0.278	0.934	0.426
5	1500	50	20.963	10	0.147	0.646	0.365	0.36	1.044	0.473
6	1500	60	23.452	10	0.153	0.549	0.357	0.331	0.95	0.462
RD-65-7B										
1	2000	5	4.323	10	0.16	0.561	0.376	0.308	0.969	0.457
2	2000	20	10.995	10	0.138	0.581	0.374	0.35	1.053	0.467
3	2000	30	14.821	10	0.154	0.597	0.396	0.348	1.066	0.479
4	2000	40	18.109	10	0.165	0.608	0.359	0.328	1.079	0.457
5	2000	50	20.963	10						
6	2000	60	23.452	10						
RD-65-7C										
1	3000	5	4.323	10	0.0085	0.49	0.405	0.405	1.263	0.412
2	3000	20	10.995	10	0.101	0.602	0.438	0.438	1.486	0.443
3	3000	30	14.821	10	0.117	0.605	0.364	0.364	1.346	0.393
4	3000	40	18.109	10	0.131	0.8	0.359	0.359	1.399	0.404
5	3000	50	20.963	10	0.133	0.951	0.391	0.391	1.382	0.41
6	3000	60	23.452	10	0.151	1.026	0.413	0.413	1.441	0.437

Table C.4 Series RD-64 Data

Table C.4a

Date: 6-5-96	Power:	2000						
sample/track	speed	Ar or Ar/So2	Sulfur	Graphite	stand off	video image	width	Depth
RD-64-1 A	mm/min	scale unit	yes/no	yes/no	mm	area mm^2	mm	mm
1	1500	5	No	No	10	0.311	1.26	0.373
2	1500	10	No	No	10	0.449	1.41	0.396
3	1500	15	No	No	10	0.421	1.353	0.418
4	1500	20	No	No	10	0.407	1.261	0.507
5	1500	25	No	No	10	0.414	1.365	0.487
6	1500	30	No	No	10	0.42	1.21	0.501
7	1500	35	No	No	10	0.459	1.249	0.473
8	1500	40	No	No	10	0.508	1.36	0.526
9	1500	45	No	No	10	0.467	1.342	0.493
10	1500	50	No	No	10	0.464	1.306	0.515
11	1500	55	No	No	10	0.48	1.293	0.557
12	1500	60	No	No	10	0.467	1.349	0.532
RD-64-1B								0.4815
1	2000	5	No	No	10	0.254	1.078	0.345
2	2000	10	No	No	10	0.268	1.136	0.332
3	2000	15	No	No	10	0.321	1.106	0.404
4	2000	20	No	No	10	0.294	1.098	0.398
5	2000	25	No	No	10	0.302	1.159	0.393
6	2000	30	No	No	10	0.366	1.189	0.438
7	2000	35	No	No	10	0.328	1.12	0.39
8	2000	40	No	No	10	0.361	1.198	0.447
9	2000	45	No	No	10	0.344	1.162	0.435
10	2000	50	No	No	10	0.324	1.134	0.408
11	2000	55	No	No	10	0.357	1.159	0.421
12	2000	60	No	No	10	0.373	1.134	0.465

Table C.4b

Date: 6-5-96	Power:	2000						
sample/track	speed: v	Ar or Ar/So2	Sulfur	Graphite	stand off	video image	width	Depth
RD-64-2A	mm/min	scale unit	yes/no	yes/no	mm	A : area mm^2	mm	mm
1	2500	5	No	No	10	0.198	1.111	0.306
2	2500	10	No	No	10	0.224	1.123	0.329
3	2500	15	No	No	10	0.271	1.203	0.348
4	2500	20	No	No	10	0.363	1.05	0.365
5	2500	25	No	No	10	0.208	0.978	0.331
6	2500	30	No	No	10	0.2	0.947	0.248
7	2500	35	No	No	10	0.229	0.978	0.331
8	2500	40	No	No	10	0.222	1.068	0.331
9	2500	45	No	No	10	0.242	0.993	0.357
10	2500	50	No	No	10	0.226	0.962	0.318
11	2500	55	No	No	10	0.195	0.879	0.306
12	2500	60	No	No	10	0.235	0.979	0.34
RD-64-2B							Avg:	0.325833333
1	3000	5	No	No	10	0.161	0.966	0.234
2	3000	10	No	No	10	0.179	1.019	0.368
3	3000	15	No	No	10	0.167	0.994	0.27
4	3000	20	No	No	10	0.192	0.953	0.329
5	3000	25	No	No	10	0.158	0.883	0.315
6	3000	30	No	No	10	0.212	0.886	0.315
7	3000	35	No	No	10	0.192	0.896	0.306
8	3000	40	No	No	10	0.169	0.782	0.324
9	3000	45	No	No	10	0.202	0.932	0.315
10	3000	50	No	No	10	0.178	0.863	0.309
11	3000	55	No	No	10	0.219	0.915	0.326
12	3000	60	No	No	10	0.192	0.985	0.315

Table C.5 Series RD-63 Data

sample/track	speed	Ar or Ar/So2	Sulfur	Graphite	stand off	video image	width	Depth
RD-63-3	mm/min	scale unit	yes/no	yes/no	mm	area mm^2	mm	mm
1	1500	30	No	No	20	0.455	1.967	0.337
2	2000	30	No	No	20	0.347	1.841	0.273
3	2500	30	No	No	20	0.29	1.652	0.234
4	3000	30	No	No	20	0.156	1.908	0.136
5	1500	30	yes	No	20	0.391	1.788	0.32
6	2000	30	yes	No	20	0.358	1.925	0.292
7	2500	30	yes	No	20	0.277	1.975	0.145
8	3000	30	yes	No	20	0.191	1.652	0.164
9	1500	30	No	Yes	20	0.562	2.112	0.329
10	2000	30	No	Yes	20	0.482	1.886	0.304
11	2500	30	No	Yes	20	0.489	2.42	0.239
12	3000	30	No	Yes	20	0.515	2.509	0.226
13	1500	30	yes	Yes	20	0.426	2.154	0.262
14	2000	30	yes	Yes	20	0.5	2.173	0.265
15	2500	30	yes	Yes	20	0.476	2.271	0.262
16	3000	30	yes	Yes	20	0.705	2.544	0.359

APPENDIX D

Table D.1 Regression Data of Shielding Gases

sample/track:	RD-66-1A	RD-66-3A	RD-66-4A	RD-66-5A	RD-66-6A	RD-66-7A
	Ar	Nitrogen	Helium	Oxygen	Air	CO2
β[0]	0.433773542	0.382927313	0.344910769	0.43628325	0.431633643	0.278380177
β[1]	0.044209924	0.080847541	0.773518726	0.094873882	0.124674047	0.332828453
r^2	0.053199479	0.179844356	0.552639055	0.234299063	0.160894931	0.971575408
sample/track:	YRD-66-1A	YRD-66-3A	YRD-66-4A	YRD-66-5A	YRD-66-6A	RD-66-7A
	Ar	Nitrogen	Helium	Oxygen	Air	CO2
β[0]	0.2032836	0.201148984	0.355919029	0.627304719	0.728337673	0.278380177
β[1]	0.437101286	0.493361443	3.2215642	1.205415845	0.395097187	0.332828453
r^2	0.63342606	0.54135337	0.84650632	0.905861064	0.370833909	0.971575408

Table D.2 Modified Regression Data for Equation 5.1

sample/track:	RD-66-1A	RD-66-3A	RD-66-4A	RD-66-5A	RD-66-6A	RD-66-7A
Modified	Ar	Nitrogen	Helium	Oxygen	Air	CO2
β_0	1289.457616	1138.30949	1025.299551	1296.918104	1283.096441	827.5272794
β_1	131.4207015	240.3315737	2299.401684	282.0269988	370.6125059	989.3830345
sample/track:	YRD-66-1A	YRD-66-3A	YRD-66-4A	YRD-66-5A	YRD-66-6A	RD-66-7A
Modified	Ar	Nitrogen	Helium	Oxygen	Air	CO2
β_0	559.5474822	553.6718525	979.6835367	1726.68516	2004.783024	766.2542714
β_1	1203.141442	1358.000117	8867.503991	3317.96269	1087.523224	916.1256614

Graph Series D.1: RD-66 Regression and Confidence Graphs.

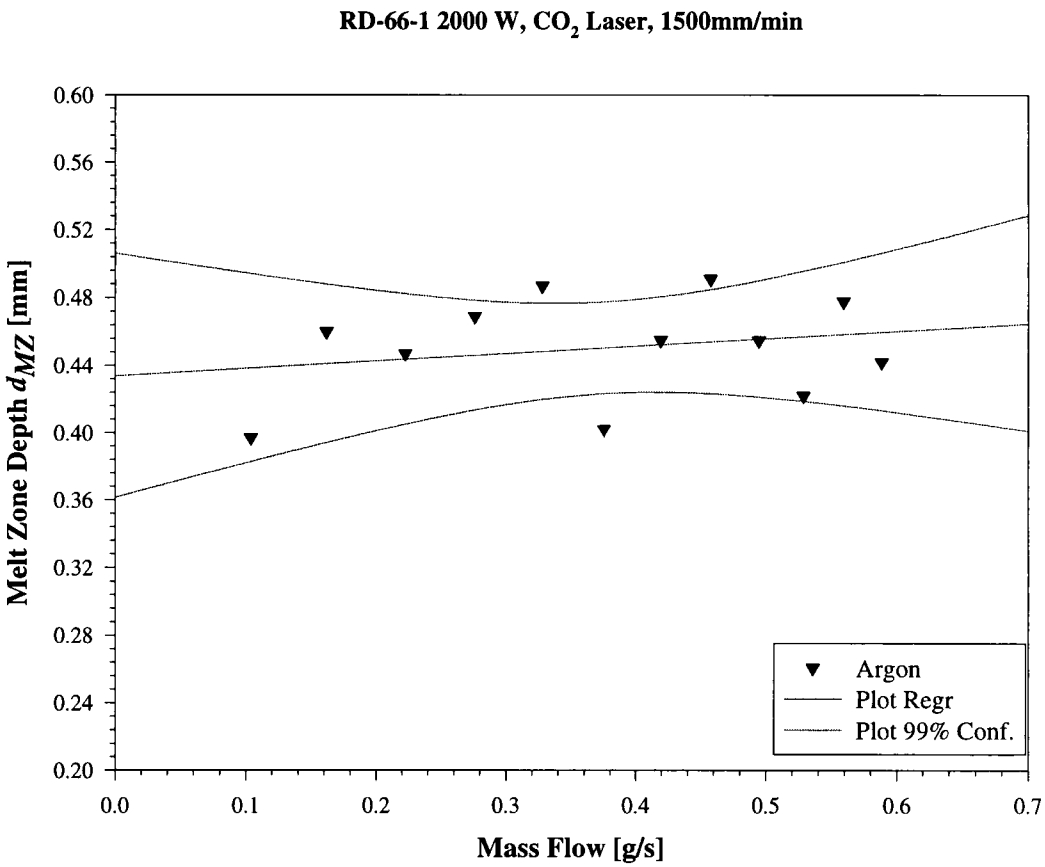

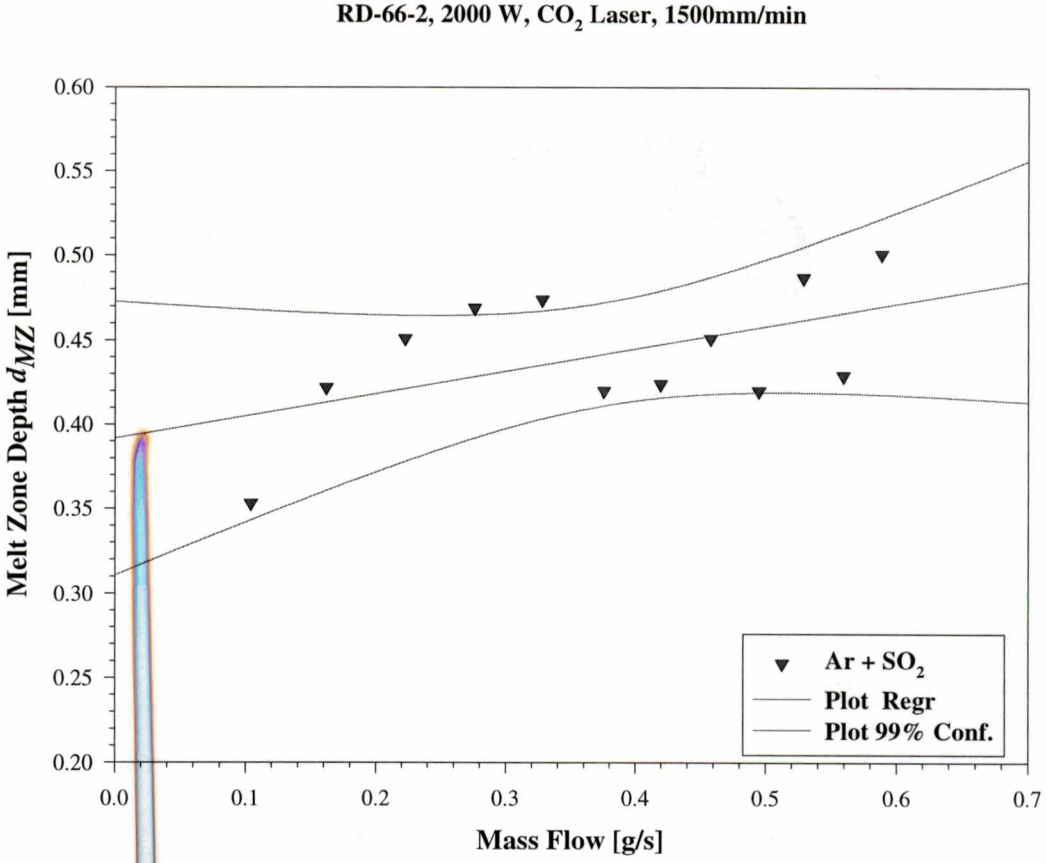
RD-66-2, 2000 W, CO2 Laser, 1500mm/min
Melt Zone Depth dMZ [mm]
0.60
0.55
0.50
0.45
0.40
0.35
0.30
0.25
0.20
0.0
0.1
0.2
0.3
0.4
0.5
0.6
0.7
Mass Flow [g/s]
Ar + SO2
Plot Regr
Plot 99% Conf.

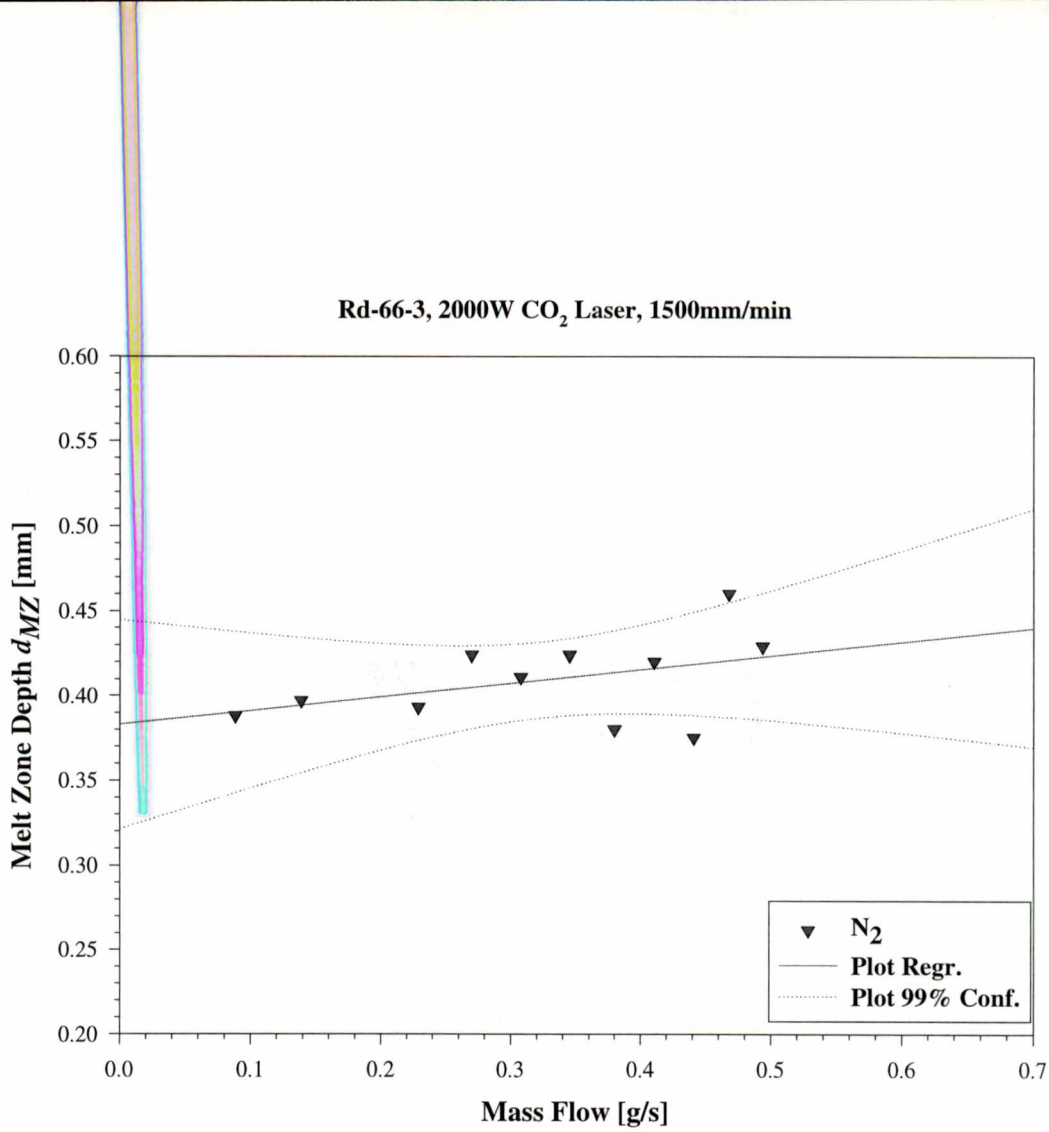
Rd-66-3, 2000W CO_2 Laser, 1500mm/min
Melt Zone Depth d_{MZ} [mm]
0.60
0.55
0.50
0.45
0.40
0.35
0.30
0.25
0.20
0.0
0.1
0.2
0.3
0.4
0.5
0.6
0.7
Mass Flow [g/s]
N_2
Plot Regr.
Plot 99% Conf.

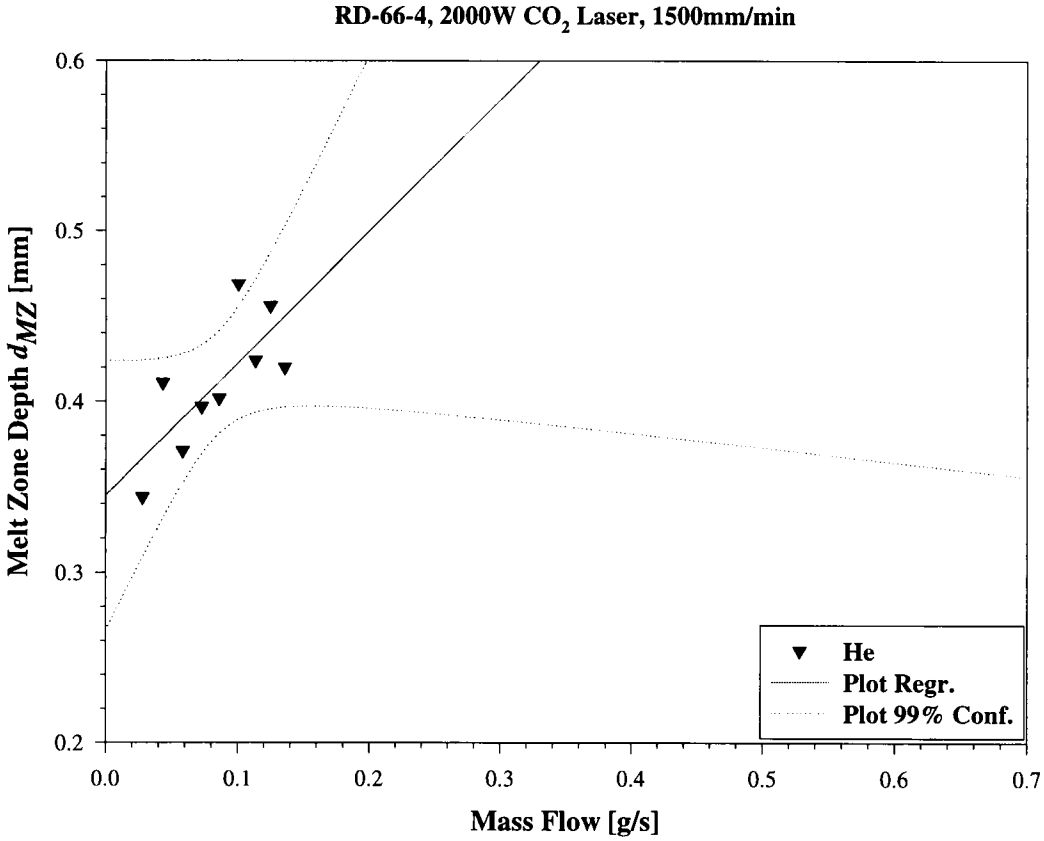
RD-66-4, 2000W CO_2 Laser, 1500mm/min
Melt Zone Depth d_{MZ} [mm]
0.6
0.5
0.4
0.3
0.2
0.0
0.1
0.2
0.3
0.4
0.5
0.6
0.7
Mass Flow [g/s]
He
Plot Regr.
Plot 99% Conf.

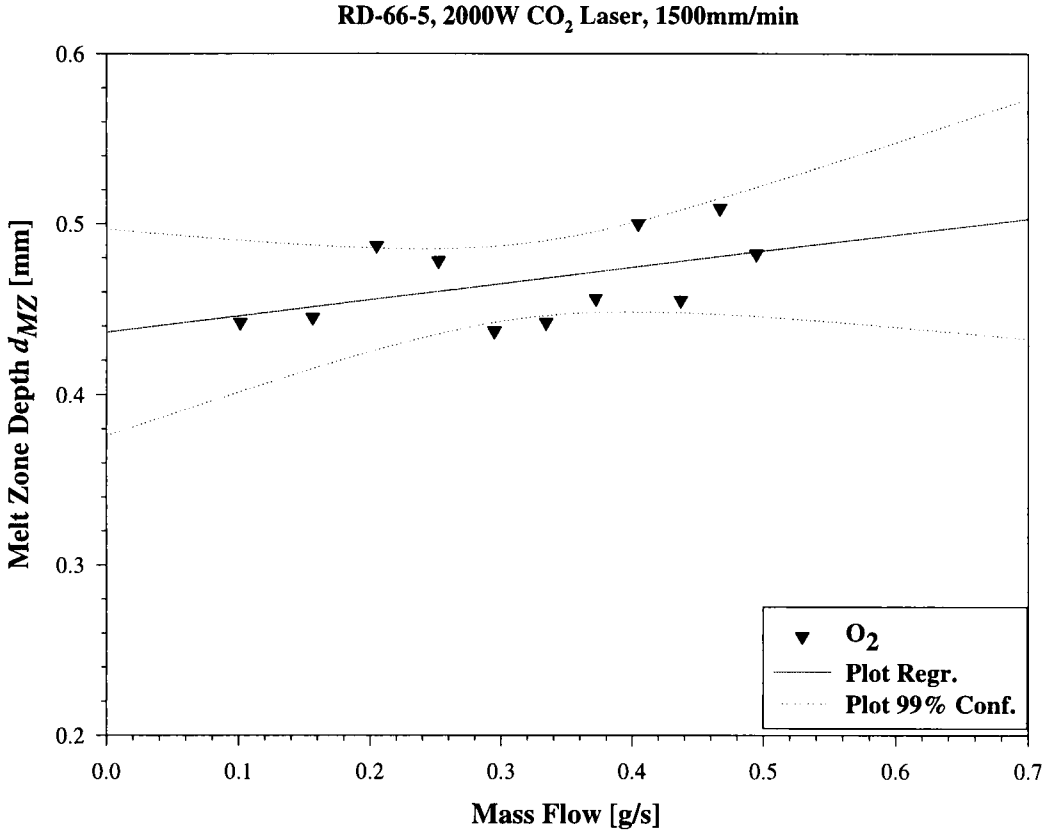
RD-66-5, 2000W CO_2 Laser, 1500mm/min
Melt Zone Depth d_{MZ} [mm]
0.6
0.5
0.4
0.3
0.2
0.0
0.1
0.2
0.3
0.4
0.5
0.6
0.7
Mass Flow [g/s]
O_2
Plot Regr.
Plot 99% Conf.

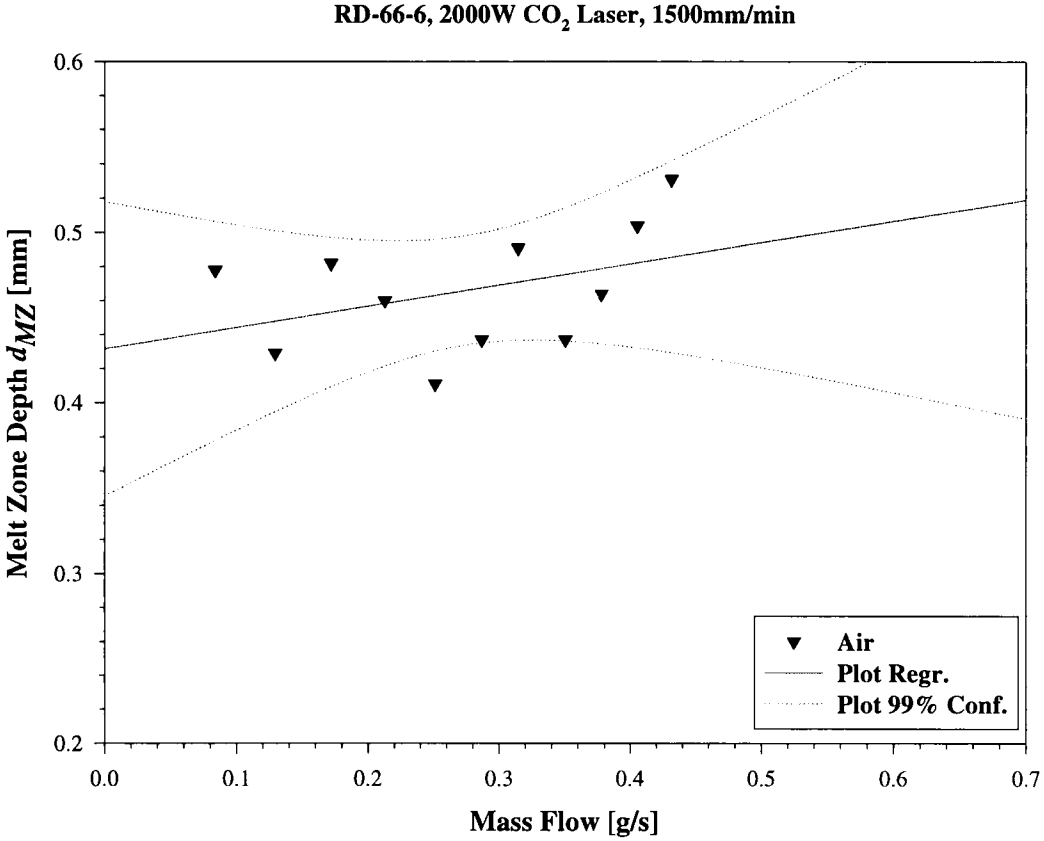
RD-66-6, 2000W CO_2 Laser, 1500mm/min
Melt Zone Depth d_{MZ} [mm]
0.6
0.5
0.4
0.3
0.2
0.0
0.1
0.2
0.3
0.4
0.5
0.6
0.7
Mass Flow [g/s]
Air
Plot Regr.
Plot 99% Conf.

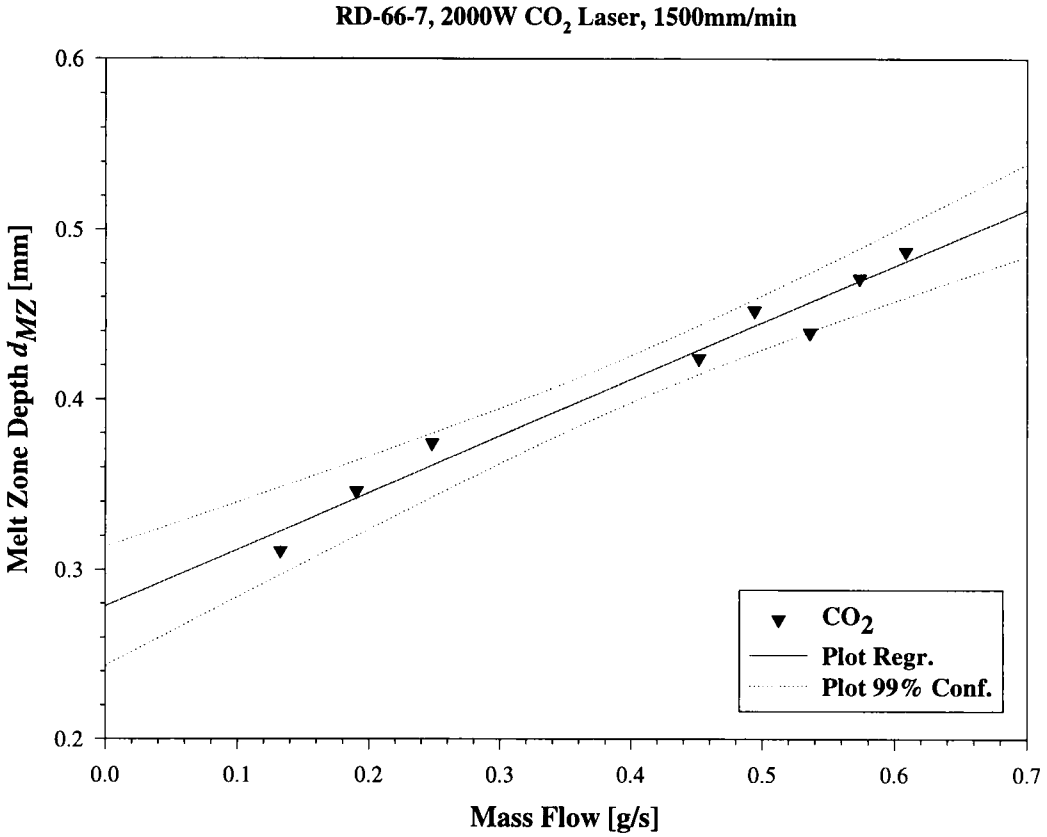
RD-66-7, 2000W CO_2 Laser, 1500mm/min
Melt Zone Depth d_{MZ} [mm]
0.6
0.5
0.4
0.3
0.2
0.0
0.1
0.2
0.3
0.4
0.5
0.6
0.7
Mass Flow [g/s]
CO_2
Plot Regr.
Plot 99% Conf.

Graph Series D.2:YRD-66 Regression and Confidence Graphs

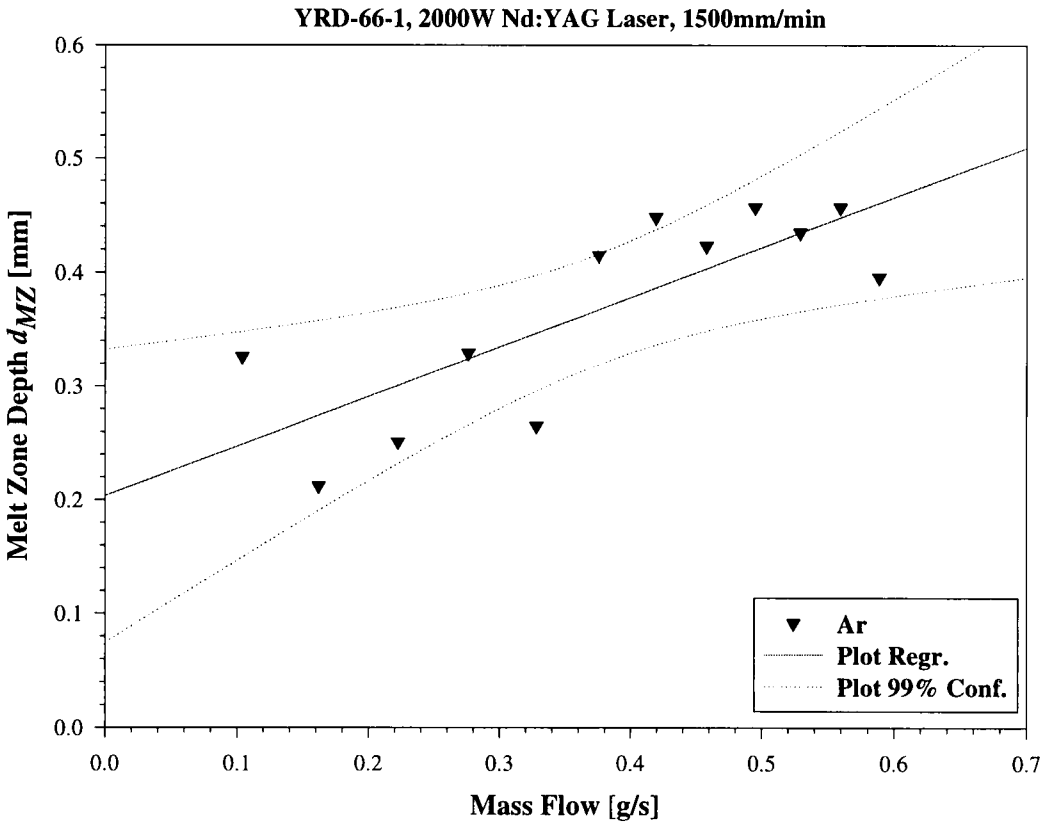

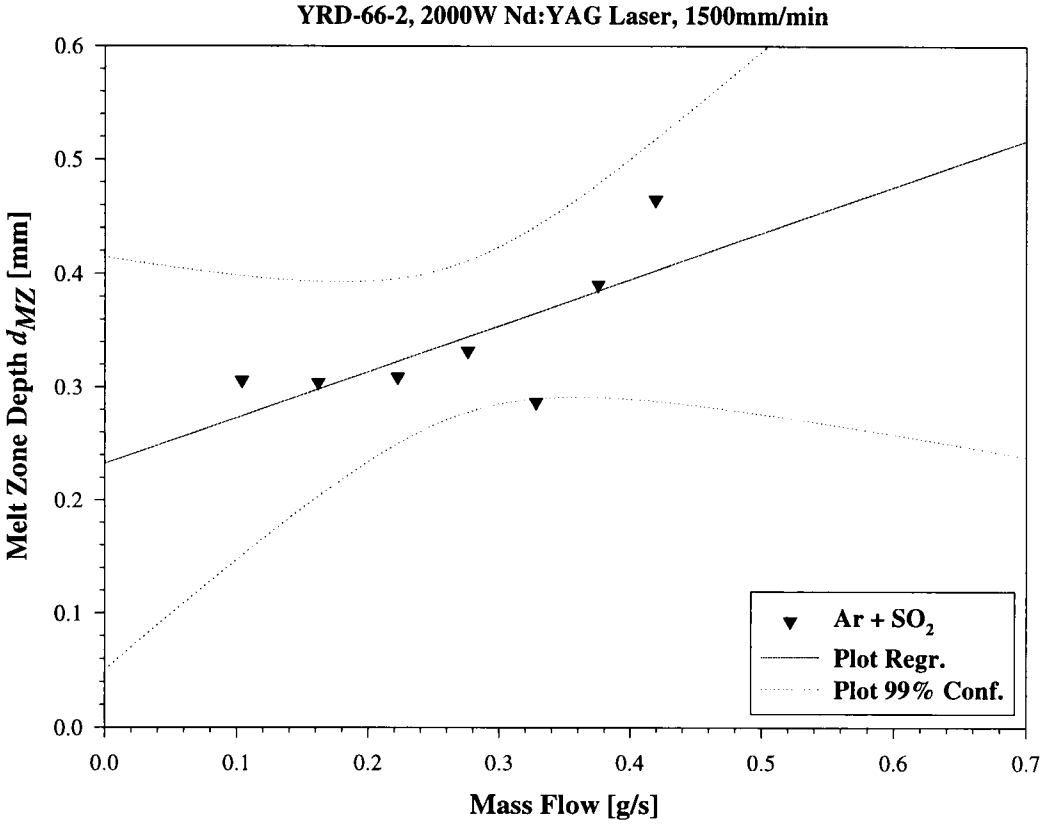
YRD-66-2, 2000W Nd:YAG Laser, 1500mm/min
Melt Zone Depth d_{MZ} [mm]
Mass Flow [g/s]
0.0
0.1
0.2
0.3
0.4
0.5
0.6
0.7
Ar + SO_2
Plot Regr.
Plot 99% Conf.

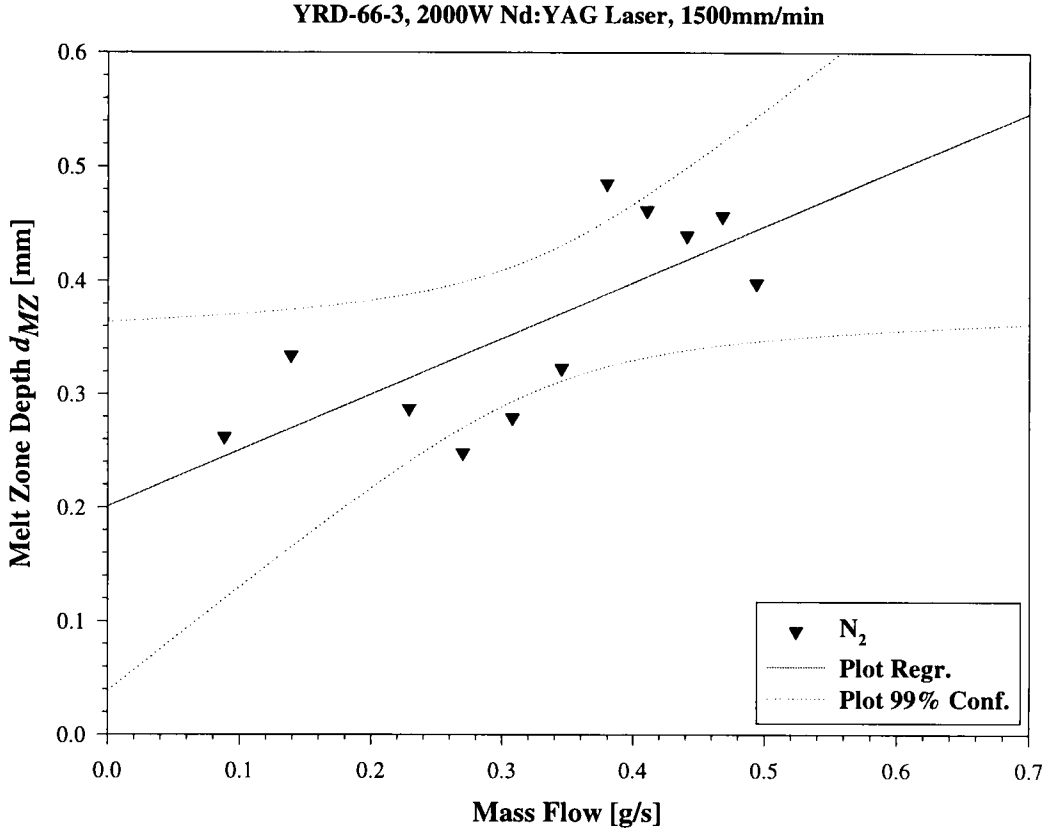
YRD-66-3, 2000W Nd:YAG Laser, 1500mm/min
Melt Zone Depth d_{MZ} [mm]
0.0
0.1
0.2
0.3
0.4
0.5
0.6
0.0
0.1
0.2
0.3
0.4
0.5
0.6
0.7
Mass Flow [g/s]
N_2
Plot Regr.
Plot 99% Conf.

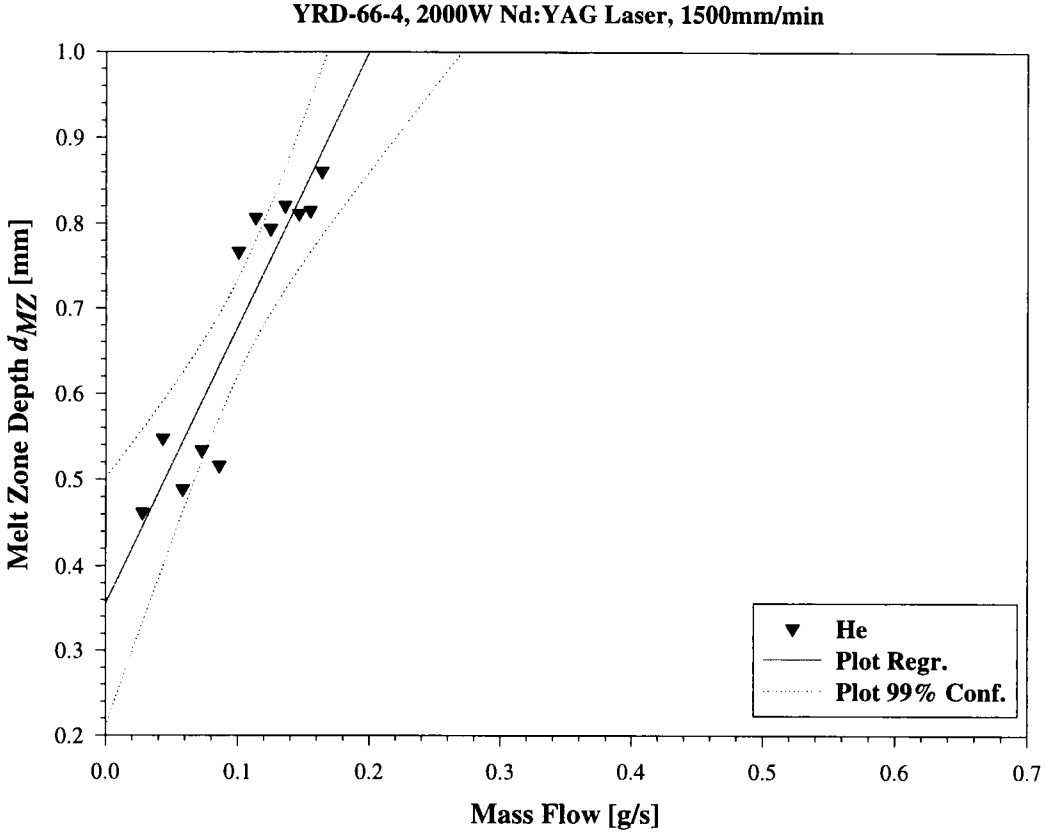
YRD-66-4, 2000W Nd:YAG Laser, 1500mm/min
Melt Zone Depth d_{MZ} [mm]
1.0
0.9
0.8
0.7
0.6
0.5
0.4
0.3
0.2
0.0
0.1
0.2
0.3
0.4
0.5
0.6
0.7
Mass Flow [g/s]
He
Plot Regr.
Plot 99% Conf.

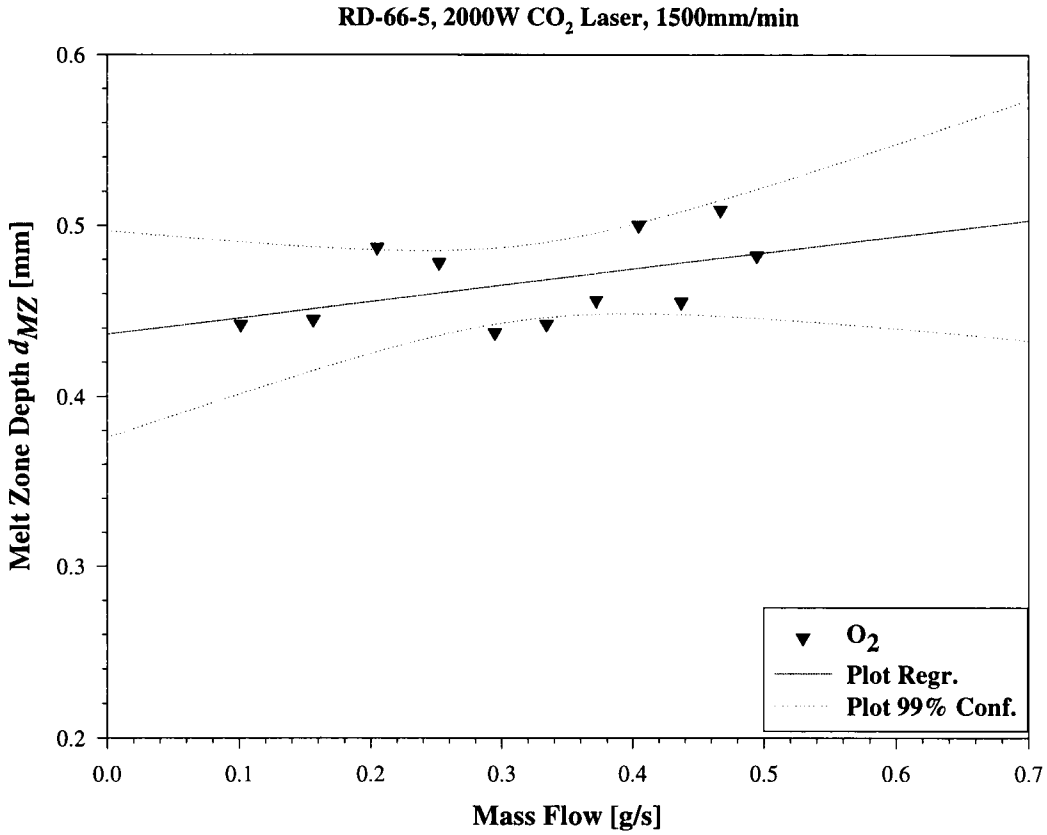
RD-66-5, 2000W CO_2 Laser, 1500mm/min
Melt Zone Depth d_{MZ} [mm]
0.6
0.5
0.4
0.3
0.2
0.0
0.1
0.2
0.3
0.4
0.5
0.6
0.7
Mass Flow [g/s]
O_2
Plot Regr.
Plot 99% Conf.

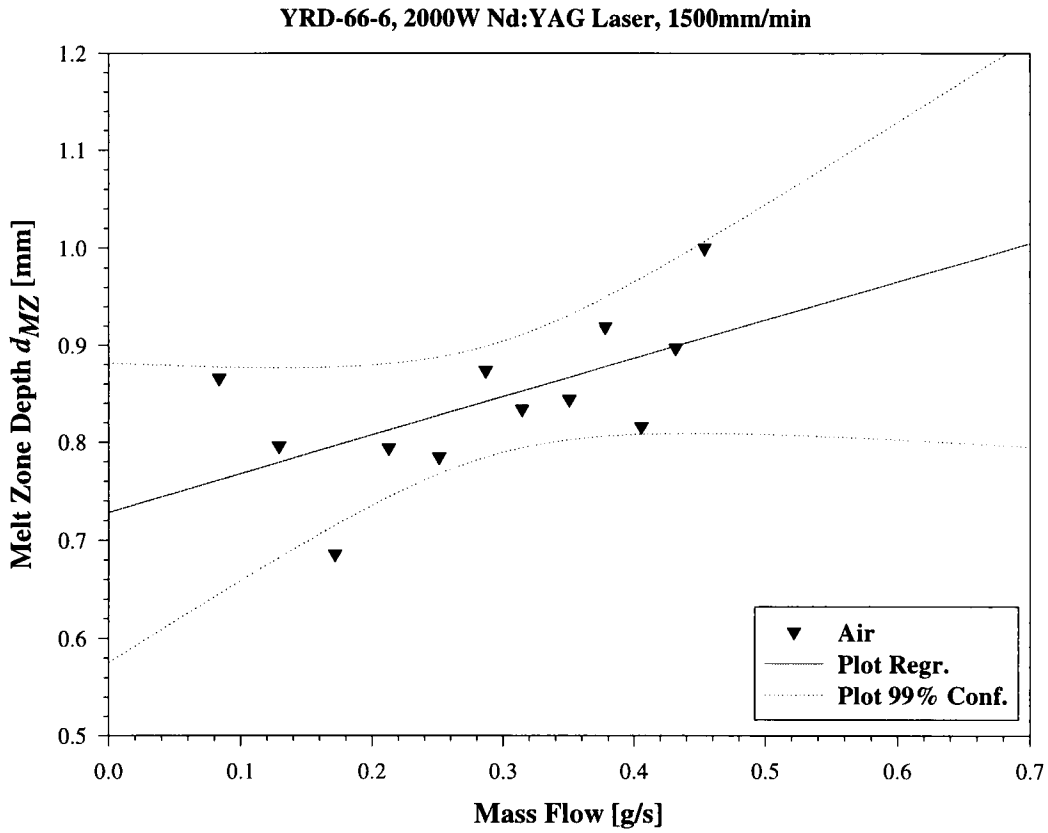
YRD-66-6, 2000W Nd:YAG Laser, 1500mm/min
Melt Zone Depth d_{MZ} [mm]
1.2
1.1
1.0
0.9
0.8
0.7
0.6
0.5
0.0
0.1
0.2
0.3
0.4
0.5
0.6
0.7
Mass Flow [g/s]
Air
Plot Regr.
Plot 99% Conf.

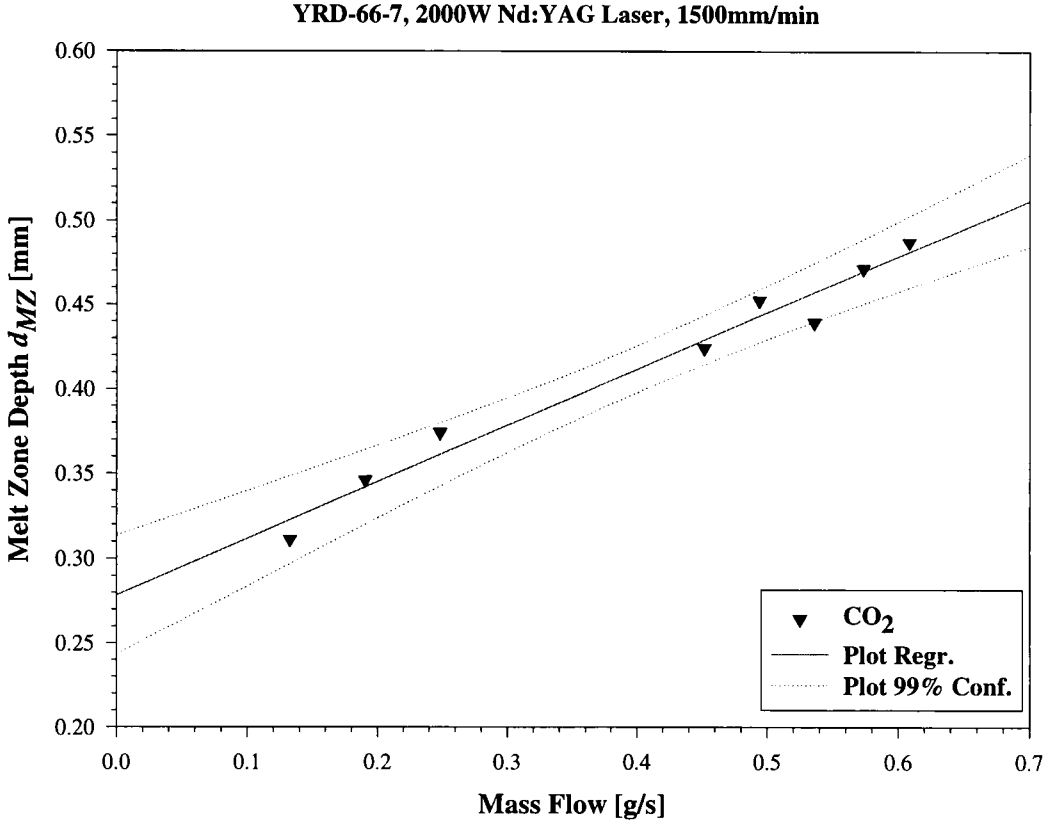
YRD-66-7, 2000W Nd:YAG Laser, 1500mm/min
Melt Zone Depth d_{MZ} [mm]
0.60
0.55
0.50
0.45
0.40
0.35
0.30
0.25
0.20
0.0
0.1
0.2
0.3
0.4
0.5
0.6
0.7
Mass Flow [g/s]
CO_2
Plot Regr.
Plot 99% Conf.

APPENDIX E

Graph Series E.1 and Table Series E.1: Plasma Table of Data and Graphs

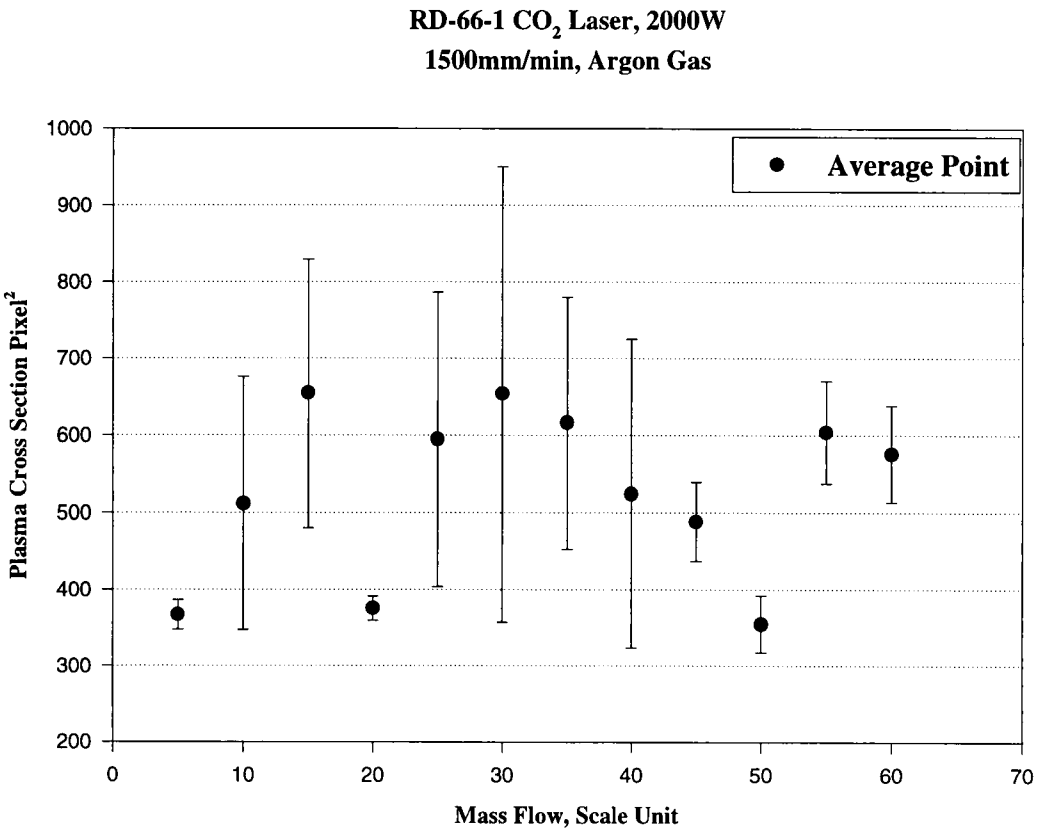

Argon												
Mass Flow Scale Unit	**5**	**10**	**15**	**20**	**25**	**30**	**35**	**40**	**45**	**50**	**55**	**60**
Plasma Size Pixel^2	381	320	424	381	420	356	652	266	420	315	524	656
"	352	720	615	352	469	994	833	488	503	350	599	593
"	387	521	791	387	840	804	490	604	542	405	686	539
"	350	486	789	382	652	462	491	740	489	350	608	516
Average For each track	**367.5**	**511.75**	**654.75**	**375.5**	**595.25**	**654**	**616.5**	**524.5**	**488.5**	**355**	**604.25**	**576**

RD-66-2, CO_2 Laser, 2000W
1500mm/min, Ar+SO_2 Gas

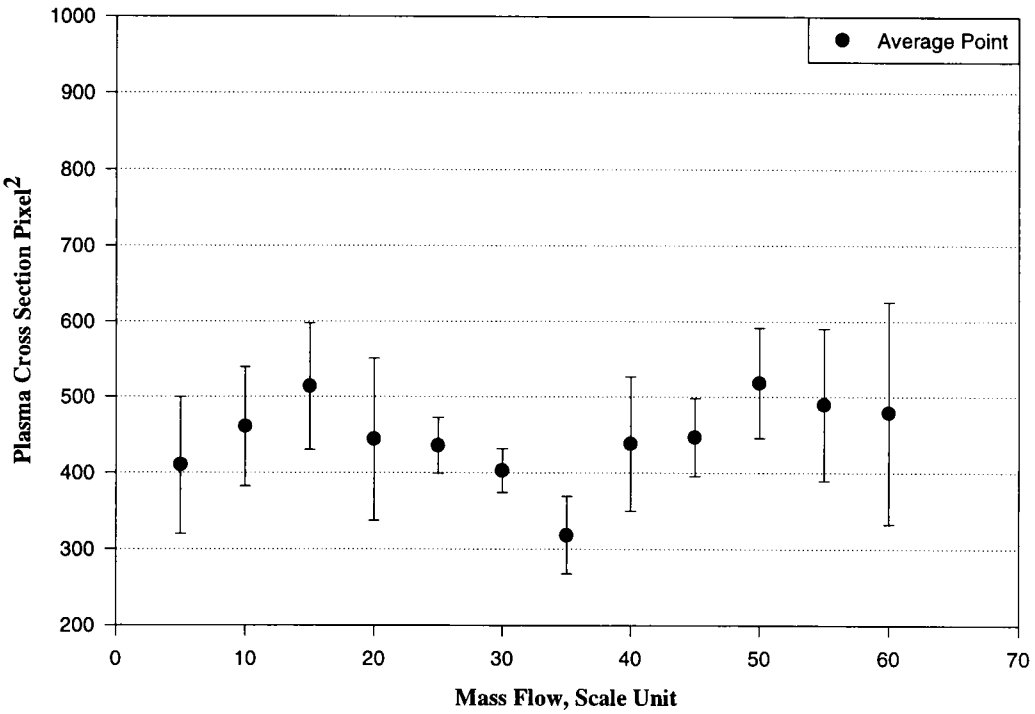

Argon+SO2												
Mass Flow Scale Unit	**5**	**10**	**15**	**20**	**25**	**30**	**35**	**40**	**45**	**50**	**55**	**60**
Plasma Size Pixel^2	511	436	605	597	474	420	331	306	385	475	399	572
"	356	566	407	373	397	360	384	487	427	506	626	632
"	316	378	498	369	459	413	268	483	502	468	431	321
"	457	464	546	438	413	418	291	477	473	625	504	392
Average For each track	**410**	**461**	**514**	**444.25**	**435.75**	**402.75**	**318.5**	**438.25**	**446.75**	**518.5**	**490**	**479.25**

RD-66-3; CO_2 Laser, 2000W
1500mm/min, Nitrogen Gas

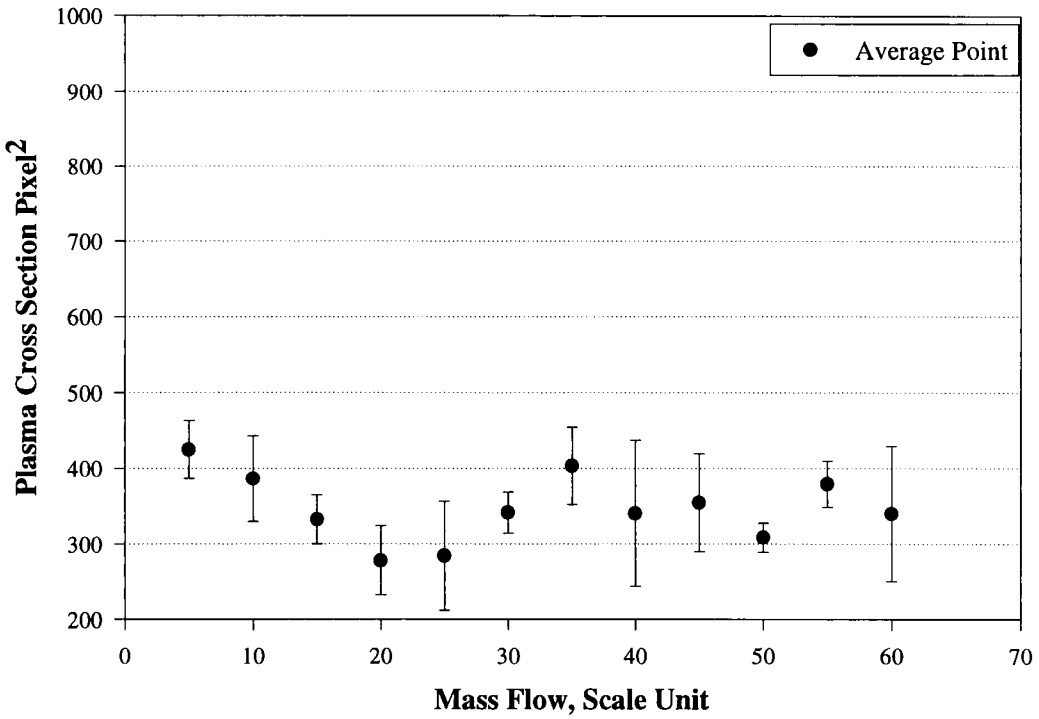

Nitrogen												
Mass Flow Scale Unit	**5**	**10**	**15**	**20**	**25**	**30**	**35**	**40**	**45**	**50**	**55**	**60**
Plasma Size Pixel^2	441	415	338	341	381	319	457	301	440	283	377	267
"	420	448	318	280	284	325	415	485	369	326	362	259
"	374	320	299	233	266	343	408	295	313	305	355	402
"	464	362	375	259	207	380	334	281	297	320	423	432
Average For each track	**424.75**	**386.25**	**332.5**	**278.25**	**284.5**	**341.75**	**403.5**	**340.5**	**354.75**	**308.5**	**379.25**	**340**

RD-66-4, CO_2 Laser, 2000W
1500mm/min, Helium Gas

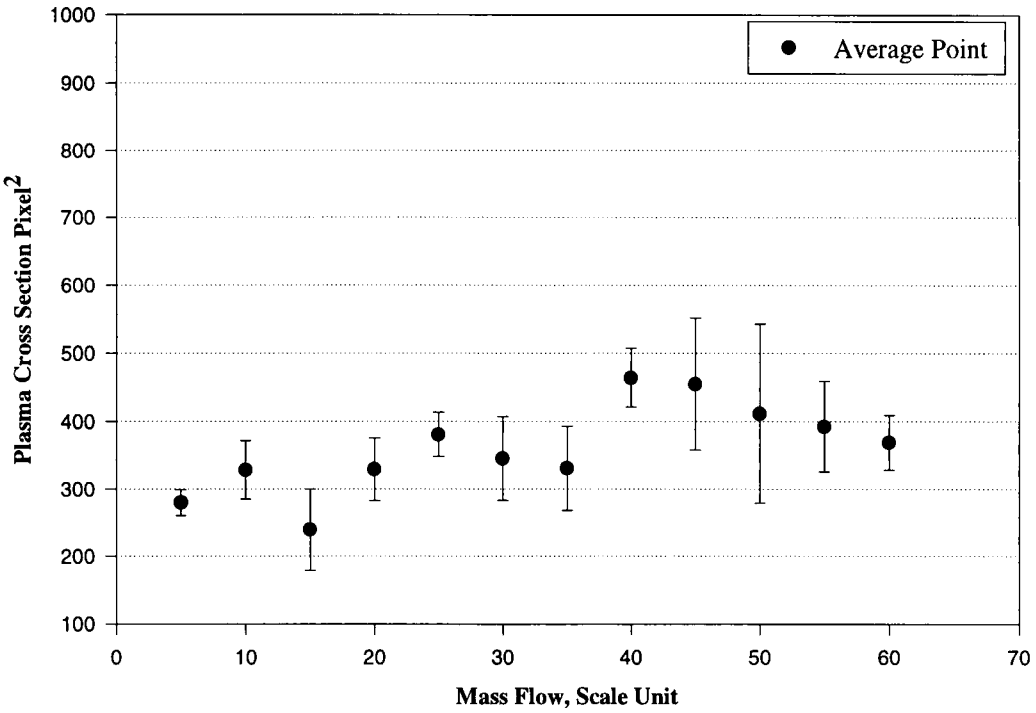

Helium												
Mass Flow Scale Unit	**5**	**10**	**15**	**20**	**25**	**30**	**35**	**40**	**45**	**50**	**55**	**60**
Plasma Size Pixel^2	255	275	191	391	406	329	307	476	377	530	322	355
"	286	344	248	293	362	294	253	467	588	520	462	388
"	301	377	322	338	410	435	384	509	465	308	435	412
"	278	317	197	294	344	322	378	405	389	286	350	319
Average For each track	**280**	**328.25**	**239.5**	**329**	**380.5**	**345**	**330.5**	**464.25**	**454.75**	**411**	**392.25**	**368.5**

RD-66-5, CO_2 Laser, 2000W
1500mm/min, Oxygen Gas

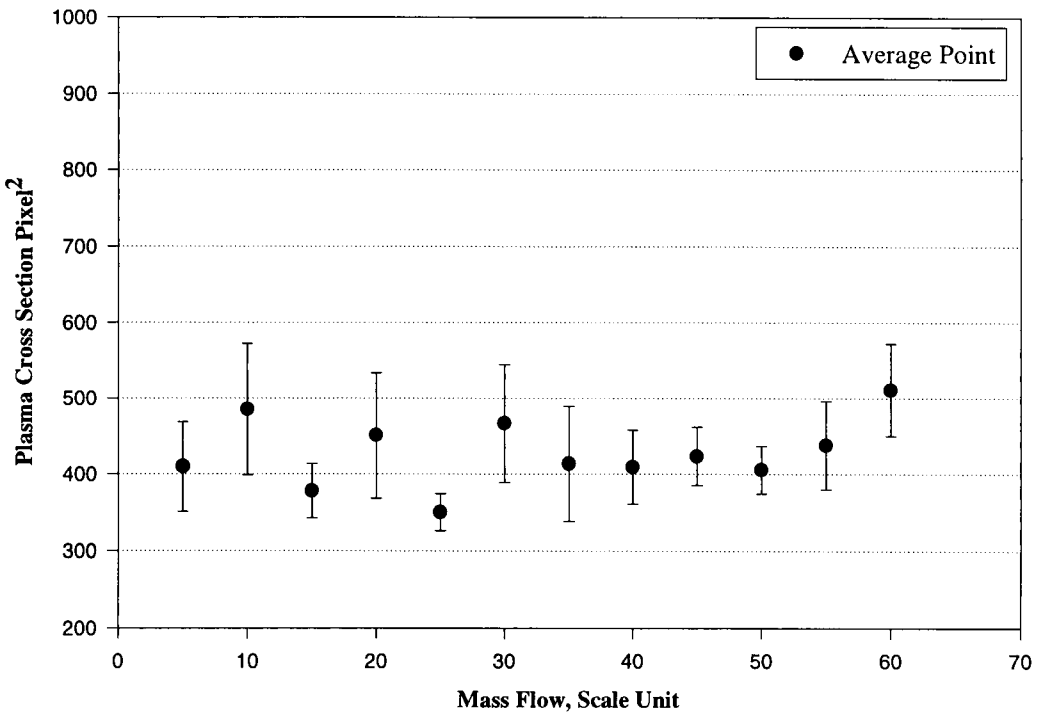

Oxygen												
Mass Flow Scale Unit	**5**	**10**	**15**	**20**	**25**	**30**	**35**	**40**	**45**	**50**	**55**	**60**
Plasma Size Pixel^2	485	551	355	405	377	456	488	470	472	377	493	561
"	351	535	388	572	358	497	355	426	408	400	356	558
"	379	360	424	392	347	365	343	373	432	450	450	493
"	425	496	346	435	320	549	469	368	382	396	453	432
Average For each track	**410**	**485.5**	**378.25**	**451**	**350.5**	**466.75**	**413.75**	**409.25**	**423.5**	**405.75**	**438**	**511**

RD-66-6, CO_2 Laser, 2000W
1500mm/min, Air

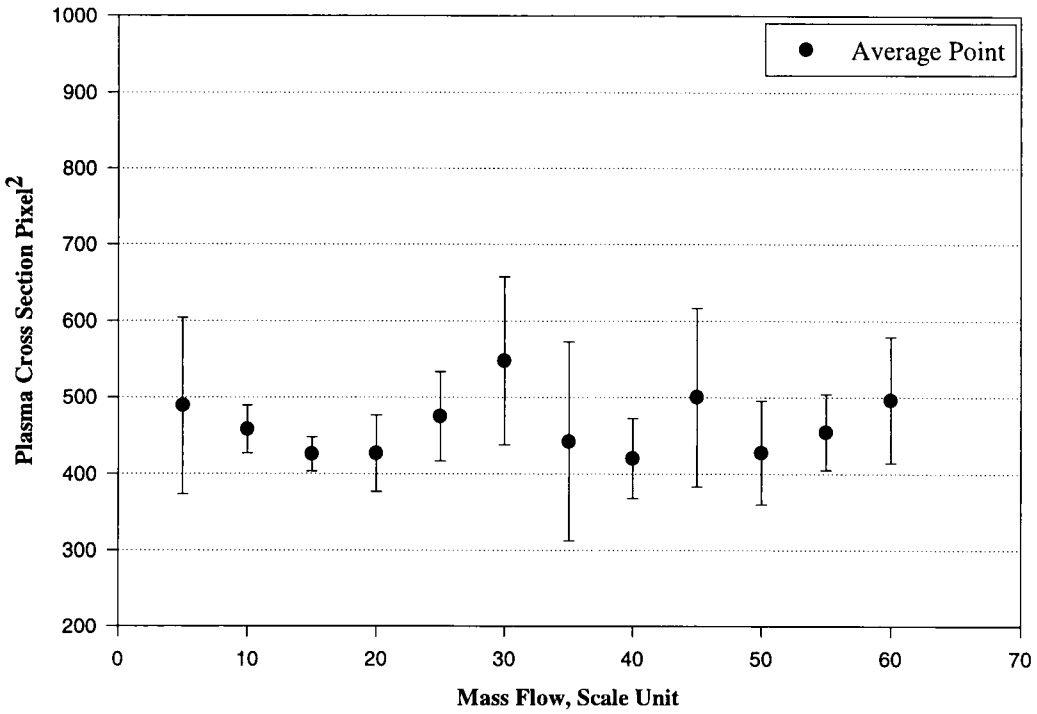

Air												
Mass Flow Scale Unit	**5**	**10**	**15**	**20**	**25**	**30**	**35**	**40**	**45**	**50**	**55**	**60**
Plasma Size Pixel^2	646	470	416	472	499	492	534	486	548	485	528	601
"	499	496	413	441	462	436	571	438	642	487	440	523
"	431	427	459	356	538	689	358	383	387	363	427	430
"	380	439	415	438	401	574	306	374	425	375	423	432
Average For each track	**489**	**458**	**425.75**	**426.75**	**475**	**547.75**	**442.25**	**420.25**	**500.5**	**427.5**	**454.5**	**496.5**

RD-66-7, CO_2 Laser, 2000W
1500mm/min, CO_2 Gas

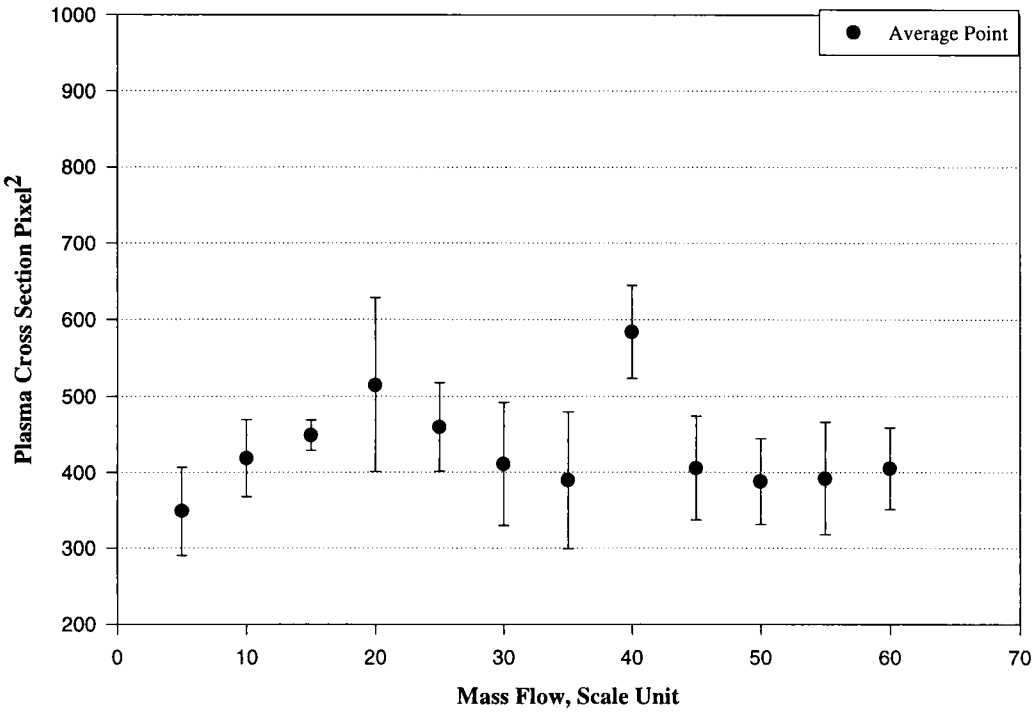

CO2												
Mass Flow Scale Unit	**5**	**10**	**15**	**20**	**25**	**30**	**35**	**40**	**45**	**50**	**55**	**60**
Plasma Size Pixel^2	393	439	441	383	473	411	464	593	469	421	500	453
"	325	355	425	526	477	475	269	653	380	369	376	408
"	277	405	470	491	376	296	372	586	320	445	335	430
"	399	475	460	659	512	461	453	505	453	317	356	329
Average For each track	**348.5**	**418.5**	**449**	**514.75**	**459.5**	**410.75**	**389.5**	**584.25**	**405.5**	**388**	**391.75**	**405**

Graph Series E.2: Plasma Size vs. Melt Zone Correlation Plots

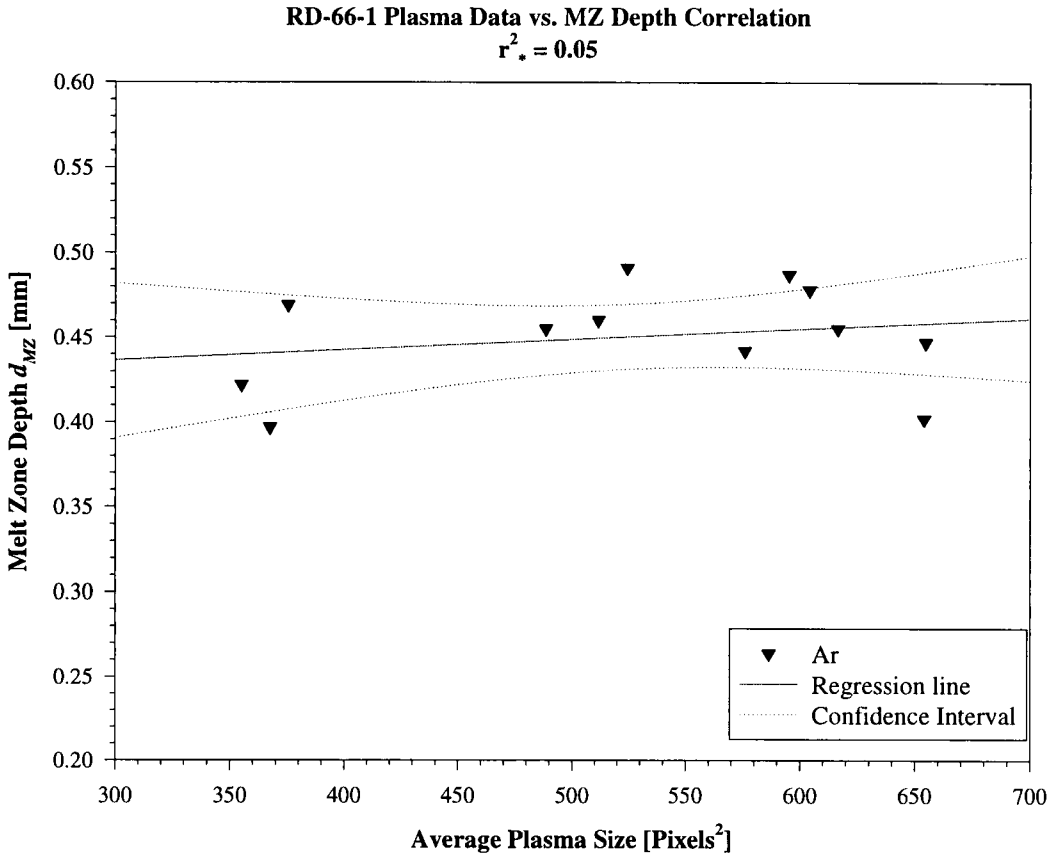

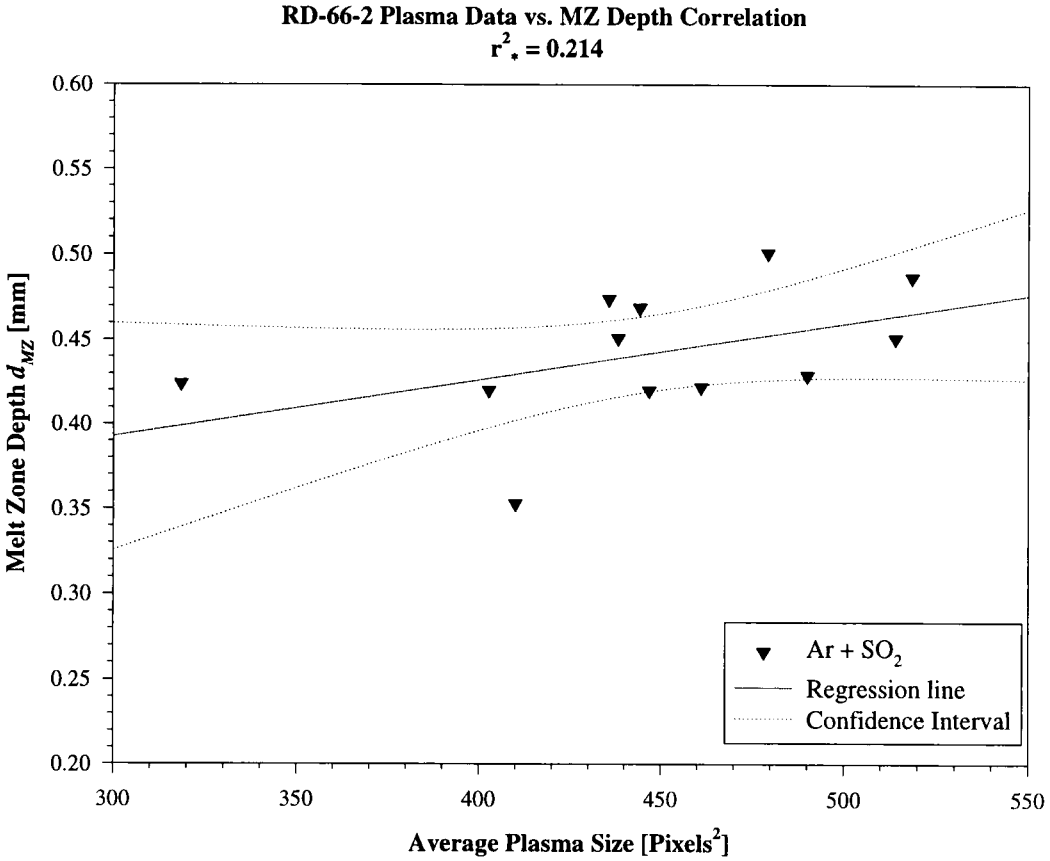
RD-66-2 Plasma Data vs. MZ Depth Correlation
$r^2_* = 0.214$
Melt Zone Depth d_{MZ} [mm]
0.60
0.55
0.50
0.45
0.40
0.35
0.30
0.25
0.20
300
350
400
450
500
550
Average Plasma Size [Pixels^2]
Ar + SO_2
Regression line
Confidence Interval

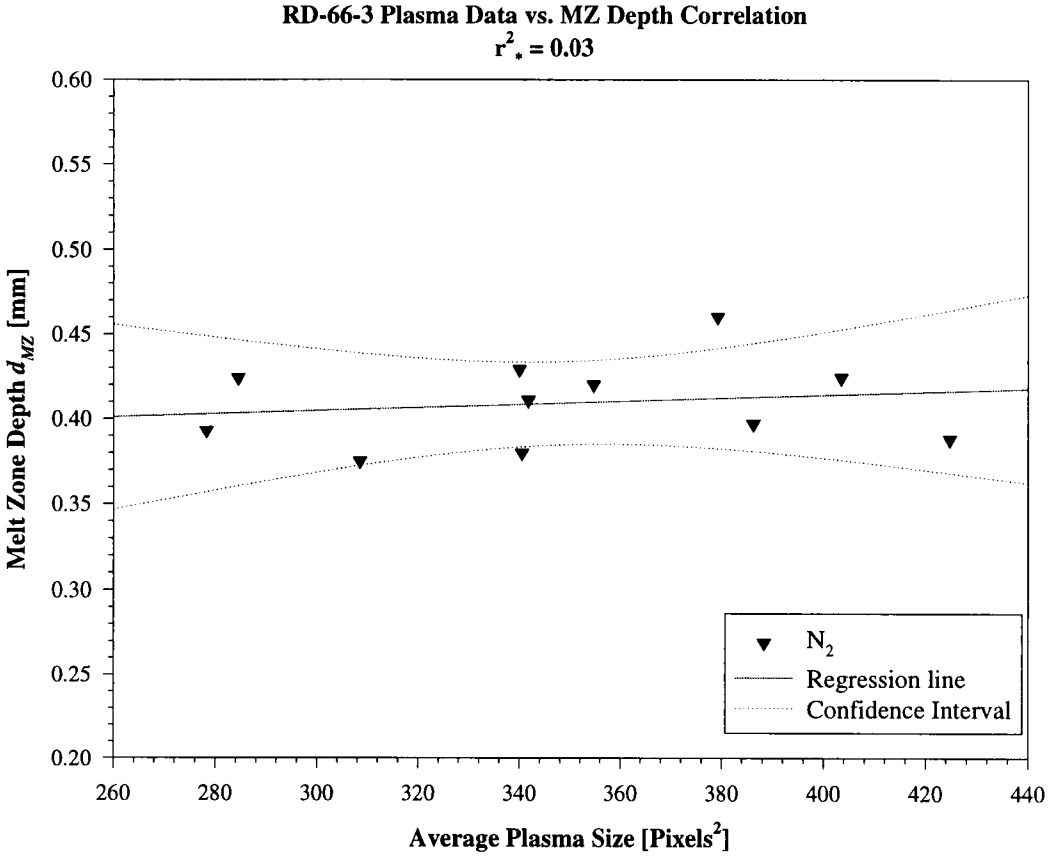
RD-66-3 Plasma Data vs. MZ Depth Correlation
$r^2_* = 0.03$
Melt Zone Depth d_{MZ} [mm]
0.60
0.55
0.50
0.45
0.40
0.35
0.30
0.25
0.20
260
280
300
320
340
360
380
400
420
440
Average Plasma Size [Pixels^2]
N_2
Regression line
Confidence Interval

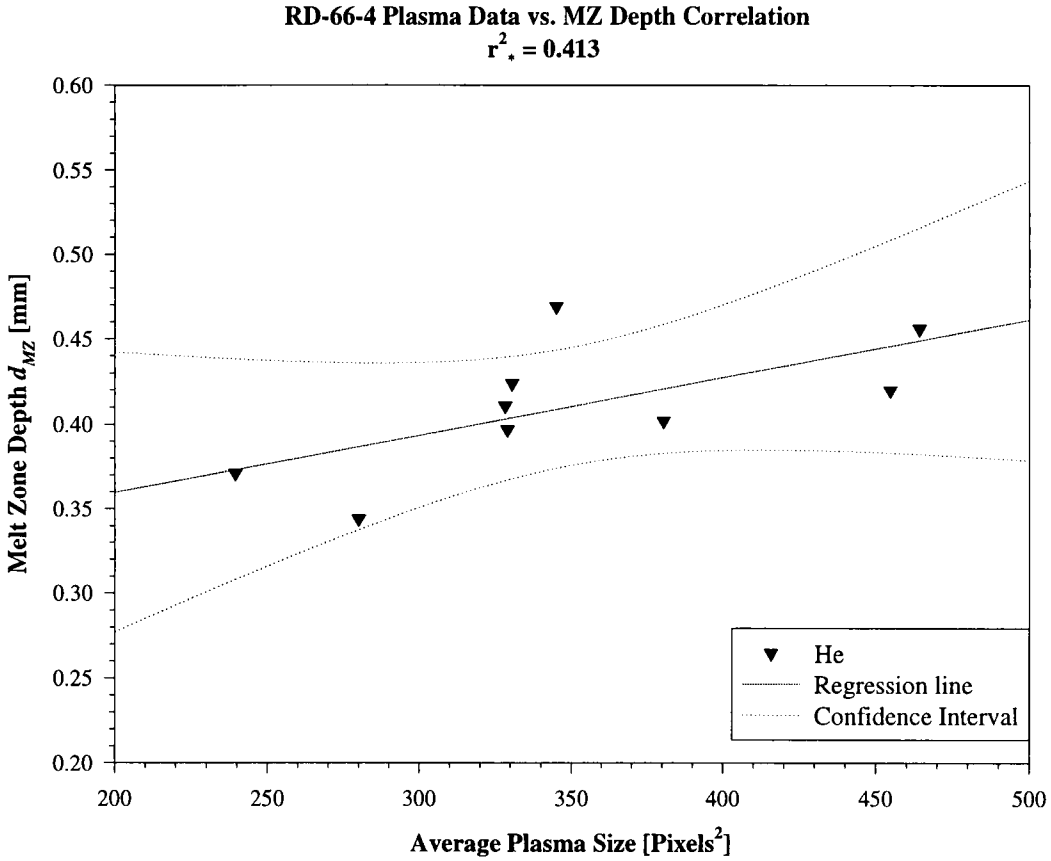
RD-66-4 Plasma Data vs. MZ Depth Correlation
$r^2_* = 0.413$
Melt Zone Depth d_{MZ} [mm]
0.60
0.55
0.50
0.45
0.40
0.35
0.30
0.25
0.20
200
250
300
350
400
450
500
Average Plasma Size [Pixels^2]
He
Regression line
Confidence Interval

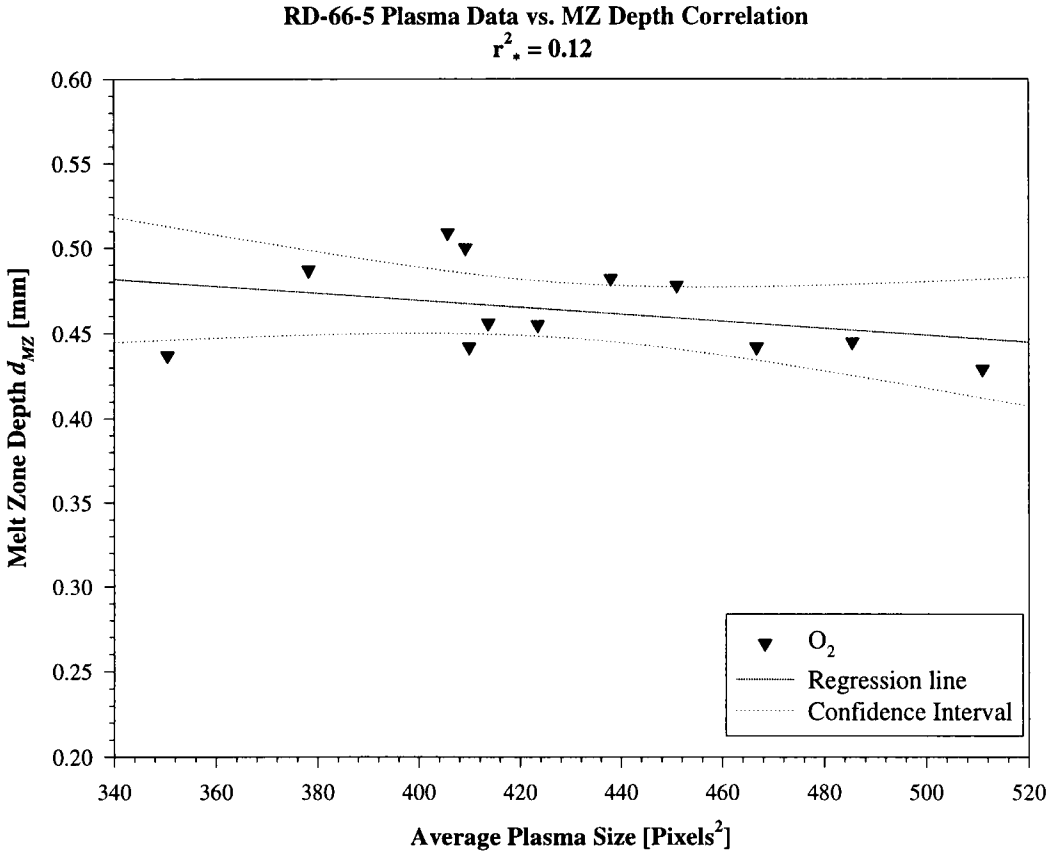
RD-66-5 Plasma Data vs. MZ Depth Correlation
$r^2_* = 0.12$
Melt Zone Depth d_{MZ} [mm]
0.60
0.55
0.50
0.45
0.40
0.35
0.30
0.25
0.20
340
360
380
400
420
440
460
480
500
520
Average Plasma Size [Pixels^2]
O_2
Regression line
Confidence Interval

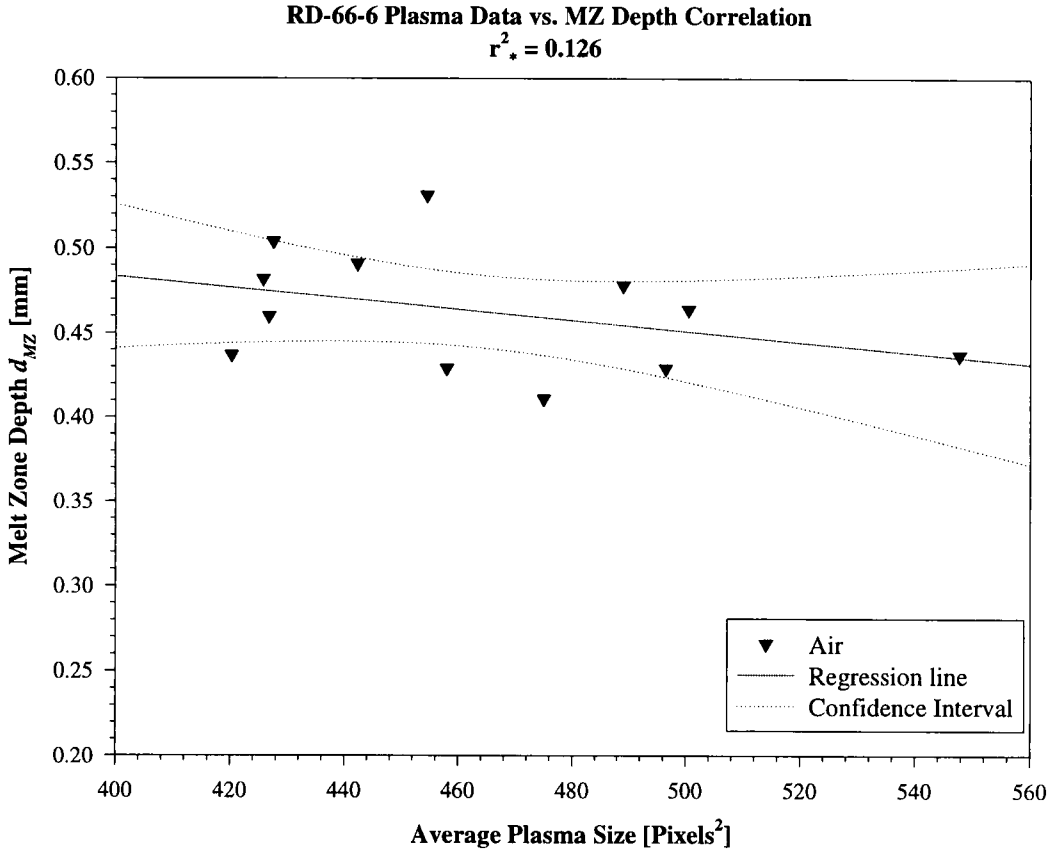
RD-66-6 Plasma Data vs. MZ Depth Correlation
$r^2_* = 0.126$
Melt Zone Depth d_{MZ} [mm]
0.60
0.55
0.50
0.45
0.40
0.35
0.30
0.25
0.20
400
420
440
460
480
500
520
540
560
Average Plasma Size [Pixels^2]
Air
Regression line
Confidence Interval

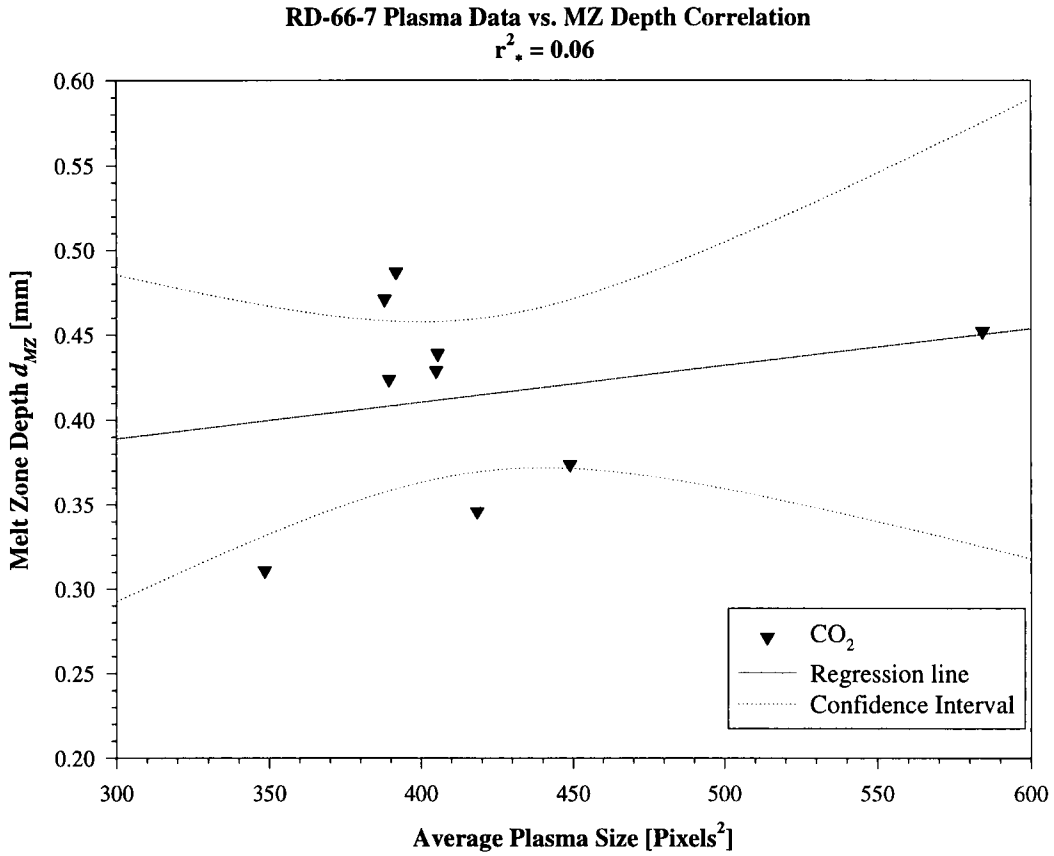
RD-66-7 Plasma Data vs. MZ Depth Correlation
$r^2_* = 0.06$
Melt Zone Depth d_{MZ} [mm]
0.60
0.55
0.50
0.45
0.40
0.35
0.30
0.25
0.20
300
350
400
450
500
550
600
Average Plasma Size [Pixels^2]
CO_2
Regression line
Confidence Interval

VITA

Farhad Nazeradl was born September 25, 1960 in Tehran, Iran. He attended the Southern Connecticut State University (SCSU) Physics Department and graduated with Honor in May 1995. While attending at SCSU, he work on a proposal which led to a Two years project studying the conductivity of solid at cryogenic environment.

He entered University of Tennessee Space Institute (UTSI) in September 1995 to pursue a degree in Material Science Engineering. He worked in conjunction with Arnold Engineering and Development Center (AEDC) wind tunnel surface enhancement project.. The main goal of this project was to create a corrosion resistance coating using high-power laser on the surface of wind tunnel's component to improve operational capability of the wind tunnel.

Farhad completed his studies and the related project in Center for Laser Application at UTSI in and received a Master of Science in Material Science Engineering.